Durham E-Theses

High precision simulations of electroweak physics with Sherpa

THOMPSON, JENNIFER,MARY

High Precision Simulations of Electroweak Physics with SHERPA

Jennifer M. Thompson

Abstract

One vital theoretical tool in the ever-improving description of particle physics is Monte Carlo event simulation. With the CERN LHC currently exploiting the highest energies in any human-made experiment, with unprecedented precision for a range of processes, very precise theoretical models are strongly motivated. This thesis introduces an implementation of Sudakov logarithms, which are a high-energy approximation to the exact NLO calculation of the electroweak quantum theory, within the SHERPA Monte Carlo framework. As well as this, it validates and applies the SHERPA + OPENLOOPS interface to a range of interesting electroweak processes at NLO in QCD. One key area of study in the electroweak sector is that of high multiplicities of weak bosons in the final state, which are motivated by the insight these studies could provide into the recently discovered 125 GeV particle, with properties consistent with the Standard Model Higgs boson. Furthermore, several electroweak processes are key backgrounds in searches for physics beyond the Standard Model. In addition, leading order results are presented for more complex electroweak processes for which such a high level of precision has not yet become necessary. The thesis is concluded with studies at a potential future 100 TeV proton-proton collider.

High Precision Simulations of Electroweak Physics with Sherpa

Jennifer M. Thompson

A thesis submitted in partial fulfilment
of the requirements for the degree of
Doctor of Philosophy

Department of Physics
Durham University

October 18, 2015

Contents

List of Figures

List of Tables

Declaration

I confirm that no part of the material offered has previously been submitted by myself for a degree in this or any other University. Where material has been generated through joint work, the work of others has been indicated.

Jennifer M. Thompson
Durham, October 18, 2015

Acknowledgements

Dedication

This thesis is dedicated to my wonderful family, who have been endlessly supportive and encouraging throughout my studies. And, of course to my partner, Mark Zentile, who have all shown me amazing support and tolerance for the past 4 years. I cannot imagine how much more challenging this process would have been without them behind me all the way.

Chapter 1

Introduction

1.1 The LHC and Future Colliders

The recent progress in experimental particle physics has been largely driven by the ongoing experiments at the CERN LHC. The LHC is currently the highest energy particle physics collider in the world. It is capable of reaching centre-of-mass energies of up to $14\,\mathrm{TeV}$ with proton-proton collisions. From its first successful run, data is available at $7\,\mathrm{TeV}$ with $4.8\,\mathrm{fb^{-1}}$ of data and $8\,\mathrm{TeV}$ with $20.3\,\mathrm{fb^{-1}}$ of data. The physics results from these experiments have a broad range and provide some of the most precise and detailed analyses available. An early, great success of the LHC is the 2012 discovery of the Higgs boson with a mass of $125\,\mathrm{GeV}$, which has been confirmed by both the ATLAS and CMS experiments [1, 2]. This discovery completes the Standard Model of particle physics (SM), and validates the Brout-Englert-Higgs (BEH) mechanism of electroweak (EW) symmetry breaking mechanism [3–8], which was initially proposed about 5 decades ago. To date, many of the properties of this boson have been found to be in agreement with the SM predictions, including its couplings to both fermions [9–11] and bosons [12–14] as well as its spin-parity quantum numbers [15, 16].

In June 2015, the LHC restarted at an increased centre-of-mass energy ($\sqrt{s}$) of $13\,\mathrm{TeV}$. This is before it will finally reach its design energy of $14\,\mathrm{TeV}$, with an expected total luminosity of $3\,\mathrm{ab^{-1}}$. Possibilities for future colliders after the LHC, which would operate at even higher centre-of-mass energies,

are being discussed. For example, the potential for physics at a $100\,\text{TeV}$ machine [17] opens up several new potential physics studies as well as introducing challenges that are not present at current energies.

Despite the amazing success of the LHC so far, there are still several deep, open questions to be explored by subsequent runs and future colliders. This thesis presents both phenomenological studies into relevant electroweak processes, and the implementation and validation of some tools that allow the necessary high precision to be obtained. These questions include:

1. **Precision studies of Higgs boson couplings to other SM particles**
   Although current measurements of the Higgs boson couplings to the other SM particles have been measured to be in good agreement with the SM, further precision measurements are necessary to contain these couplings, because any deviation from SM predictions would be an indication of beyond the Standard Model (BSM) physics.

2. **Anomalous gauge boson coupling**
   Similarly, the measurement of the tri-linear gauge boson couplings – and, once possible, also the quartic couplings – is necessary to constrain possible anomalous gauge boson couplings. These would be BSM phenomena which would result from the inclusion of new operators, which are typically of higher dimension.

3. **Higgs boson self-coupling**
   The Higgs boson self-coupling parameters, the tri-linear and quartic couplings, are yet to be precisely measured. These couplings are potentially very sensitive to new physics, and therefore their measurement has the potential to place stringent constraints on new physics models.

4. **Dark matter**
   The LHC has not yet found a suitable candidate for dark matter, which makes up $\sim 25\,\%$ of the universe. As this is likely to be a new, massive particle, it could be detectable at future colliders. An option for this dark matter is that it could couple to the SM through the Higgs boson interaction only, as a so-called Higgs portal.

5. **Supersymmetry or other extensions of the SM**

   Supersymmetry (SUSY) is a very popular extension of the SM, and is capable of presenting solutions to many problems with the SM, such as dark matter and the hierarchy problem. As yet, no evidence of SUSY has been observed but the search will continue at higher energies, with several SUSY models and regions of parameter space as yet not excluded.

1.2   Monte Carlo Event Generators

Particle physics phenomenology is dominated by calculations, based on first principles, in the perturbative expansion of the underlying quantum field theory. By the nature of these calculations, they become almost prohibitively complicated beyond next-to leading order (NLO), at least with current technology. Within this approach, it is also not possible to describe the very high-multiplicity final states (hundreds or thousands of particles) commonly encountered in experiments. Furthermore, there are no first-principle calculations for the low-energy physics that plays an important role in any particle physics experiment: hadronisation effects and the underlying event. This seriously limits the predictive power of the theory, and strongly motivates the Monte Carlo approach. This thesis makes use of the Sherpa Monte Carlo event generator, with its OpenLoops interface where applicable, to perform several phenomenological studies into the EW sector.

Monte Carlo event simulations provide the interface between the low-multiplicity final states of fixed-order perturbation theory with the complicated high-multiplicity hadronic experimental final state. This approach divides the calculation of the full event into several stages, occurring at different scales. This allows the stages to be considered to factorise and therefore be treated more or less independently. In this way, the Monte Carlo approach to event simulations can overcome the limitations of other theoretical approaches discussed above.

1.2.1 Overview of the Physics Stages

The following provides a very brief overview of the key physics stages implemented in a Monte Carlo simulation. An excellent and more thorough review is available in Ref. [18], and references therein.

Hard Process

Because many processes of interest at colliders involve a large transfer of transverse momentum, Monte Carlo simulations begin with a calculation of the underlying hard process of the event, which can have several external particles. This can be calculated from the perturbation theory of the quantum fields, made possible even in QCD by the nature of asymptotic freedom of the quanta, quarks and gluons. The hard process can then be calculated from matrix elements (MEs) resulting from, e.g., all relevant Feynman diagrams. The partonic cross section is calculated from the squared ME, averaged over incoming colours and spins. At hadron colliders, the partonic cross section must further be folded with the parton distribution functions (PDFs) of the incoming hadrons – protons at the LHC – which govern the transition from hadrons to quarks and gluons, to finally produce the total, hadronic cross section. The result is then integrated over the phase-space of the final state particles. While these advanced numerical methods are capable of more complex hard processes than a purely analytical approach, they do not meet the full complexity of the experimental final states. This is because of the high scale at which the hard process occurs. It allows the particles to radiate possibly large numbers of particles as they evolve to the low scale of hadronisation, which is discussed in more detail below.

It is possible that some of the particles produced in the final state of the ME are unstable, and need to decay. This can be factorised if the particle is considered in the narrow-width approximation. Within the SHERPA [19, 20] framework, these decays can be treated in such a way as to correctly include spin correlations and redistribute the kinematics onto a Breit-Wigner distribution. In these decays, new particles are created. These new particles can also be unstable and need to decay themselves, creating a chain than terminates at stable or sufficiently long-lived particles.

Parton Shower

Coloured particles produced in the hard process considered above can radiate secondary quanta, in the same way that charged particles emit photons. The parton shower allows this cascade of an arbitrary amount of secondary radiation to be described. A complication in QCD, as compared to the QED case, is that emitted gluons can, themselves, emit further gluons.

The hard process is a fixed order calculation, and can be supplemented by the parton shower, as this is a complementary approximation. The parton shower is completely universal and becomes exact in the soft-collinear region of phase-space, where the majority of the additional radiation occurs. It acts as a numerical solution to the renormalisation group equation, performing an effective resummation of the large logarithmic terms introduced. Current implementations of parton showers are available to leading logarithmic accuracy; they describe the leading emissions from the external particles as they evolve from the high scale of the hard process to a low scale at which non-perturbative effects dominate due to the confinement property of QCD. At this scale, $\mathcal{O}(1\,\mathrm{GeV})$, a phase transition occurs from the quanta of QCD to colourless bound states. In Monte Carlo event simulation, this phase transition is described by a procedure known as hadronisation, which is discussed below.

Hadronisation

Because there are no quantitative models available from first principles for hadronisation, Monte Carlo event simulations use qualitative models such as the string [21, 22] and cluster models. These involve several unconstrained parameters, which reflect the lack of knowledge about this physics. These parameters are determined by fitting to data. Since this occurs at a scale so well separated from the hard interaction, hadronisation can be considered to factorise as a universal procedure independent of the hard process and parton shower.

The string model of hadronisation relies on the long-distance confinement property of QCD, and treats the colour flow along quark lines as flux tubes.

Breaks in these tubes correspond to particle creation, and gluons provide 'kinks' in the tube, which are associated with an energy and a momentum. The cluster model is instead predicated on the pre-confinement [23] nature of the parton shower, such that, once gluons are forced to split to quark-antiquak pairs, the hadrons comprise of colour singlets of quarks which neighbour each other in colour space.

Hadron and τ Decays

Many hadrons produced in this hadronisation step will be unstable. Therefore, in order to produce a realistic experimental final state, these unstable hadrons must decay. The branching fractions for these decays can be taken from look-up tables, with many of the relevant numbers being reported in the Particle Data Group's Review of Particle Physics [24]. However, for some decays theoretical models are employed instead, and not all hadrons are included in the simulations.

The hadronic decay products can potentially need to decay further, and this proceeds until the hadrons have a sufficiently long lifetime. Typically, this means that light mesons and baryons are considered stable. Although not a hadron, the τ lepton decay to its neutrino and a virtual W boson can be implemented alongside the hadron decays.

QED Shower

Additional QCD radiation was considered above in a parton shower approach. Naturally, particles charged under QED can radiate secondary quanta (photons) as well. QED radiation can also be treated in a parton shower approach, with electric charge used in place of the colour flow.

An alternative approach to QED radiation is provided by the YFS [25] procedure, which is an exponentiation of the full eikonal approximation to soft photon emission below some cut-off as well as the virtual contributions.

Multiple Interactions

An additional difficulty presents itself at a hadron collider. Because hadrons are extended objects, it is very likely that a hard interaction is supplemented by other partonic collisions occurring at lower energy. These collisions are simulated as pure $2 \to 2$ QCD processes, and typically involve small transfers of momentum, yielding particles with very small values of transverse momentum. As the colliding partons are coloured, these interactions can have an impact on the colour flow of the entire event.

This procedure does not affect the total cross-section for the process, and the radiation from these interactions rarely produce radiation that passes a jet definition. Instead, the effect on the event is more global; multiple interactions increase particle multiplicity and energy.

1.2.2 Recent Developments

In recent years, the Monte Carlo community has made great progress in accuracy, by including NLO QCD MEs in simulations. These calculations frequently rely on an interface to external code to provide the virtual part of the NLO contribution, with the Monte Carlo contributing the rest of the calculation. Currently, NLO QCD calculations are the standard level of precision in simulations of LHC events. However, as experimental precision improves, even this level of accuracy in QCD can become a limiting factor in physics studies. Calculations to next-to-next-to leading order (NNLO) QCD results have already been published for some processes [26–37] as have results for NLO EW corrections [38–41].

The first steps towards including NNLO QCD in a Monte Carlo event generator with parton showering effects have been completed to date [42–44], and there has been a similar interest in including NLO EW calculations [45–47]. These face different technical challenges to the NNLO QCD implementations, and Refs. [45–47] show successful implementations of EW NLO calculations within Monte Carlo event generators.

1.2.3   EW Sudakov Logarithmic Corrections

This thesis also details and validates the implementation of EW Sudakov approximation to NLO EW corrections in SHERPA. A contribution to full NLO EW calculations comes from EW Sudakov logarithms. These logarithms are a consequence of the scale hierarchy between the centre-of-mass energy of the collision and the EW scale, and therefore naturally grow logarithmically with energy. As the centre-of-mass energy increases, the EW Sudakov logarithms begin to dominate the NLO EW correction. Because it is possible to implement these logarithms without the full machinery of NLO EW calculations, EW Sudakov logarithms are a very useful approximation to the full NLO EW calculation in the high-energy limit. The EW Sudakov approximation has been studied in many different processes [48–59].

The EW interaction includes weak bosons with masses of the order of the weak scale, and the photon, which is massless. The interaction can, therefore, be considered to have two phases: a symmetric phase in which all EW bosons have equal masses, and a broken phase which accounts for the difference between the masses of the weak bosons and the photon. The high-energy approximation of EW Sudakov logarithms is dominated by the symmetric phase, and the logarithms arising from the scale difference between the photon and the weak bosons is cancelled by real radiation.

The form of these logarithms is $\log(|(p_i + p_j)^2|/M_V^2)$, where M_V is the mass of the boson and p_i, p_j are the momenta of external legs i, j of the calculation relevant to the EW correction. It is clear that these logarithms will increase with the centre-of-mass energy, and will begin to dominate EW corrections in the high-energy limit. They are also comparable in size to NNLO QCD corrections, and as such a consistent implementation of both the NNLO QCD and NLO EW corrections is important. The EW Sudakovs can be included on top of fixed order MEs in a Monte Carlo simulation as a K-factor. This is a factor that multiplies the amplitude squared by some constant value, and therefore makes including the mixed NLO QCD+NLO EW correction trivial.

The above paragraphs discuss the calculation of the Sudakov logarithmic approximation in the absence of any real EW boson emission. However, in a

typical experimental analysis, observables are likely to be sufficiently inclusive to either missing energy, jets or leptons as to include at least some of the real correction. These real emission processes will then cancel some of the logarithms arising from the virtual exchange, and must be included in simulation for an accurate description of the physics. It is trivial to include these as additional LO processes at $\mathcal{O}(\alpha_{\mathrm{EW}}^{n+1})$ alongside the Born process, where n is the order in the EW coupling, α_{EW}, of the Born process considered. This is at minimal additional cost in CPU time. Nevertheless, the large Sudakov logarithms from virtual EW boson exchange have a significant impact in the high-energy tails of distributions, which is important for new physics searches and precision EW physics studies.

It is worth noting that non-Abelian interactions naturally violate [60] the Bloch-Nordsieck (BN) theorem [61], leading to large logarithmic corrections becoming physically relevant even in fully inclusive calculations due to non-cancellation of the real and virtual emission. For Abelian interactions, such as QED, the BN theorem guarantees the exact cancellation of the real and virtual divergences. However, the more general Kinoshita-Lee-Nauenberg (KLN) [62, 63] theorem applies to non-Abelian interactions. Compared to the BN theorem, the KLN theorem includes an additional term that is in general non-zero and can lead to IR divergences. In QCD the exact cancellation between the real and virtual divergences is recovered due to colour confinement. This introduces a colour averaging over the initial state, washing out the non-cancellation term. In contrast, the initial state for EW interactions is not an EW singlet, and therefore the non-cancellation of the real and virtual contributions can be observed. The NLO calculation in EW, therefore, includes a logarithmic dependence on the IR cut-off of the theory. However, this does not have such a substantial impact on the cross-section, and even in distributions the inclusion of real radiation greatly reduces the virtual contribution.

1.3   Structure of the Thesis

Most of the work included in this thesis make use of the Sherpa [19, 20] Monte Carlo event generator, either using or extending its functionality.

SHERPA is a general purpose Monte Carlo event generator with in-built ME generators, COMIX [64] and AMEGIC++ [65]. MEs can therefore be generated up to NLO QCD accuracy, with an interface to an external one-loop provider for the virtual contribution. Where NLO QCD calculations are performed, they use the interface to the one-loop provider, OPENLOOPS [66]. This is a fully automated code which uses a numerical recursion method. For these NLO QCD calculations, the COLLIER library [67] is used to provide the tensor and scalar integrals, as this provides a high level of numerical stability. These MEs can then be passed through the internal parton shower and subsequent hadronisation. Unless otherwise specified, the PDFs are those from CT10 [68].

This thesis aims to produce precision physics studies in the EW sector of the SM. These studies are vital for the remaining questions in particle physics. The tools required for precision studies into EW processes are NLO corrections in both QCD and EW.

A validation is included of an automated NLO QCD interface for nearly arbitrary processes in the SM, which are calculated to NLO in QCD and correct matching of these MEs to the parton shower. The physics studies presented to NLO accuracy in QCD are EW processes of interest at high precision. The NLO techniques are employed in Higgsstrahlung production (VH production for $V = W^\pm Z$), where couplings between the Higgs boson and the gauge boson can be explored, as well as in tri-lepton production channels in the SM, which form backgrounds to several BSM searches. In particular, these backgrounds are of interest in neutralino and chargino searches at the LHC experiments [69–74]. A study into the Higgs boson tri-linear self-coupling is also presented, where the $t\bar{t}HH$ channel is exploited as the leading contribution to di-Higgs boson production with constructive interference between contributing diagrams [75].

The second technique demonstrated in this thesis is that of the implementation of an automated high-energy approximation to NLO EW corrections within the SHERPA ME generator framework, the EW Sudakov implementation introduced in Subsec. 1.2.3.

In addition, some EW processes are considered at 100 TeV, in preparation

for a potential future collider at this energy [17]. These studies also focus on EW processes, and extend the previous tri-lepton study as a BSM background. The relative cross-sections for weak boson fusion (WBF) production of multiple Higgs bosons are presented, alongside theoretical calculations of multiple weak boson production.

To summarise, this thesis consists of an overview of the relevant theory in Chap. 2, followed by three main parts:

1. **Part I**

   To open the thesis, two chapters are dedicated to work completed into the implementation and validation of high precision methods within the SHERPA framework. Firstly, there is a validation study of the SHERPA + OPENLOOPS interface with a comprehensive check of total cross-sections for a range of processes. These are checked against published MADLOOP numbers. Secondly, there is a detailed explanation of the implementation of EW Sudakov logarithms within SHERPA along with validation plots and initial results.

2. **Part II**

   The second part of the thesis focuses on the application of precision Monte Carlo calculations to LHC physics. These chapters use the SHERPA + OPENLOOPS interface validated in the first part. Results are shown for important EW processes at LHC energies, both for Higgs boson studies and SUSY searches.

3. **Part III**

   The last part of this thesis looks at the future of precision EW physics beyond the LHC. This presents results for EW processes which will be of interest in a 100 TeV hadron collider.

The conclusions are then presented in Part IV.

Chapter 2

Theory

This chapter outlines the current literature and theoretical basis on which many of the subsequent chapters rely. It outlines the status of Monte Carlo simulations and details the tools employed to extend these simulations to NLO QCD accuracy. The SHERPA + OPENLOOPS interface is used as an explicit example, because this is the set-up which will be employed in this thesis. Other codes are available, and these are mentioned, although their exact methods are not detailed.

2.1 The Cross-Section

The general form for the cross-section, σ, for a $n + 2$-leg process as in Fig. 2.1 at a hadron collider, is

$$
\sigma(\mu) = \int \int \mathrm{d}x_1 \mathrm{d}x_2 f_1(x_1, \mu) f_2(x_2, \mu) \int (2\pi)^4 \delta^4 \left(p_1 + p_2 - \sum_f p_f \right) \times \\
\frac{|\mathcal{M}(\mu)|^2}{2\hat{s}} \prod_f \frac{\mathrm{d}^3 p_f}{(2\pi)^3 2E_f} \, ,
\tag{2.1}
$$

where $E_{1(2)}$, $p_{1(2)}$ are the energy and momentum of incoming leg 1(2), respectively; E_f and p_f are the energy and momentum of the final state leg f. The partonic centre-of-mass energy is denoted by $\sqrt{\hat{s}}$, f_i is the PDF for hadron i and x_j denotes the momentum fraction of parton j. $\mathcal{M}(\mu)$ represents the ME evaluated at scale μ, where the renormalisation scale, μ_R, and factorisa-
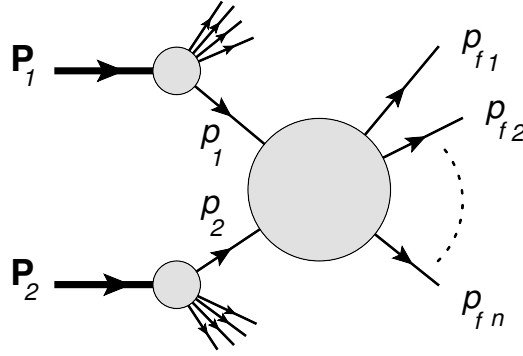
Figure 2.1: A general diagrammatic representation of a hard process at a proton-proton collider for incoming protons with momenta P_1 and P_2, where arrows denote the direction of the relevant momentum. p_1, p_2 are the momenta of the incoming partons, and p_{fj} is the momentum of the final state particles from $j = 1$ to $j = n$.

tion scale, μ_F, are taken to be equivalent as $\mu_R = \mu_F = \mu$. These scales are discussed in more detail in Subsec. 2.1.1.

In addition to calculating this total cross-section, it is important for Monte Carlo simulations to be able to provide fully differential distributions, $d\sigma$. This allows the calculation of the distribution for an arbitrary observable, $\mathcal{O}$, whose distribution is defined by $d\sigma/d\mathcal{O}$.

2.1.1 Fixed Order Scales

The importance of the PDFs in a Monte Carlo simulation has been mentioned above. These must be evaluated at a scale known as the factorisation scale, μ_F. This scale is related to the hard process, but is unphysical. This implies that any dependence on this scale should vanish if an all-orders calculation in perturbation theory was performed. At LO there is a strong dependence on this scale choice.

A second unphysical scale, μ_R as introduced above, is the of the renormalisation scale, which determines the scale at which the strong coupling is evaluated. The relationship between the values of the coupling constants evaluated at two different scales, Q_1 and Q_2, is given by the renormalisation group equation,

$$\frac{d\alpha}{d\log(Q_1/Q_2)} = \beta(\alpha).$$

(2.2)

The appropriate β function for the strong coupling constant, α_s, is

$$\beta(\alpha_s) = -\left(11 - \frac{2}{3}n_f\right)\frac{\alpha_s^2}{2\pi}, \qquad (2.3)$$

where n_f is the number of flavours of quarks considered to be massless. The ME also depends on this scale, through the strong running coupling. However, for most processes, the factorisation and the renormalisation scales are taken to be equivalent, $\mu_F = \mu_R$, as in Eq. (2.1).

2.2 Monte Carlo Simulation

As has been mentioned in Chap. 1, Monte Carlo simulations allow high multiplicity hadronic final states typical of collider experiments to be theoretically modelled. This section describes the hard process calculation in Monte Carlo simulation in more detail, explaining some of the methods and tools employed. It also details the interaction between the ME and the parton shower.

2.2.1 Fixed Order Calculations

The procedure outlined in Sec. 1.2 begins with the calculation of a fixed-order perturbative calculation. This section discusses the method employed in calculating NLO MEs. Calculations of NLO QCD cross-sections, σ_{NLO}, take the form

$$\sigma_{\text{NLO}} = \int \mathrm{d}\Phi_B B + \int \mathrm{d}\Phi_V V + \int \mathrm{d}\Phi_R R, \qquad (2.4)$$

where B is the differential LO cross-section, V is the differential virtual contribution and R is the differential real contribution. Φ_X represents the appropriate phase-space for X. Fig. 2.2 shows the virtual (left-hand-side) and real (right-hand-side) contributions. The virtual diagram includes an undefined loop momentum, q in Fig. 2.2, which means that V must contain the integral over q. This integration produces divergences in the limits $q \to \infty$, the UV divergence, and $q \to 0$, the IR divergence. UV divergences can
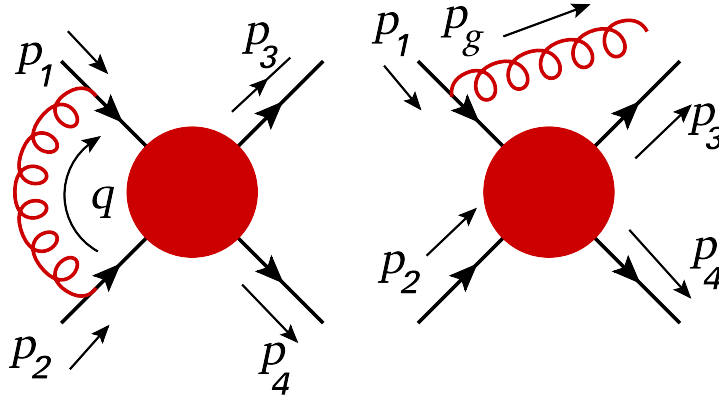
Figure 2.2: Left-hand-side shows the virtual contribution to the NLO cross-section, and right-hand-side shows the real contribution to some arbitrary process denoted by the blob. p_i denotes the external momenta for $i = \{1, 2, 3, 4\}$, and q the internal loop momentum.

be handled with a regularisation and renormalisation procedure, however the IR divergences require the inclusion of the real radiation in order to become finite.

An analytical method for handling these divergences of the NLO calculation is dimensional regularisation [76]. Taking this as an example, the divergences are parameterised by ϵ, where ϵ is defined by the number of dimensions, D, used in the calculation according to $D = 4 - 2\epsilon$. As ϵ is taken to zero, the real and the virtual contributions diverge. However, the explicit analytical expressions for the divergences in the real and the virtual terms exactly cancel each other.

Since numerical methods cannot integrate the divergent quantities separately, the divergences cannot be naively treated. One possible solution to this, which is the current approach adopted by Monte Carlo event simulators, involves cancelling the divergences at the integrand stage. Fig. 2.3 shows a diagrammatic representation of the NLO QCD cross section for $e^+e^- \to q\bar{q}$ production. There is no interference between the real and the virtual contributions, as the final states do not exist in the same phase-space. Therefore, in order to cancel the divergences the subtraction method introduces an additional quantity, S, as

$$\int \mathrm{d}\Phi_{\mathrm{NLO}}\sigma_{\mathrm{NLO}} = \int \mathrm{d}\Phi_B \left[B + V + I \right] + \int \mathrm{d}\Phi_R \left[R - S \right]. \qquad (2.5)$$
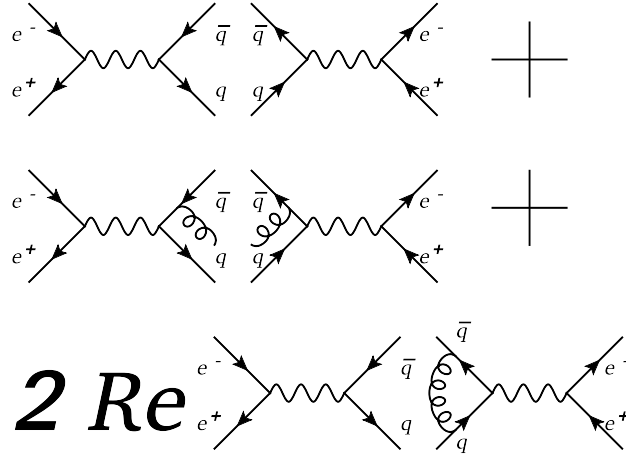
Figure 2.3: The diagrammatic representation of NLO $e^+e^- \to q\bar{q}$ production. This comprises a LO contribution (top line), a real emission part (middle) and an interference term between the tree-level diagram and the virtual contribution.

I is the integral of S over the one-parton subspace,

$$I = \int d\Phi_1 S, \qquad (2.6)$$

such that the operation amounts to adding 0 to Eq. (2.4). The LO term, B, and the virtual term, V, have been collected together because they share a common phase-space, as can be seen from Fig. 2.3. This phase-space is $\Phi_B \equiv \Phi_N$ for an N-body final state Born process, while $\Phi_R \equiv \Phi_{N+1}$. S represents a structure that exactly cancels the divergences in R, and therefore I exactly cancels the divergences introduced by the virtual correction. Now each term in the equation for the NLO QCD cross-section is separately finite and appropriate for Monte Carlo integration.

The conditions required for S to fulfil are listed in Ref. [77]. These conditions are that S must:

- not be dependent on the considered observables.

- exactly cancel all divergences of R.

- not introduce additional divergences.

- be a convenient form for Monte Carlo integration.

- be analytically integrable over the one-parton sub-space.
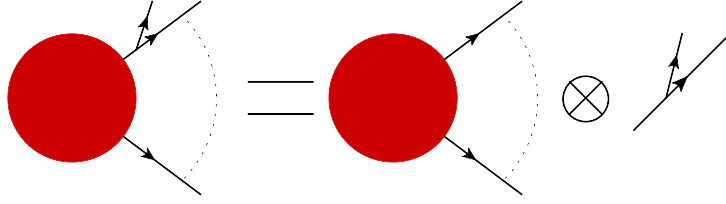
Figure 2.4: Diagrammatic representation of Catani-Seymour splitting kernels used for S subtraction terms.

Ref. [77] introduces a universal subtraction scheme for calculating S for an arbitrary process. This is known as Catani-Seymour subtraction, and is shown diagrammatically in Fig. 2.4. This implies the structure for the subtraction terms, S, of

$$S = \sum_{\text{dipole}} B \otimes \mathrm{d}V_{\text{dipole}}, \qquad (2.7)$$

such that S is expressed as a convolution of an underlying LO term, B, and a universal splitting function, V_{dipole}. The divergent information is contained within V_{dipole}, and naturally B contains all the process-dependence. The mapping of the real emission final state back onto its LO partner introduces some momentum violation, which must be absorbed by a spectator particle, defined as a relevant colour partner.

The subtraction terms formed in this way are a summation over all possible splittings that could give rise to the final state S structure. The splitting function $\mathrm{d}V_{\text{dipole}}$ depends on the final state partons involved in the splitting, including the spectator particle included for momentum conservation.

Other subtraction schemes exist, and produce similarly process-independent subtraction terms, such as Nagy-Soper dipoles [78, 79], the FKS method [80] and antenna subtraction [81, 82]. The following section details how to proceed to match the NLO QCD ME to a parton shower.

One-Loop Providers

Considering, once again, the equation for a numerical NLO calculation given in Eq. (2.5), the B, I and $R - S$ components can be calculated by SHERPA stand-alone. The remaining V component is the virtual loop contribution to the NLO calculation. This is usually obtained from external codes, such
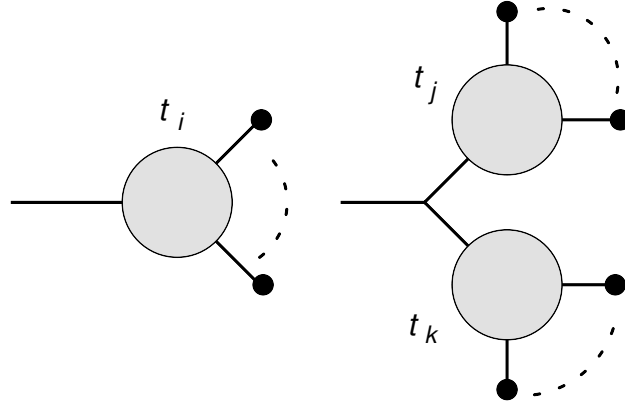
Figure 2.5: A diagrammatic representation of a step in a tree-level recursion calculation. The lines terminating in black blobs represent the external lines of the diagram. The remaining line (far left-hand-side of each diagram) represents an internal, off-shell line.

as those listed in Subsec. 2.2.1. The SHERPA + OPENLOOPS interface, which is validated and employed for phenomenological studies in this thesis, uses OPENLOOPS' very versatile native interface.

The focus in this thesis is on the interface with the OPENLOOPS code. This is a fully automated one-loop generator based on a fast numerical recursion for multi-particle processes.

The OPENLOOPS method can be used with either tensor integral reduction or OPP [83] reduction. For tensor integrals the COLLIER library [67] is used, which guarantees high numerical stability thanks to the methods of Refs. [84–86]. Alternatively, CUTTOOLS [87] can be used for OPP reduction, with the scalar integrals provided by ONELOOP [88].

To briefly explain the method employed by OPENLOOPS, it is necessary to consider recursion methods, beginning with tree-level recursion. Fig. 2.5 shows how the recursion of tree-level amplitudes occurs. The left-hand diagram, M, in Fig. 2.5 shows a graphical representation of a sub-tree t_i with colour-stripped amplitude $a^\alpha(t_i)$. α denotes the spinor or Lorentz index of the cut line, as appropriate.

The colour factor, C, of the diagrams is factored out of the amplitudes as

$$M(t_i) = C A(t_i) \, , \tag{2.8}$$

where $A(t_i)$ can be calculated as a contraction of two sub-trees.

The sub-tree t_i can be constructed by connecting sub-trees t_j and t_k with amplitudes $a(t_j)$ and $a(t_k)$, respectively, by a vertex, as shown in Fig. 2.5, as

$$a^\alpha(t_i) = V^\alpha_{\beta\gamma} a^\beta(t_j) a^\gamma(t_k)\,, \tag{2.9}$$

where $V^\alpha_{\beta\gamma}$ denotes the calculation of the vertex and propagators introduced in the recursion. This process of decomposition can then be applied recursively until external lines are reached.

It is possible to use this technique with loop calculations. Fig. 2.6 shows the cutting of a loop propagator, labelled D_0, for a diagram with colour-stripped amplitude A_v. Considering the set of n sub-trees, shown as blobs in Fig. 2.6, to be collectively labelled as S_n, this amplitude involves an integral over the loop momentum, q, in D dimensions of

$$A_v = \int \frac{\mathrm{d}^\mathrm{D}q N(S_n, q)}{D_0...D_{n-1}}\,, \tag{2.10}$$

where the denominators of the relevant propagators are $D_0...D_{n-1}$, and the numerators of the evaluation are collected as $N(S_n, q)$. Eq. (2.10) shows the evaluation of the amplitude shown diagrammatically in Fig. 2.6. In principle, this enables the recursion method described for tree-level diagrams to also calculate $N(S_n, q)$ for fixed values of the loop momentum, as needed in OPP reduction, by

$$N^\alpha_\beta(S_n, q) = V^\alpha_{\gamma\delta}(S_n, q) N^\gamma_\beta(S_{n-1}, q) t^\delta_n\,, \tag{2.11}$$

where the sub-tree t^δ_n represents the tree-like sub-diagram of N^α_β, and the vertex and numerator of the propagator introduced in the recursion are contained in $V^\alpha_{\gamma,\delta}(q)$.

Repeating the recursion to evaluate the numerator for many loop momenta turns out to be quite inefficient. Furthermore, there is no straight-forward and efficient way to use this procedure in combination with tensor integrals. Instead, in the OPENLOOPS approach, the momentum dependence is fac-
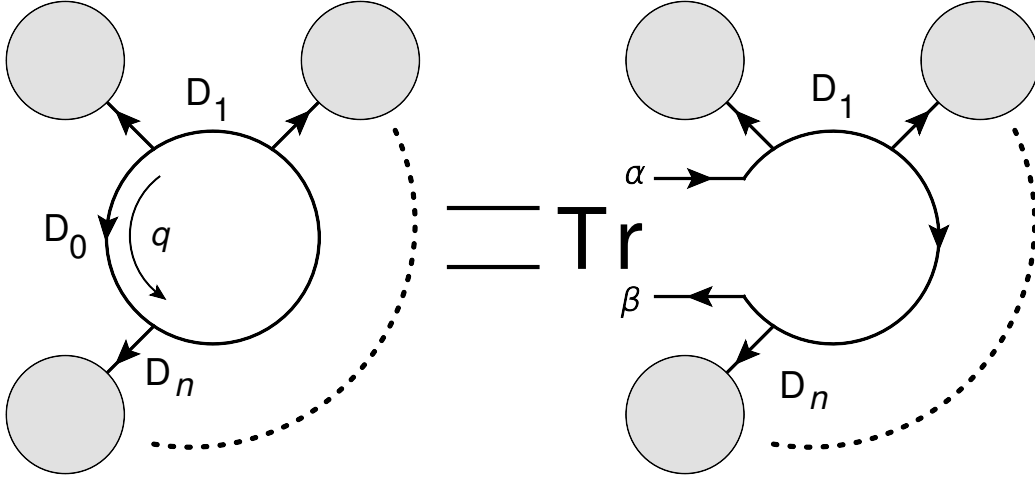
Figure 2.6: The cutting of loop propagator D_0 to create a tree-like structure to be calculated with tree-level recursive relations. The loop calculation is then given by the trace over external indices α and β. The blobs represent sub-amplitudes at tree-level.

torised out from both N_β^α and $V_{\gamma\delta}^\alpha$. This yields the following

$$
N_\beta^\alpha(q) = N_{0,\beta}^\alpha + N_{1,\beta;\mu_1}^\alpha q^{\mu_1} + ... + N_{m,\beta;\mu_1...\mu_m}^\alpha q^{\mu_1}...q^{\mu_m} \tag{2.12}
$$
$$
V_{\gamma\delta}^\alpha(q) = V_{0,\gamma\delta}^\alpha + V_{1,\gamma\delta;\mu}^\alpha q^{\delta;\mu}, \tag{2.13}
$$

where the first subscript for N, V on the right-hand-side of Eqs. (2.12) and (2.13) denotes the order of q for which it is a coefficient. Higher orders in q are possible for effective theories. These coefficients are numerically calculated and stored for later use.

With this approach, multiple evaluations of $N_\beta^\alpha(q)$ become very fast, therefore reducing the CPU time needed for OPP reduction significantly compared to the tree recursion approach described earlier. On the other hand, inserting Eq. (2.12) into Eq. (2.10) and taking the trace over N, naturally yields the tensor integral representation of the amplitude, where the polynomial coefficients of the numerator correspond to the coefficients of the tensor integrals.

Since the publication of Ref. [66], other collaborations have implemented this method, such as MadGraph + aMC@NLO [89].

Available Tools

This subsection lists the available tools for Monte Carlo event simulation. These are the general purpose Monte Carlo simulators

- PYTHIA [90]

- HERWIG++ [91, 92]

- SHERPA [19, 20]

- ARIADNE [93]

In addition to this, there are several ME generator codes; these calculate the hard ME and interface to external code for the parton showering.

- MADGRAPH + aMC@NLO [89]

- WHIZARD [94, 95]

- ALPGEN [96–98]

- HELAC [99, 100].

For loop processes, several codes exist as one-loop providers.

- GOSAM [101, 102]

- NJET [103, 104]

- OPENLOOPS [66]

- BLACKHAT [105, 106]

Some interfaces between Monte Carlo event generators and external one-loop providers make use of the BLHA [107] standard. A very convenient way of including different PDF sets in a Monte Carlo simulation is with an interface to LHAPDF [108]. In this thesis, the default PDF set used is the CT10 PDF set, which is included directly in SHERPA. All other PDF sets used in this thesis are included via the SHERPA interface to LHAPDF.

2.2.2 Matching

LO matching to parton shower is achieved in the following way, where the phase-space dependence of the differential LO cross-section, B, is made explicit for an expansion in the parton shower, PS, up to one emission;

$$
\begin{aligned}
\sigma_{\text{LO}}^{\text{PS}} =& \sigma_{\text{LO}} \otimes \text{PS} = \\
& \int \mathrm{d}\Phi_N B(\Phi_N) \left[\Delta(Q_0^2, \mu_q^2) + \int_{Q_0^2}^{\mu_q^2} \mathrm{d}\Phi_1 \frac{\alpha_s}{2\pi} \mathrm{K}(\Phi_1) \Delta(q(\Phi_1)^2, \mu_q^2) \right] .
\end{aligned}
$$

(2.14)

Eq. (2.14) comprises a term describing no emission (left-hand term on right-most-side) and a term describing exactly one emission (right-hand term on right-most-side); α_s is the coupling constant for QCD. It is important to notice that the bracket on the right-most-side of Eq. (2.14) integrates to unity; the parton shower does not alter the total cross-section. In Eq. (2.14), and $q(\Phi_1)$ is the evolution parameter, typically considered to be virtuality, transverse momentum or opening angle. It is determined by the first emission, and is smaller than the starting scale, μ_q, and larger than the lower hadronisation scale, Q_0. The starting scale, μ_q, for the shower is a process-dependent quantity, and cannot be determined from first-principles. It is therefore an unphysical choice like the factorisation and renormalisation scales discussed earlier. This scale is typically varied by a factor of 2 to give an estimate of the theoretical uncertainty. $\Delta(t_1, t_2)$ represents the Sudakov form factor, which can be interpreted as a no-emission probability between scales t_2 and t_1. This has the form

$$
\Delta(t_1, t_2) = \exp \left(-\frac{\alpha_s}{2\pi} \int_{t_1}^{t_2} \mathrm{d}\Phi_1 \mathrm{K}(\Phi_1) \right) .
$$

(2.15)

K is the splitting kernel for the parton shower.

NLO QCD calculations include the possibility of an emission of QCD radiation from the ME. This complicates the matching of the ME to the parton shower, since the parton shower can double-count the emission from the ME. Matching algorithms avoid this double-counting by demanding that the hardest QCD emission comes from the ME.

Of the two matching procedures currently available, MC@NLO [109] and POWHEG [110, 111], SHERPA implements the S-MC@NLO method [112, 113], which is a variant of MC@NLO. This variant exactly identifies the subtraction terms with the parton shower splitting kernels. This adjustment allows the S-MC@NLO implementation to handle subleading colour configurations in a process-independent way.

Although, historically, the second matching scheme for NLO MEs, the POWHEG method can be considered as a generalisation of the MC@NLO method. In the POWHEG approach, Eq. (2.14) is transformed by including the ratio of the real emission to the Born cross-sections in the Sudakov form factor as

$$
\sigma^{\mathrm{PS}}_{\mathrm{POWHEG}} =
$$
$$
\int \mathrm{d}\Phi_N \bar{B}(\Phi_N) \left[\Delta(Q_0^2, \mu_q^2) + \int_{Q_0^2}^{\mu_q^2} \mathrm{d}\Phi_1 \frac{\alpha_s}{2\pi} \frac{R(\Phi_N, \Phi_1)}{B(\Phi_N)} \Delta(q(\Phi_1)^2, \mu_q^2) \right] .
$$
$$
(2.16)
$$

The POWHEG method, as seen up to the first emission in Eq. (2.16), exponentiates the full phase-space, and uses R/B as the splitting kernel, leading to an altered Sudakov form factor. $\bar{B}$ is the NLO reweighted Born term, as explicitly shown in the subtraction equation Eq. (2.5). The POWHEG method naturally includes configurations that are not part of the NLO calculation. In order to remedy this, the phase-space can be divided into hard and soft regions. The exact location of this split is tunable, and this can be used to mimic higher order effects.

The MC@NLO method, again up to the first emission, re-expresses Eq. (2.14) as

$$
\sigma^{\mathrm{PS}}_{\mathrm{MC@NLO}} = \int \mathrm{d}\Phi_N \bar{B}(\Phi_N) \left[\Delta(Q_0^2, \mu_q^2) + \int_{Q_0^2}^{\mu_q^2} \mathrm{d}\Phi_1 \frac{\alpha_s}{2\pi} R_S(\Phi_1) \Delta(q(\Phi_1)^2, \mu_q^2) \right]
$$
$$
+ \int \mathrm{d}\Phi_{N+1} R_H(\Phi_{N+1}) .
$$
$$
(2.17)
$$

Eq. (2.17) looks similar to Eq. (2.16), with an additional term on the right-hand side, $\int \mathrm{d}\Phi_{N+1} R_H(\Phi_{N+1})$. This originates from $R = R_H + R_S$, where R

is the real emission ME, as in Eq. (2.16), and R_H, R_S are the hard and soft regions, respectively. All of the divergences of the real emission are encoded in R_S, as the subtraction terms. If there is no emission from the ME, there is a veto on any parton shower emissions. This is shown in Eq. (2.17) by the Sudakov form factor, $\Delta(Q_0^2, \mu_q^2)$.

The NLO re-weighted LO term is provided by the following in the S-MC@NLO implementation,

$$\bar{B}(\Phi_N) = B(\Phi_N) + V(\Phi_N) + \int \mathrm{d}\Phi_1 B(\Phi_N) R_S(\Phi_1)\Theta(\mu_q - Q)\,, \qquad (2.18)$$

and R_H is given by

$$R_H(\Phi_{N+1}) = R(\Phi_{N+1}) - [B \otimes R_S](\Phi_{N+1})\Theta(\mu_q - Q)\,. \qquad (2.19)$$

2.2.3 Merging

It is possible to improve the kinematical description of observables, without performing the full NLO QCD calculation, by including multiple LO MEs with different multiplicities. This method is known as merging, and this section outlines the procedure as implemented in SHERPA, before extending this formalism to NLO, as the next logical step.

LO Merging

Multi-jet merging introduces additional QCD radiation from the ME. This produces a more accurate calculation of radiation patterns in hard, well-separated regions of phase-space than the parton shower, because the parton shower is a soft-collinear approximation. LO merging, therefore, makes use of several MEs, calculated up to some order in α_s. The inclusion of these high multiplicity MEs in calculations creates double-counting problems, as occurred with NLO MEs. Similarly, an algorithm is required to consistently include a parton shower on top of the ME.

There are several available merging algorithms, and instances of these algorithms are included in several Monte Carlo simulations. An overview of the different algorithms can be found in Refs. [114–116]. The available merging

algorithms are:

- **CKKW(-L)** [117, 118]

  This method is discussed in detail below this list. Implementations of the method can be found in Sherpa and a similar merging method, the dipole cascade [119, 120], is implemented in Ariadne.

- **UMEPS** [121]

  This merging algorithm preserves the total cross-section to LO, unlike other methods which break unitarity. There is an implementation of this merging algorithm in Pythia.

- **MLM** [97]

  This method implements the Sudakov suppression by vetoing any final state, once the parton shower has been completed, that is reconstructed to have more jets than was initially requested. It is implemented in Alpgen, MadGraph and Helac.

Focussing on the CKKW method, this introduces a merging scale, which is used to determine a minimum-distance requirement on the emissions. It requires that all emissions above the merging scale are produced from the ME as opposed to the parton shower. Below this cut, the QCD radiation is produced by the parton shower. Similar to the fixed-order scales introduced in Subsec. 2.1.1 and the parton shower starting scale introduced in Sec. 2.2.2, this is an unphysical scale whose variations provide a theoretical uncertainty on the calculation. The implemented algorithm is:

1. One of the multiplicities is selected, by weighting the processes by the cross-sections, such that the ME with final state multiplicity i is selected with the probability $\sigma_i / \sum_j \sigma_j$.

2. The final state is re-clustered back to a $2 \rightarrow 2$ process, or until no valid clustering can be found, using the parton shower splitting kernel. In this way a parton shower history can be constructed from the ME.

3. A scale for the process is calculated from the $2 \rightarrow 2$ core process, or from a process-specific scale. Process-specific scales must be used if the process cannot be re-clustered back to a $2 \rightarrow 2$.

4. The event is reweighted according to the parton shower couplings for the emissions and appropriate Sudakov form factors.

5. The parton shower radiates as a truncated shower between the ME emissions.

6. The Sudakov form factors are included by vetoing any event for which a parton shower emission is produced harder than the merging scale. The exception to this is for the highest multiplicity case, where the parton shower is required to fill the rest of the phase-space. Here events are vetoed only if the shower emits a parton harder than the softest parton shower starting scale.

This produces a consistently merged sample, with the hardest jets described to LO accuracy, as opposed to the leading logarithmic accuracy provided by the parton shower. The LO merged cross-section, as implemented in the SHERPA Monte Carlo event generator, is given by the following equation, where the merging scale is given by Q_{cut},

$$
\begin{aligned}
\mathrm{d}\sigma_{\mathrm{LO}}^{\mathrm{LOPS}} = {} & \mathrm{d}\Phi_N B_N \otimes \mathrm{PS}^N \Theta(Q_{\mathrm{cut}} - Q_{N+1}) \\
& + \mathrm{d}\Phi_{N+1} B_{N+1} \Theta(Q_{N+1} - Q_{N+2}) \Delta(Q_{N+1}^2, Q_N^2) \mathrm{PS}^{N+1} \Theta(Q_{\mathrm{cut}} - Q_{N+2}) \\
& + \dots ,
\end{aligned}
$$

$$(2.20)$$

where B_N represents the differential LO ME with final state parton multiplicity of N. Eq. (2.20) shows the explicit construction of the LO merging up to one additional emission from the ME. The subsequent emissions proceed in a similar way, each containing generating functions PS^{N+m}, where m is the number of additional QCD emissions from the ME.

NLO Merging

To extend merging to NLO QCD, a similar method to that explained in Subsec. 2.2.3 is employed. There are NLO extensions to the CKKW method, which is implemented in SHERPA and to the UMEPS scheme, which is UNLOPS. UNLOPS has the same fundamental principle of UMEPS, where the

total cross-section from the merging algorithm is maintained to NLO accuracy. Therefore, with the UNLOPS method the merging procedure is unitary.

The method presented here is the extension of the LO merging method described above to including NLO QCD accurate MEs. This procedure is MEPS@NLO, as implemented in SHERPA. NLO QCD accuracy introduces a complication: the real emission from the N parton final state contains $N+1$ parton final states, as does the LO-like contribution from the $N+1$ parton ME. This double counting is corrected by a removal of the real emission by adapting the Sudakov form factor, Δ. The contribution from the real emission term can be removed either through subtraction or a multiplicative factor. The differences between these two methods is of higher order.

Rewriting Eq. (2.20) in an appropriate way for NLO QCD merging with multiple NLO QCD MEs yields an equation for the fully differential, NLO QCD merged cross section, $d\sigma_{\mathrm{NLO}}^{\mathrm{MEPS}}$. This is expressed in Eq. (2.21) in terms of the N-parton NLO QCD cross sections, σ_N^{NLO},

$$
\begin{aligned}
d\sigma_{\mathrm{NLO}}^{\mathrm{MEPS}} = {} & d\Phi_N \bar{B}_N \otimes \widetilde{\mathrm{PS}}^N \Theta(Q_{\mathrm{cut}} - Q_{N+1}) \\
& + d\Phi_{N+1} \bar{B}_{N+1} \Theta(Q_{N+1} - Q_{\mathrm{cut}}) \left[\Delta(Q_{\mathrm{cut}}^2, Q_{N+1}^2) - \Delta^{(1)}(Q_{\mathrm{cut}}^2, Q_{N+1}^2) \right] \\
& \quad \otimes \widetilde{\mathrm{PS}}^{N+1} \Theta(Q_{\mathrm{cut}} - Q_{N+2}) + \dots.
\end{aligned}
$$

$$(2.21)$$

Eq. (2.21) shows the NLO merging procedure. $\Delta^{(1)}$ denotes the contribution to the Sudakov form factor for the real emission part. This is subtracted from the full Sudakov form factor. In the SHERPA implementation of NLO merging, the removal of this double counting is achieved in a multiplicative way. The subtraction method of this removal is shown in Eq. (2.21) as it is more illustrative for clarity. $\widetilde{\mathrm{PS}}^N$ provides the shower for the NLO QCD N particles cross section.

Further emissions can be considered to either NLO or LO accuracy on top of Eq. (2.21).

Part I

Tool Development

Chapter 3

Validation of the
SHERPA + OPENLOOPS Interface

In order to perform calculations to NLO accuracy in QCD, SHERPA [19, 20] makes use of an interface with one of several external codes that provide the virtual one-loop MEs. The one-loop providers which are currently interfaced to SHERPA are OPENLOOPS [66], NJET [103, 104], GOSAM [101, 102] and BLACKHAT [105, 106]. This chapter looks at the validation of total cross-sections calculated with the SHERPA + OPENLOOPS interface.

3.1 Introduction

A comprehensive list of total cross-sections for SM processes at the LHC has been published to NLO accuracy in QCD by the MADLOOP + aMC@NLO collaboration in Ref. [122]. This list of processes comprises an overview of LHC physics, including multiple partonic final states, massive weak bosons and photon production as well as production of massive coloured particles. This chapter presents the comparison between these published numbers and those calculated with the SHERPA + OPENLOOPS framework, as a validation of the interface.

The method of the OPENLOOPS code is described in Chap. 2. It provides loop MEs in the form of generated libraries, and these exist for a wide variety of processes, for QCD and EW corrections. Therefore, through the

SHERPA + OPENLOOPS interface, SHERPA can perform both NLO QCD and NLO EW calculations. OPENLOOPS also includes some MEs for loop-induced processes, such as $gg \rightarrow HZ$, although the validation of these processes is not included in this thesis. This chapter also does not address any validation of the S-MC@NLO implementation of distributions and observables. However, this provides a good proof-of-concept argument for the SHERPA + OPENLOOPS interface for NLO QCD calculations. uncertainties quoted in Sec. 3.4 are statistical.

3.2 Basic Consistency Checks

The form of the virtual loop contribution, V, is

$$V = B \left(\frac{P_\epsilon}{\epsilon} + \frac{P_{\epsilon^2}}{\epsilon^2} \right) , \tag{3.1}$$

where B is the Born ME, P_ϵ and P_{ϵ^2} are the coefficients to the poles diverging as $\frac{1}{\epsilon}$ and $\frac{1}{\epsilon^2}$, respectively. In this formalism, ϵ parameterises the divergent behaviour of integrals which have been performed using dimensional regularisation. It is important that the integrated subtraction term in SHERPA and the virtual contribution from OPENLOOPS agree on the values of B, P_ϵ and P_{ϵ^2} for each phase-space point. This is easy to check within the SHERPA framework, see Appendix A for details.

3.3 Set-Up

The cross-sections presented in Sec. 3.4 were calculated using both the COMIX [64] and AMEGIC++ [65] ME generators, separately, for the LO comparison. AMEGIC++ was also employed for the Born and integrated subtraction terms of the NLO calculation, using OPENLOOPS for the virtual ME. For the subtraction procedure, Catani-Seymour subtraction terms were used. This was the most CPU intensive part of the NLO QCD calculation, for the majority of processes in this validation study. The COMIX ME generator was used for the calculation of these terms, because it has a better

Parameter	value	Parameter	value
M_Z	91.188	α^{-1}	132.50698
M_W	80.419	G_F	1.16639×10^{-5}
M_b	4.75	CKM_{ij}	δ_{ij}
M_t	172.5	Γ_Z	2.4414
M_H	120	Γ_W	2.0476

Table 3.1: Relevant EW parameters. Masses, M_X, and widths, Γ_X, for particle X are given in GeV. The G_μ scheme was employed to set the relevant EW parameters.

convergence than AMEGIC++. All final state particles are considered to be stable with their widths set to zero.

The parameters in Tab. 3.1 are used for all processes considered in this chapter, and are a consistent set of EW parameters. A diagonal CKM matrix, which contains the information on mixing between quark generations, is used in the Born processes as well as the loops. The calculations presented in this chapter are performed with a fixed width scheme, as this was required in the MADLOOP calculation. However, the complex mass scheme is also implemented in the SHERPA + OPENLOOPS interface. Some of the cross-sections in the MADLOOP paper were calculated with loops involving EW bosons removed on the MADLOOP side. This is not reproduced with the SHERPA + OPENLOOPS interface, which includes all possible loops.

Any applied cuts are kept to a minimum, and any that are are applied are provided in Subsec. 3.3.1. These cross-sections were completed for 7 TeV proton-proton collisions with the MSTW2008nlo (MSTW2008lo) PDF set [123, 124] in the case of NLO (LO) calculations with massless b-quarks and the MSTW2008nlonf4 (MSTW2008lonf4) PDF set for NLO (LO) calculations with massive b-quarks. The running of the strong coupling is taken from the PDF set. The scales in this process are set such that the renormalisation, factorisation scales are set equal and to a fixed value, which enables a comparison between the integrators. This scale is chosen for each process independently. A list of the scales and number of light flavours considered is given in Tab. 3.2.

Process	μ	n_f	Process	μ	n_f
$\bar{t}$	M_t	5	$W^+(e^+\nu)$	M_W	5
tj	M_t	5	$W^+(e^+\nu)j$	M_W	5
tjj	M_t	5	$W^+(e^+\mu)jj$	M_W	5
$t\bar{b}j$	$M_t/4$	4	$Z(e^+e^-)$	M_Z	5
$t\bar{b}jj$	$M_t/4$	4	$Z(e^+e^-)j$	M_Z	5
$W^+(e^+\nu)b\bar{b}$	$M_W + 2M_b$	4	$Z(e^+e^-)jj$	M_Z	5
$W^+(e^+\nu)t\bar{t}$	$M_W + 2M_t$	5	HW^+	$M_W + M_H$	5
$Z(e^+e^-)b\bar{b}$	$M_Z + 2M_b$	4	HW^+j	$M_W + M_H$	5
$Z(e^+e^-)t\bar{t}$	$M_Z + 2M_t$	5	HZ	$M_Z + M_H$	5
$\gamma t\bar{t}$	$2M_t$	5	HZj	$M_Z + M_H$	5
W^+W^-	$2M_W$	4	$Ht\bar{t}$	$M_t + M_H$	5
W^+W^-j	$2M_W$	4	$Hb\bar{b}$	$M_t + M_H$	4
W^+W^+jj	$2M_W$	4	Hjj	M_H	5

Table 3.2: Table of the scales and number of light flavours considered in the PDF for all processes considered.

3.3.1   Applied Cuts

For processes involving a final state photon, the photon is isolated according to the Frixione isolation procedure [125] with a radius $d = 0.4$, an exponent $n = 1$ and energy fraction $\epsilon = 1$. This requires that the maximum energy deposited in a cone of radius d around the photon does not exceed ϵE_γ, where E_γ is the energy of the photon. In addition to this requirement, the photon is required to be hard and central, with a $p_\perp > 20\,\text{GeV}$ and $|\eta| < 2.5$. Any process with jets have jets defined by the k_T clustering algorithm with $p_\perp > 25\,\text{GeV}$ and a cone size of $R = 0.7$. In the case of oppositely charged leptons, $\ell^+\ell^-$, in the final state, there is an invariant mass cut, $m_{\ell^+\ell^-} > 30\,\text{GeV}$.

3.4   Results

The results of the comparison are presented in this section. Tab. 3.3 shows the comparison of LO cross-sections between AMEGIC++ and COMIX in SHERPA and MADGRAPH, which demonstrates that the two set-ups compared are identical. Tab. 3.4 shows the relative agreement at LO between the SHERPA cross-sections for both AMEGIC++ and COMIX with MADGRAPH. The

Process	MADGRAPH/pb	AMEGIC++/pb	COMIX/pb
$W^+(e^+\nu)$	5072.5(2.9)	5074.56(2.54)	5074.9(2.5)
$W^+j(e^+\nu)$	828.4(8)	827.83(82)	828.31(83)
$W^+jj(e^+\nu)$	298.8(4)	299.34(30)	299.63(30)
$Z/\gamma^*(e^-e^+)$	1007.0(1)	1007.92(10)	1007.9(1)
$Z/\gamma^*(e^+e^-)j$	156.11(3)	156.22(16)	156.35(16)
$Z/\gamma^*(e^+e^-)jj$	54.24(2)	54.32(5)	54.48(21)
HW^+	0.3428(3)	0.34296(13)	0.34266(13)
HW^+j	0.1223(1)	0.12235(12)	0.12226(12)
HZ	0.2781(1)	0.27820(10)	0.27821(14)
HZj	0.0988(1)	0.098918(99)	0.099078(99)
$W^+(e^+\nu)b\bar{b}$	11.557(5)	11.553(6)	11.5472(58)
$W^+(e^+\nu)t\bar{t}$	0.009415(3)	0.009414(5)	0.009408(5)
$Z/\gamma^*(e^+e^-)b\bar{b}$	9.459(4)	9.4552(47)	9.4564(47)
$Z/\gamma^*(e^+e^-)t\bar{t}$	0.0035131(4)	0.00351307(35)	0.003509(6)
$t\bar{t}$	123.76(5)	123.714(47)	123.67(12)
$\gamma t\bar{t}$	0.2906(1)	0.2904(1)	0.2907(4)
$Ht\bar{t}$	0.08896(1)	0.088912(9)	0.08892(8)
Hjj	1.104(2)	1.105(1)	1.103(1)
tj	34.78(3)	34.83(3)	34.807(35)
W^+W^-	29.976(4)	29.96(2)	29.98(2)

Table 3.3: Comparison of cross-section numbers between the SHERPA LO and the LO MADGRAPH numbers. Processes with an unstable Z boson include photon interference. Column 2 presents the cross-section from MADGRAPH, column 3 from AMEGIC++ and the final column from COMIX. Eq. (3.2).
*The large discrepancy for $Z/\gamma^* \to e^+e^-$ related to an outstanding disagreement with MADGRAPH.

Process	d(A,M)	d(C,M)	d(C,A)
$W^+(e^+\nu)$	0.5	0.6	0.1
$W^+j(e^+\nu)$	-0.5	-0.08	0.4
$W^+jj(e^+\nu)$	1.08	1.7	0.7
$Z/\gamma^*(e^-e^+)$	6.5	6.4*	-0.1
$Z/\gamma^*(e^+e^-)j$	0.7	1.5	0.6
$Z/\gamma^*(e^+e^-)jj$	1.5	1.1	0.7
HW^+	0.1	-0.4	-0.2
HW^+j	0.3	-0.3	-0.5
HZ	0.7	0.6	0.06
HZj	0.8	2.0	1.1
$W^+(e^+\nu)b\bar{b}$	-0.5	-1.3	-0.7
$W^+(e^+\nu)t\bar{t}$	-0.2	-1.2	-0.8
$Z/\gamma^*(e^+e^-)b\bar{b}$	-0.6	-0.4	0.2
$Z/\gamma^*(e^+e^-)t\bar{t}$	-0.05	-0.7	-0.7
$t\bar{t}$	-0.7	-0.7	-0.3
$\gamma t\bar{t}$	-1.4	0.2	0.7
$Ht\bar{t}$	-3.6	-0.5	0.1
Hjj	0.4	-0.4	-1.4
tj	1.2	0.6	-0.5
W^+W^-	-0.8	0.2	0.7

Table 3.4: Comparison of d(X,Y), as defined in Eq. (3.2), between LO cross-sections for COMIX (C), AMEGIC++ (A) and MADGRAPH (M). Processes with an unstable Z boson include photon interference.
* See caption of Tab. 3.3

distance measure, d(X,Y), is

$$d(X, Y) = \frac{X - Y}{\sqrt{\delta X^2 + \delta Y^2}}, \qquad (3.2)$$

where δX represents the uncertainty of value X.

The validation of the SHERPA + OPENLOOPS interface is provided by the comparison of the NLO QCD total cross sections with the MADLOOP calculation. These total cross sections are presented along with their relative difference, d(SHERPA + OPENLOOPS,MADLOOP), in Tab. 3.5. The SHERPA + OPENLOOPS interface shows good agreement with MADLOOP for several different processes at the LHC. There is disagreement between MADLOOP and the SHERPA + OPENLOOPS calculation for the $Z/\gamma^*(e^+e^-)$ process, as can be seen in Tab. 3.5. This disagreement in also present

Process	MADLOOP/pb	SHERPA + OPENLOOPS/pb	d(SOL,M)
$W^+(e^+\nu)$	6146.2(9.8)	6136.81(3.09)	-0.9
$W^+j(e^+\nu)$	1065.3(1.8)	1065.8(2.0)	0.2
$W^+jj(e^+\nu)$	289.7(3)	289.5(4)	-0.4
$Z/\gamma^*(e^-e^+)$	1170(2.4)	1192.04(56)	9*
$Z/\gamma^*(e^+e^-)j$	203.0(2)	203.3(7)	0.4
$Z/\gamma^*(e^+e^-)jj$	54.1(6)	54.5(6)	0.5
HW^+	0.4455(3)	0.44564(14)	0.4
HW^+j	0.1501(2)	0.1508(2)	2.3
HZ	0.3659(2)	0.36588(15)	-0.08
HZj	0.1237(1)	0.1245(2)	3.6
$W^+(e^+\nu)b\bar{b}$	22.95(7)	23.09(5)	1.6
$W^+(e^+\nu)t\bar{t}$	0.01159(1)	0.01160(1)	0.7
$Z/\gamma^*(e^+e^-)b\bar{b}$	15.31(3)	15.37(3)	1.4
$Z/\gamma^*(e^+e^-)t\bar{t}$	0.004876(2)	0.004873(5)	-0.6
$t\bar{t}$	162.08(12)	162.07(11)	-0.06
$\gamma t\bar{t}$	0.4169(3)	0.4168(7)	-0.1
$Ht\bar{t}$	0.09869(3)	0.09873(12)	0.3
Hjj	1.333(2)	1.336(2)	1
W^+W^-	43.92(3)	43.96(3)	0.9

Table 3.5: Comparison of cross-section numbers between the SHERPA + OPENLOOPS (SOL) interface and the MADLOOP (M) numbers. Processes with an unstable Z boson include photon interference. Column 2 provides the MADLOOP cross-sections, and column 3 the SHERPA + OPENLOOPS calculation. The final column is the difference between the NLO calculations, as defined in Eq. (3.2).
* See the caption of Tab. 3.3.
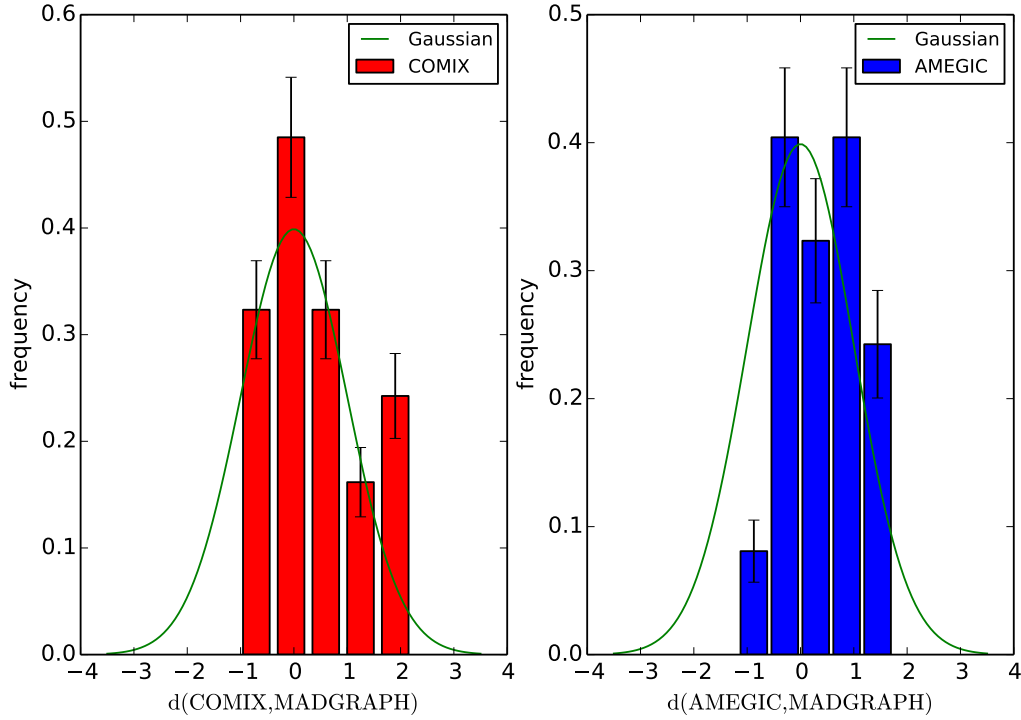
Figure 3.1: The d(SHERPA, MADGRAPH) for the processes presented in Tab. 3.3, for COMIX and AMEGIC++. These are compared to a Gaussian distribution, with all curves and histograms normalised to unit area. The uncertainties on the histogram are statistical, and d(A, B) is defined in Eq. (3.2).

in Tab. 3.4 at LO, however, the independent ME generators COMIX and AMEGIC++ agree to |d(COMIX,AMEGIC++)| < 0.1 at LO for this process. The disagreement between SHERPA(SHERPA + OPENLOOPS) and MADGRAPH(MADLOOP) for the (N)LO cross section for the $Z/\gamma^*(e^+e^-)$ process remains unresolved.

Figs. 3.1 and 3.2 show the relative difference between the calculations from X and Y according to d(X,Y), as given in Eq. (3.2). The anomalous results for $Z/\gamma^*(e^+e^-)$ are not included in these distributions. Fig. 3.1 shows the differences between the LO cross-sections for both COMIX and AMEGIC++ with MADGRAPH, for the processes presented in Tab. 3.4. The histograms are shown to be consistent with a Gaussian distribution within the statistical uncertainties for both the COMIX and AMEGIC++ ME generators considered, as is expected for a comparison between two sets of statistically
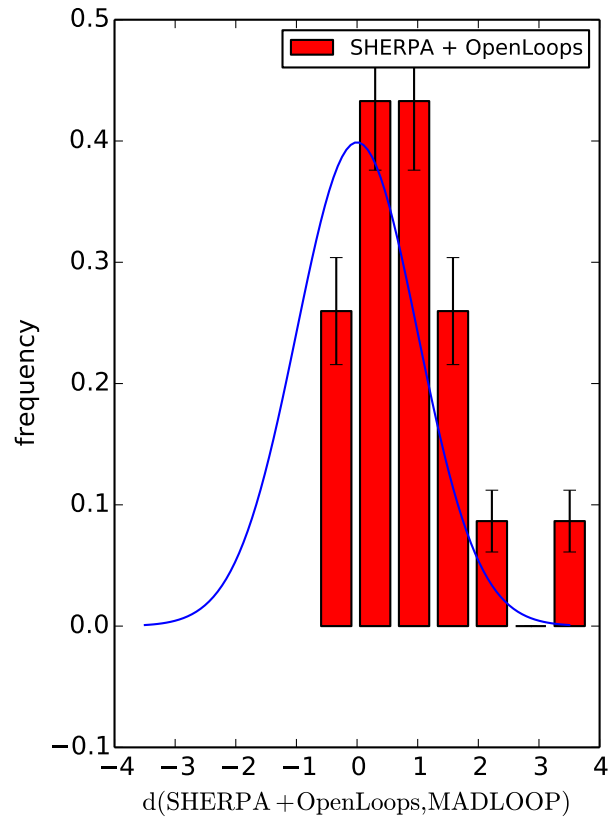
Figure 3.2: The d(SHERPA + OPENLOOPS, MADLOOP) for the processes presented in Tab. 3.5. These are compared to a Gaussian distribution, with both the curve and histogram normalised to unit area. The uncertainties on the histogram are statistical, and d(A, B) is defined in Eq. (3.2).

independent calculations. Fig. 3.2 shows the same plot for the NLO QCD cross-section calculation, between SHERPA + OPENLOOPS and MADLOOP. Again, within the statistics available, the d(A, B) distribution is compatible with the Gaussian distribution.

3.5 Conclusions

This chapter presents the validation of the interface between SHERPA and the one-loop provider OPENLOOPS, which will used in subsequent chapters for phenomenological studies. LO cross-sections were compared between AMEGIC++, COMIX and MADGRAPH as a check that the set-up and cuts were identical, before full NLO QCD cross-sections were compared. Good agreement was found across a broad range of processes between the SHERPA + OPENLOOPS interface and MADLOOP. This included processes with several different physics and technical challenges, such as a highly coloured final states, high multiplicities and heavy coloured particles. Some Higgs boson production channels were also included in this chapter.

At both LO and NLO QCD, the distributions of d(X, Y) were binned and compared to a Gaussian distribution, with both the histogram and the Gaussian being normalised to unit area. For the low statistics available, the histograms of the differences were compatible with the expected Gaussian distribution.

Chapter 4

Numerical EW Sudakov Corrections

This chapter details the numerical implementation of the EW Sudakov formalism in the SHERPA framework. This provides an efficient way of approximating the high-energy limit of the exact NLO EW corrections. The implementation applies the correction as a K-factor to the squared amplitude at each phase-space point evaluated. Cross-sections are presented for some simple processes and compared to literature values, along with some initial results.

4.1   Introduction

In the present era of precision physics, with the LHC frequently probing precision of $\mathcal{O}(1\,\%)$, there is a significant pressure on theorists to produce the required precision in simulations. With this motivation, Chap. 3 focussed on validating the SHERPA + OPENLOOPS interface for calculations of total cross-sections to NLO in QCD. Chap. 5 uses this interface in some phenomenological studies of EW SM processes, employing the S-MC@NLO and MEPS@NLO technology introduced in Chap. 2 to match to a parton shower. This set-up, NLO QCD ME merging, is the current state of the art in precision of Monte Carlo event generators. However, as the precision of experiments continues to improve, moving beyond the NLO QCD approxi-
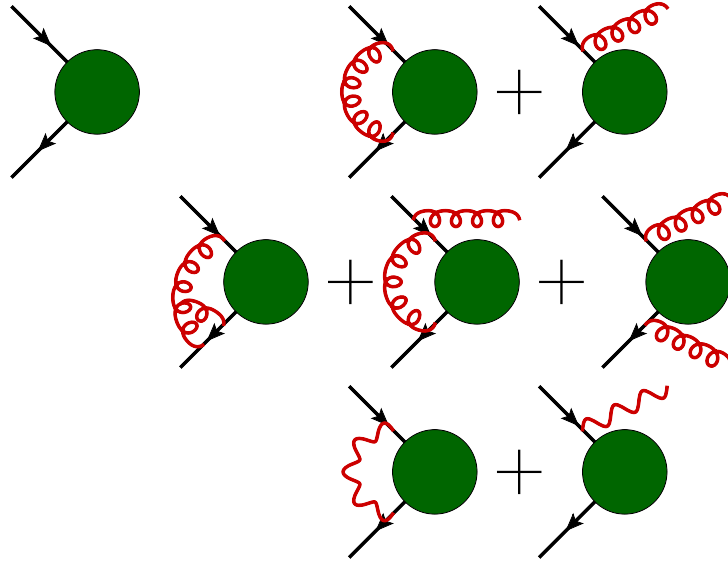
Figure 4.1: Diagrammatic representation of NLO QCD (top right hand side), NNLO QCD (middle) and NLO EW (bottom) for an arbitrary Born process (top left)

mation becomes increasingly important. As introduced in Chap. 1, there is currently interest in developing NNLO accurate Monte Carlo simulations [26–37, 42–44], at which precision NLO EW corrections become important. In some cases NLO EW corrections can even form the dominant correction, such as Higgs boson production via WBF. It is therefore well motivated to consider the effect of NLO EW corrections alongside NNLO QCD, and an exact NLO EW calculation is implemented within the SHERPA framework [47] with OPENLOOPS providing the virtual diagrams. However, the exact NLO EW computation is very CPU intensive, and often an approximation is sufficiently accurate, especially in event generation. This chapter focuses on increasing the precision in EW of processes in the SM via the implementation of high energy EW Sudakov approximation to the exact NLO EW calculation.

Chap. 1 introduced the concept of EW Sudakov logarithms as a high-energy approximation to the exact NLO EW calculation, arising as a result of the difference in the scale of the process and the mass of the EW boson. Fig. 4.1 shows example diagrams for NLO, NNLO QCD corrections and EW NLO corrections to an arbitrary Born process. The structure of the NLO QCD calculation is mirrored in the NLO EW case. However, a difference between NLO QCD and NLO EW is highlighted in Fig. 4.2. This shows the decay of
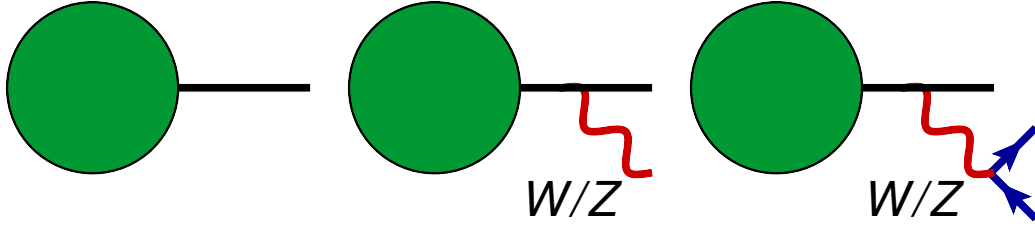
Figure 4.2: Diagram showing the decay of real emission of weak bosons that allow it to be categorised as a distinct process.

the real radiation of weak bosons to observable particles, which allows it to be theoretically consistently separated from the rest of the NLO EW calculation as a distinct process. This leaves the virtual diagrams uncancelled by any real emission, and physically observable. However, if an analysis is inclusive with respect to the decay products of the real emission term, these diagrams can be included at LO in the calculation as a separate process, as discussed in Chap. 1.

As is expected from the form of the logarithms, the main effect of the Sudakov logarithms is in the high transverse momentum, high-$p_\perp$, tail of distributions. This high-$p_\perp$ tail is an important feature to understand correctly as heavy new resonances can show up in this region of phase-space. As well as this, there is an angular contribution to the Sudakov corrections which introduces shape changes in angular distributions, which can impact the decay plane of a heavy resonance.

The implementation detailed in this chapter follows the general algorithm for calculating these logarithms as formulated by S. Pozzorini and A. Denner [48]. This general algorithm for the inclusion of EW Sudakov corrections is also implemented in the ALPGEN ME generator [59].

4.2 Relevant Diagrams

The relevant diagrams that lead to these large logarithms are those that suffer from mass singularities [126]. These divergent structures are illustrated in Fig. 4.3. These arise from the collinear and soft limits of the boson emission, which become divergent in the limit of vanishing mass of the ex-
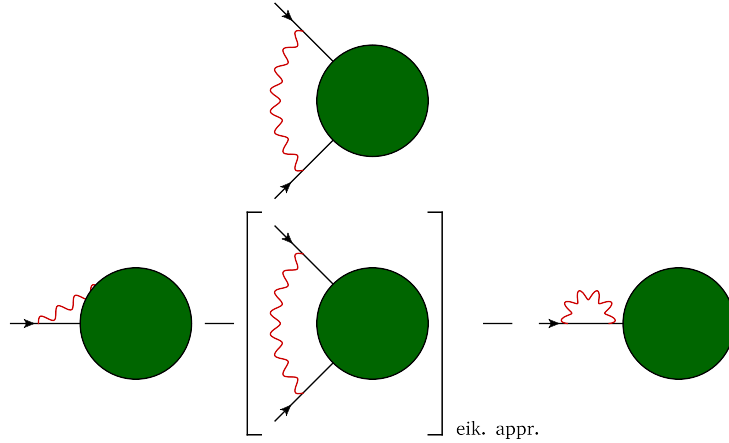
Figure 4.3: Diagrams contributing to large logarithms. Above is the soft, collinear exchange between two external legs, and below is the collinear contribution, with the double counting with the soft-collinear and wavefunction renormalisation contributions subtracted. The second term in the lower diagram is evaluated in the eikonal approximation.

changed boson. The two diagrams in Fig. 4.3 represent the categories of these divergences. The upper diagram illustrates a contribution to the double-logarithmic, soft and collinear divergences, which arise when an external line emits an EW particle, which is absorbed by a second external line. The lower diagram in Fig. 4.3 illustrates the emission of an EW particle from an external line into an internal line of the process. The soft-collinear contribution, such as those included in the upper diagram of Fig. 4.3, are removed. This leaves a collinear divergent structure, which contributes only a single logarithm to the correction.

Soft divergences, which are subtracted in Fig. 4.3, occur when the emitted boson is reabsorbed by the emitting external line. The logarithms introduced by this procedure are accounted for by a field renormalisation. These introduce single logarithmic corrections, and are included alongside the collinear single logarithms in this implementation. However, other forms of single logarithms arising from renormalisation of EW parameters, labelled in this chapter and in Ref. [48] as parameter logarithms, are included separately. These parameter logarithms naturally fall out of the calculation of the process with the EW parameters at the new, high scale.

For the exchange of an EW boson between external lines, as in the upper diagram of Fig. 4.3, it is clear that the logarithm is independent of the underlying

process. However, the factorisation of the collinear logarithms is not obvious, even at high energies, where the symmetric part of the EW Lagrangian is dominant. Ref. [49] demonstrates the factorisation of the collinear logarithms in all cases, and therefore shows that it is possible to calculate both the single and double logarithms without any detailed information about the underlying process. The only necessary information comes from the external lines, with the exception of the parameter renormalisation logarithms, which must be approached differently as described in Subsec. 4.4.3.

In the high-energy limit, where the EW Sudakov logarithms dominate the exact NLO EW result, the single logarithms have a smaller effect than the double, soft-collinear logarithms. However, at currently accessible energies and energies that will become accessible in the near future, the single logarithms still provide a significant contribution to the total EW Sudakov correction. They are typically $\mathcal{O}(1\,\%)$ of the LO cross section at energies $\sim 1\,\mathrm{TeV}$, compared to $\mathcal{O}(10\,\%)$ for double logarithms. Furthermore, in the $2 \to 2$ process for four fermions at $1\,\mathrm{TeV}$, the single logarithms are the dominant correction, larger than the double logarithms [127]. Because the single logarithms are typically positive in sign, whereas the double logarithms are negative, the single logarithms must be included to prevent the overall prediction for the EW Sudakov correction from becoming too negative. It is therefore important to consider the contribution of both diagrams in Fig. 4.3 to the EW Sudakov approximation.

4.3   Notation

The notation used in this chapter is inspired by the Denner and Pozzorini paper, Ref. [48], which concisely presents the universal structure of EW logarithms.

The Sudakov corrections can be applied to the calculations at the amplitude level. The EW Sudakov corrected Born ME, $\mathcal{M}_{\mathrm{EW}}^{i_1...i_n}$, to an original process $\mathcal{M}_{\mathrm{LO}}^{i_1...i_n}$ with external lines $[i_1...i_n]$ can be expressed by some perturbation, $\delta\mathcal{M}_{\mathrm{EW}}^{i_1...i_n}$, to the original Born ME $\mathcal{M}_{\mathrm{LO}}^{i_1...i_n}$ as in Eq. (4.1). For all external lines defined by convention to be incoming,

$$\mathcal{M}_{\mathrm{EW}}^{i_1..i_n} = \mathcal{M}_{\mathrm{LO}}^{i_1...i_n} + \delta\mathcal{M}_{\mathrm{EW}}^{i_1...i_n} \,, \tag{4.1}$$

and therefore the squared amplitude can be written as

$$\begin{aligned}
|\mathcal{M}_{\mathrm{EW}}^{i_1...i_n}|^2 &= |\mathcal{M}_{\mathrm{LO}}^{i_1...i_n} + \delta\mathcal{M}_{\mathrm{EW}}^{i_1...i_n}|^2 \\
&= |\mathcal{M}_{\mathrm{LO}}^{i_1...i_n}|^2 + 2\Re\left[\mathcal{M}_{\mathrm{LO}}^{*i_1...i_n}\delta\mathcal{M}_{\mathrm{EW}}^{i_1...i_n}\right] + \mathcal{O}(\{\delta\mathcal{M}_{\mathrm{EW}}^{i_1...i_n}\}^2) \,.
\end{aligned} \tag{4.2}$$

It is at this amplitude squared level that a K-factor can be introduced. The transformed squared ME, $|\mathcal{M}_{\mathrm{EW}}^{i_1...i_n}|^2$, can be written as

$$|\mathcal{M}_{\mathrm{EW}}^{i_1...i_n}|^2 = (1 + \mathrm{K}_{\mathrm{EW}})|\mathcal{M}_{\mathrm{LO}}^{i_1...i_n}|^2 \,. \tag{4.3}$$

This chapter details the implementation of the calculation of K_{EW} in Eq. (4.3) for any arbitrary EW process with SHERPA. By a comparison between Eqs. (4.2) and (4.3), it can be seen that

$$\mathrm{K}_{\mathrm{EW}} = \frac{2\Re[\mathcal{M}_{\mathrm{LO}}^{*i_1...i_n}\delta\mathcal{M}_{\mathrm{EW}}^{i_1...i_n}]}{|\mathcal{M}_{\mathrm{LO}}^{i_1...i_n}|^2} + \mathcal{O}(\{\delta\mathcal{M}_{\mathrm{EW}}^{i_1...i_n}\}^2) \,. \tag{4.4}$$

The term $\mathcal{O}(\{\delta\mathcal{M}_{\mathrm{EW}}^{i_1...i_n}\}^2)$ is neglected in this implementation as subleading. K_{EW} is the calculated quantity in this implementation of EW Sudakov logarithms. This is calculated for each phase-space point evaluated, and multiplied to the squared Born amplitude.

There are three distinct categories from which the EW Sudakov logarithms can arise. These are the double logarithms that arise from soft-collinear emission, $\mathrm{K}_{\mathrm{EW}}^{\mathrm{SC}}$, single logarithms, $\mathrm{K}_{\mathrm{EW}}^{\mathrm{C}}$, and single logarithms arising from parameter renormalisation, $\mathrm{K}_{\mathrm{EW}}^{\mathrm{PR}}$. Therefore, K_{EW} is decomposed as

$$\begin{aligned}
\mathrm{K}_{\mathrm{EW}} &= \mathrm{K}_{\mathrm{EW}}^{\mathrm{SC}} + \mathrm{K}_{\mathrm{EW}}^{\mathrm{C}} + \mathrm{K}_{\mathrm{EW}}^{\mathrm{PR}} \\
&= \frac{2\Re[\mathcal{M}_{\mathrm{LO}}^{*i_1...i_n}\left(\delta\mathcal{M}_{\mathrm{EW}}^{\mathrm{SC}i_1...i_n} + \delta\mathcal{M}_{\mathrm{EW}}^{\mathrm{C}i_1...i_n} + \delta\mathcal{M}_{\mathrm{EW}}^{\mathrm{PR}i_1...i_n}\right)]}{|\mathcal{M}_{\mathrm{LO}}^{i_1...i_n}|^2} \,.
\end{aligned} \tag{4.5}$$

The $\delta\mathcal{M}_{\mathrm{EW}}^{\mathrm{X}i_1...i_n}$ terms in Eq. (4.5) are the relevant correction terms for the corresponding $\mathrm{K}_{\mathrm{EW}}^{\mathrm{X}}$.
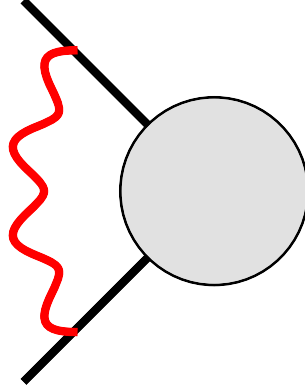
Figure 4.4: The form of diagrams that contribute to the soft-collinear double logarithms in the Sudakov approximation.

4.4 Implementation of K-factors

From Eq. (4.5), it is possible to describe the individual contributions from the three different forms of EW Sudakov logarithm. This section describes the implementation of the K_{EW}^{SC}, K_{EW}^{C} and K_{EW}^{PR} components, which can be treated entirely independently in this approach. Once all of the corrections have been calculated, the final result, K_{EW}, is simply the sum of the components. The Sudakov implementation in SHERPA does not affect any part of the event generation, other than the ME weighting. The following subsections detail the implementation of each different contribution to the EW Sudakov approximation. Where applicable, the longitudinal polarisations of the weak bosons are treated with the Goldstone boson equivalence theorem. This implies the substitutions

$$\mathcal{M}^{W_L^{\pm}} = \mathcal{M}^{\phi^{\pm}}, \qquad (4.6)$$
$$\mathcal{M}^{Z_L^{\pm}} = i\mathcal{M}^{\chi}, \qquad (4.7)$$

for some ME, $\mathcal{M}$, with longitudinal gauge boson, $W_L^{\pm}, Z_L$, replaced by the appropriate Goldstone boson, $\phi^{\pm}, \chi$.

4.4.1 Soft-Collinear Logarithms

The double logarithms, which arise from diagrams such as those in Fig. 4.4, provide the $\mathrm{K}_{\mathrm{EW}}^{\mathrm{SC}}$ contribution. These corrections include logarithms, L_V, for each EW boson V, of

$$L_V(|(p_l + p_k)^2|) = \log^2\left(\frac{|(p_l + p_k)^2|}{M_V^2}\right), \tag{4.8}$$

where p_l, p_k are the momenta of external legs, l and k, involved in the EW boson exchange. Extracting the $\mathrm{K}_{\mathrm{EW}}^{\mathrm{SC}}$ terms from Eq. (4.5) gives

$$\mathrm{K}_{\mathrm{EW}}^{\mathrm{SC}} = \frac{2\Re\left[\mathcal{M}_{\mathrm{LO}}^* \delta\mathcal{M}_{\mathrm{EW}}^{\mathrm{SC}}\right]}{|\mathcal{M}_{\mathrm{LO}}|^2}, \tag{4.9}$$

where the external lines are not labelled explicitly for clarity. As $\mathcal{M}_{\mathrm{LO}}$ is known as the original Born term, calculating $\mathrm{K}_{\mathrm{EW}}^{\mathrm{SC}}$ relies on the calculation of $\delta\mathcal{M}_{\mathrm{EW}}^{\mathrm{SC}}$. This can be expressed as a combination of EW couplings, logarithms of the form $L_V(|(p_l + p_k)^2|)$ and an underlying ME, $\mathcal{M}_0$. This underlying ME is not necessarily equivalent to $\mathcal{M}_{\mathrm{LO}}$, since the exchange of a weak boson, $W^\pm$, Z can lead to flavour changes in the external lines.

Summing over all possible exchanges of EW bosons, V, between all possible combinations of external lines, l and k,

$$\delta\mathcal{M}_{\mathrm{EW}}^{\mathrm{SC}\,i_1\ldots i_n} = \frac{\alpha}{4\pi}\sum_l\sum_{k<l}\sum_V \mathcal{M}_0^{i_1\ldots i_{l'}\ldots i_{k'}\ldots i_n} g_{i_{l'}i_l}^V g_{i_{k'}i_k}^{\overline{V}} L_V(|(p_l + p_k)^2|), \tag{4.10}$$

where $g_{i_{l'}i_l}^V$ represents the coupling of boson V to external line i_l, which is transformed by the EW vertex into line $i_{l'}$. It is possible, for example in the case of photons, for $i_{l'} = i_l$, although this is not the case in general. The soft-collinear contribution to the EW Sudakov correction can be implemented in the form of Eq. (4.10); however, the dominant correction can be obtained in such a way that it does not depend on the external momenta. It is simple

see from Eq. (4.8) that

$$
\begin{aligned}
L_V(|(p_l + p_k)^2|) &= \left[\log\left(\frac{\hat{s}}{M_V^2}\right) + \log\left(\frac{|(p_l + p_k)^2|}{\hat{s}}\right) \right]^2 \\
&= \log^2\left(\frac{\hat{s}}{M_V^2}\right) + 2\log\left(\frac{\hat{s}}{M_V^2}\right)\log\left(\frac{|(p_l + p_k)^2|}{\hat{s}}\right) \qquad (4.11) \\
&\quad + \text{terms with no large logarithms} \, .
\end{aligned}
$$

It is important to notice that Eq. (4.11) neglects the final term, $\log^2\left(\frac{|(p_l+p_k)^2|}{\hat{s}}\right)$, which uses the assumption that $|(p_l + p_k)|^2 \sim \hat{s} \gg M_V^2$, such that this is not a large logarithmic contribution. For the first two terms on the right-most hand-side of Eq. (4.11), the first is $L_V(\hat{s})$, and the second is defined to be

$$
2\log\left(\frac{\hat{s}}{M_V^2}\right)\log\left(\frac{|(p_l + p_k)^2|}{\hat{s}}\right) \equiv L_V^{\text{SSC}}(\hat{s}) \, . \qquad (4.12)
$$

Including these logarithms in Eq. (4.10) gives,

$$
\delta\mathcal{M}_{\text{EW}}^{\text{SC}i_1\ldots i_n} = \frac{\alpha}{4\pi} \sum_l \sum_{k<l} \sum_V \mathcal{M}_0^{i_1\ldots i_{l'}\ldots i_{k'}\ldots i_n} g_{i_{l'}i_l}^V g_{i_{k'}i_k}^{\overline{V}} \left[L_V(\hat{s}) + L_V^{\text{SSC}}(\hat{s}) \right] \, . \qquad (4.13)
$$

It is clear that the first term on the right-hand side of Eq. (4.13) provides the leading Sudakov correction, while the second term reduces to a single logarithmic contribution. It is noticed in Ref. [48], that the invariance of the S-matrix under global SU(2) transformations implies that this leading contribution, $\delta\mathcal{M}_{\text{EW}}^{\text{LSC}i_1\ldots i_n}$, can be rewritten as

$$
\delta\mathcal{M}_{\text{EW}}^{\text{LSC}i_1\ldots i_n} = -\frac{\alpha}{8\pi} \sum_l \sum_V \mathcal{M}_0^{i_1\ldots i_{l'}\ldots i_n} g_{i_{l'}i_l}^V g_{i_{l'}i_l}^{\overline{V}} L_V(\hat{s}) \, . \qquad (4.14)
$$

An advantage of this re-expression is that the sum now only runs over single external legs. This greatly simplifies the calculation, as well as reducing the number of potential flavour changes in $\mathcal{M}_0$, which must be calculated. A similar trick cannot be employed for the second, subleading term, which can be labelled $\delta\mathcal{M}_{\text{EW}}^{\text{SSC}i_1\ldots i_n}$, since this contains a dependence on momenta of the external lines, which is not a global property.

One remaining simplification to be made, in line with Ref. [48], is to relate all Sudakov logarithms to the same weak boson mass. This is chosen to be

M_W, and naturally introduces logarithms of the ratio of EW boson masses. While this difference is small for the Z boson, the photon is massless and this therefore includes a divergence. This divergence is the consequence of the necessity of an exact NLO calculation in QED. For this implementation of EW Sudakov logarithms, the photon is given a fictitious mass, M_W, and the logarithms resulting from the difference between this mass and the actual photon mass are not included. An exact NLO QED calculation should be performed if these effects become important.

Introducing this into $\delta\mathcal{M}_{\mathrm{EW}}^{\mathrm{LSC}i_1...i_n}$ gives

$$\delta\mathcal{M}_{\mathrm{EW}}^{\mathrm{LSC}i_1...i_n} =$$
$$-\frac{\alpha}{8\pi}\sum_l\sum_V \mathcal{M}_0^{i_1...i_{l'}...i_n} g_{i_{l'}i_l}^V g_{i_{l'}i_l}^{\overline{V}} \left[L_W(\hat{s}) + 2\log\left(\frac{\hat{s}}{M_W^2}\right)\log\left(\frac{M_W^2}{M_V^2}\right)\right],$$
$$(4.15)$$

where the latter term on the right-hand side only contributes when $V = Z$, and the term $\sim \log^2\left(\frac{M_W^2}{M_V^2}\right)$ is neglected completely as it has no large logarithms. The same substitution in $\delta\mathcal{M}_{\mathrm{EW}}^{\mathrm{SSC}}$ yields no large logarithms containing $\log\left(\frac{M_W^2}{M_V^2}\right)$. In Eq. (4.15), $L_W(\hat{s})$ denotes $L_V(\hat{s})$ with $M_V \to M_W$.

To summarise this section, the soft-collinear contribution to the Sudakov logarithms consists of two parts:

$$\delta\mathcal{M}_{\mathrm{EW}}^{\mathrm{SC}i_1...i_n} = \delta\mathcal{M}_{\mathrm{EW}}^{\mathrm{LSC}i_1...i_n} + \delta\mathcal{M}_{\mathrm{EW}}^{\mathrm{SSC}i_1...i_n}, \qquad (4.16)$$

with

$$\delta\mathcal{M}_{\mathrm{EW}}^{\mathrm{LSC}i_1...i_n} = -\frac{\alpha}{8\pi}\sum_l\sum_V \mathcal{M}_0^{i_1...i_{l'}...i_n} g_{i_{l'}i_l}^V g_{i_{l'}i_l}^{\overline{V}}$$
$$\left[\log^2\left(\frac{\hat{s}}{M_W^2}\right) + 2\log\left(\frac{\hat{s}}{M_W^2}\right)\log\left(\frac{M_W^2}{M_V^2}\right)\right] \qquad (4.17)$$
$$\delta\mathcal{M}_{\mathrm{EW}}^{\mathrm{SSC}i_1...i_n} = \frac{\alpha}{2\pi}\sum_l\sum_{k<l}\sum_V \mathcal{M}_0^{i_1...i_{l'}...i_{k'}...i_n} g_{i_{l'}i_l}^V g_{i_{k'}i_k}^{\overline{V}}$$
$$\log\left(\frac{\hat{s}}{M_W^2}\right)\log\left(\frac{|(p_l + p_k)^2|}{\hat{s}}\right). \qquad (4.18)$$

Appendix B lists the explicit look-up values for Δ_X, where $X = \mathrm{LSC, SSC}$,

and Eqs. (4.17) and (4.18) are expressed as

$$\delta\mathcal{M}_{\text{EW}}^{\text{LSC}i_1\ldots i_n} = -\frac{\alpha}{4\pi}\sum_l\sum_V \Delta_{\text{LSC}}(i_l, V)\mathcal{M}_0^{i_1\ldots i_{l'}\ldots i_n}$$
$$\left[\log^2\left(\frac{\hat{s}}{M_W^2}\right) + 2\log\left(\frac{\hat{s}}{M_W^2}\right)\log\left(\frac{M_W^2}{M_V^2}\right)\right] \tag{4.19}$$

$$\delta\mathcal{M}_{\text{EW}}^{\text{SSC}i_1\ldots i_n} = \frac{\alpha}{4\pi}\sum_l\sum_{k<l}\sum_V \Delta_{\text{SSC}}(i_l, V)\Delta_{\text{SSC}}(i_k\overline{V})\mathcal{M}_0^{i_1\ldots i_{l'}\ldots i_{k'}\ldots i_n}$$
$$\log\left(\frac{\hat{s}}{M_W^2}\right)\log\left(\frac{|(p_l + p_k)^2|}{\hat{s}}\right) . \tag{4.20}$$

Flavour Changes

The underlying Born term, $\mathcal{M}_0$, can potentially have differently flavoured external legs to that of the $\mathcal{M}_{\text{LO}}$. Flavour, as discussed in this chapter, is the type of particle being considered. Since the leading soft-collinear corrections can be expressed in terms of the summation over single legs, the only potential alteration to the Born process is $Z \leftrightarrow \gamma$ interference as a result of $W^\pm$ boson loops. For the subleading calculation, any process involving a $W^\pm$ boson emission also introduces a flavour-changed $\mathcal{M}_0$. This forces a full EW family of processes to be calculated alongside the original Born process. Additionally, Z boson emission can introduce flavour changes in the Higgs sector. Pure QED loops cannot introduce a flavour-changed $\mathcal{M}_0$. Therefore, for the contribution from photons, $\Re\left[\mathcal{M}_{\text{LO}}^*\mathcal{M}_0\right]/|\mathcal{M}_{\text{LO}}|^2 = 1$ and does not need to be explicitly calculated, simplifying the calculation of the K-factor in this case.

Technical Issues

The leading soft-collinear corrections are the largest contribution to the Sudakov high-energy approximation. Since it only depends on global variables, such as $\hat{s}$, the implementation of these logarithms is simple. The external particles are looped over and the relevant coefficient is found from a look-up table of values (see Appendix B). These are related to the couplings of the particles to the EW bosons. This value is then multiplied by the common logarithm to the correction, $\log\left(\frac{\hat{s}}{M_W^2}\right)$.

As the couplings of the weak bosons are dependent on the helicities of the external particles, the amplitude corrected by the K-factor must be decomposed into each spin structure for both the $W^\pm$ and Z boson contributions, which are each corrected by their relevant factor. This corrected amplitude is then included as $\delta\mathcal{M}_{\text{EW}}$ in $K_{\text{EW}}^{\text{LSC}}$.

Another issue for the leading soft-collinear correction is that of the potential flavour changes to the underlying Born process, $Z \leftrightarrow \gamma$. This involves calculating the flavour-changed process, provided that the transformed flavour combination is permitted. For this interference, both the flavour-changed and original ME must be considered, in proportion to their contributions to the total cross section. This is naturally included in the calculation if both possible amplitudes are added linearly. As the mass of the Z boson and the photon are so very different, the flavour change between these will force the particle off-shell. It is therefore necessary to redistribute the momenta in order to put all external particles back on-shell. As only one external particle at a time can potentially be affected by the correction, the recoil from putting this particle on-shell must be distributed in a consistent way between the remaining external particles. There are multiple ways in which this can be achieved, but in this implementation the recoil is shared between all final state particles, while the directions of the momenta are preserved.

For the subleading soft-collinear correction, there are similar concerns. Similarly to the leading case, the coefficients to the logarithms are found with a look-up table of values, which are related to the couplings. The amplitude must again be decomposed into its helicity components, with the coefficients to the logarithms being calculated for each configuration independently for $W^\pm$ and Z boson corrections. Of all the Sudakov logarithms implemented, the subleading soft-collinear logarithms are the most CPU intensive. It can, therefore, be beneficial to perform calculations with just the leading soft-collinear logarithms and the single logarithms, in cases where the angular dependence is not significant.

While flavour changes are common in the subleading logarithms, these are often between massless fermions, and therefore no external line is forced off-shell by the change. However, for $W^\pm$ bosons, as well as potentially external Z and H bosons and the consideration of massive fermions, a change in mass

can occur. In these cases, by the same reasoning as for the double logarithms, the momenta must be redistributed. For the subleading soft-collinear correction, the calculation remains over pairs of external particles. This allows the momentum redistribution to be kept between the two particles involved in the correction, again while preserving the directions of the momenta.

Because the subleading soft-collinear contribution to the EW Sudakov correction includes logarithms of the form $\log\left(\frac{|(p_j+p_k)^2|}{M_W^2}\right)$, which contains a dependence on the momenta of the external particles involved, it must be calculated for each possible pair of external particles. It is also important in the subleading soft-collinear calculation to introduce a cut-off on the contribution outside of the limit $|(p_j + p_k)^2| \gg M_W^2$, where the approximation is valid. This can be done with a harsh cut-off, or with some damping function. The differences introduced in the distributions by a different choice of cut-off is a source of uncertainty in the implementation. In the SHERPA implementation of the EW Sudakov approximation, there is a hard cut-off implemented in the subleading soft-collinear logarithms, for this validation, at $|(p_j+p_k)^2| = M_W^2$. Further to this, no correction is applied to any phase-space point for which $\hat{s} < M_W^2$. This second condition applies for all classes of logarithms considered, the single soft or collinear and parameter renormalisation, as well as the double logarithms.

The region in which the approximation theoretically no longer holds can be explicitly removed by the multiplication of the correction between any two external lines, i and j, by a factor, F, which is either 1 or 0 according to

$$F = \Theta\left(\frac{|(p_i + p_j)^2| - p_i^2 - p_j^2}{2|p_i||p_j|} - \cos\left[\frac{M_W^2}{\hat{s}}\right]\right), \qquad (4.21)$$

where p_i denotes the momentum of external line i, and Θ is the step function. The affect of choosing a different cut-off for the subleading double logarithms is negligible.

4.4.2 Single Soft or Collinear Logarithms

The type of diagram that gives rise to single collinear logarithms is given in Fig. 4.5, with the double-counting of the soft-collinear divergences appropri-
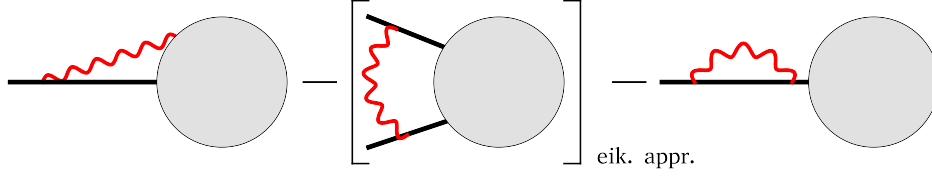
Figure 4.5: Structure of diagrams leading to single collinear logarithmic corrections. The soft-collinear and soft divergences are subtracted from the general form on the left-hand-side. Wavefunction renormalisation logarithms are then included on top of this contribution.

ately subtracted in the collinear limit, as discussed in Sec. 4.2. The contributions to the EW Sudakov approximation considered in this subsection are the collinear single logarithms and the field renormalisation logarithms. These logarithms are calculated in Ref. [49] for each EW particle. The general form for these corrections is

$$
\mathrm{K}_{\mathrm{EW}}^{\mathrm{C}} = \frac{\alpha}{4\pi} \sum_{j} \sum_{V} \Delta_{\mathrm{C}}(i_j, V) \frac{2\Re[\mathcal{M}_{\mathrm{LO}}^* \mathcal{M}_0^{i_1 \ldots i_j' \ldots i_n}]}{|\mathcal{M}_{\mathrm{LO}}|^2} L_V(\hat{s}) \,. \tag{4.22}
$$

The same transformation can now be applied as in the soft-collinear case, such that $L_V(\hat{s}) \to L_W(\hat{s})$. This does not introduce any other large logarithms, and so this is simply a substitution in Eq. (4.22). Further, the summation over all EW bosons can be performed in Eq. (4.22), such that $\sum_V \Delta_{\mathrm{C}}(i_j, V) = \Delta_{\mathrm{C}}(i_j) \sim C(i_j)$, where $C(i_j)$ is the Casimir operator of the group for external line i_j. This yields

$$
\mathrm{K}_{\mathrm{EW}}^{\mathrm{C}} = \frac{\alpha}{4\pi} \sum_{j} \Delta_{\mathrm{C}}(i_j) \frac{2\Re[\mathcal{M}_{\mathrm{LO}}^* \mathcal{M}_0^{i_1 \ldots i_j' \ldots i_n}]}{|\mathcal{M}_{\mathrm{LO}}|^2} L_W(\hat{s}) \,. \tag{4.23}
$$

Appendix B lists the coefficients for Δ_{C}, for Eq. (4.23).

Flavour Changes

Because the summation is of a similar form to the leading soft-collinear correction, the flavour changes for $\mathcal{M}_0$ are also similar. However, the renormalisation conditions forbid mixing from final state physical photons with Z bosons.

Technical Issues

The issues for the single logarithms are the same as those for the leading soft-collinear logarithms. A coefficient is found from a look-up table relevant for each particle, for each relevant helicity combination in the amplitude. For the few cases where the underlying process, $\mathcal{M}_0$, includes a flavour-changed interference, this amplitude is calculated with the altered flavour combination with the appropriate momentum redistribution.

4.4.3   Parameter Renormalisation Logarithms

The final type of logarithm to contribute to the Sudakov logarithms are those arising from the running of the EW couplings from the weak scale up to a high scale, taken for convenience to be the centre-of-mass energy of the collision. These parameter renormalisation logarithms differ from the other considered logarithms in that they depend on the internal structure of the process. The Born ME must be multiplied by a factor depending on the number of each EW coupling present in the amplitude. This amounts to recalculating the process at the higher scale. Therefore, the implementation of $\mathrm{K}_{\mathrm{EW}}^{\mathrm{PR}}$ is

$$\mathrm{K}_{\mathrm{EW}}^{\mathrm{PR}} = \frac{2\Re\left[\mathcal{M}_{\mathrm{LO}}^* \mathcal{M}_0\right]}{|\mathcal{M}_{\mathrm{LO}}|^2}, \tag{4.24}$$

where $\mathcal{M}_0 = \mathcal{M}_{\mathrm{LO}}(\sqrt{\hat{s}})$, with the dependence on the ME on the scale at which couplings are evaluated shown explicitly. Therefore, $\mathrm{K}_{\mathrm{EW}}^{\mathrm{PR}}$ can be written, with scale dependencies explicit on the right-hand-side, as

$$\mathrm{K}_{\mathrm{EW}}^{\mathrm{PR}} = \frac{2\Re\left[\mathcal{M}_{\mathrm{LO}}^*(Q)\mathcal{M}_{\mathrm{LO}}(\sqrt{\hat{s}})\right]}{|\mathcal{M}_{\mathrm{LO}}(Q)|^2}, \tag{4.25}$$

where Q is the original scale of the EW couplings. The EW couplings considered to have a scale dependence, and are therefore running couplings within this implementation, are the QED coupling, the weak mixing angle and Yukawa couplings.

Technical Issues

The parameter renormalisation logarithms cannot be so easily separated from the rest of the process as the other logarithms. This is because the logarithms that arise depend on the details of the internal couplings and not simply the external particles of the process. The calculation of these logarithms requires the reinitialisation of the process with EW parameters run up to a high scale, the centre-of-mass energy of the process. The ratio of the evolved ME and the original ME then provides the logarithmic correction.

There is no alteration to the final state particles in the parameter renormalisation logarithms, and it is not necessary to decompose the ME into its helicity components, because this is taken correctly into account with the reinitialisation of the process with the evolved EW parameters. However, even though the flavour of the particles will not change, the mass of the EW bosons will change when the parameters are evolved up to the high scale. Therefore, any external weak boson will be pushed off its mass-shell. This requires a momentum redistribution similar to that of the leading soft-collinear and single logarithms.

4.4.4 Current Limitations

There are a couple of limitations to the current implementation of the EW Sudakov approximation in SHERPA. These are briefly discussed in this subsection.

Massive Fermions

The MEs accessed by the EW Sudakov correction come as a summation of helicity amplitudes. The correction is then applied to each helicity amplitude separately, since the weak bosons are not blind to handedness. For massive fermions, such as top quarks and potentially b-quarks, c-quarks and τ-leptons[1], it is possible to conceive of a Lorentz boost that inverts the helicity of the particle. Therefore, the chirality of the particle in this case, which

---

[1]Other leptons are sufficiently light as to be considered massless in Monte Carlo simulations.

is related to the transformation of the particle under the SM, is not identical to its helicity. This means that the correction will be applied to the wrong amplitude in these cases. This is a restriction on the applicability of this implementation of EW Sudakov logarithms, and is part of the extension to this project.

ME Generator

Because the couplings of the weak bosons depend on the chirality of the external lines, the K-factor must be applied to each of the helicity amplitudes independently. In SHERPA, only the COMIX ME generator, and not AMEGIC++, will allow this to be done. Therefore, this EW Sudakov implementation can only be used with the COMIX ME generator. This is not a significant restriction, however, as COMIX is the default SHERPA ME generator.

CKM Matrix and Width Schemes

As an initial implementation, the EW Sudakovs are set up with a diagonal CKM matrix and the fixed width scheme for weak bosons. There is no technical problem with extending the current implementation to also handle a general CKM matrix or the complex mass scheme, both of which are possible within SHERPA. Enabling the EW Sudakov approximation to be used with a general CKM matrix and the complex mass scheme will be completed as part of the next step in the implementation, and does not form part of this thesis.

4.5 Validation

The validation of the Sudakov logarithmic approximation to exact NLO EW calculations has been studied in many publications [59, 128–130]. This allows for a validation of this implementation of EW Sudakovs to be done both in comparison to published calculations of the EW Sudakov approximation, as well as to the exact NLO EW result. In the latter case, the EW Sudakov ap-

Observable	Cut
$p_{\perp,\ell}$	$> 25\,\mathrm{GeV}$
$p_{\perp,\mathrm{miss}}$	$> 25\,\mathrm{GeV}$
$|\eta_\ell|$	< 2.5

Table 4.1: The cuts included from Ref. [128] for $\mu^+\nu + X$ production at a 14 TeV proton-proton collider.

proximation is expected to converge to the exact NLO EW result in the high energy limit. This is nicely illustrated for total cross sections by increasing the harshness of final state cuts on $p_\perp$ or transverse mass, M_T, defined as $M_T = \sqrt{p_{\perp,\ell} p_{\perp,\mathrm{miss}}(1 - \cos(\phi_{\ell,\nu}))}$, where $p_{\perp,\ell}$ denotes the momentum of the muon, $p_{\perp,\mathrm{miss}}$ is the missing momentum vector, and $\phi_{\ell,\nu}$ is the angle in the ϕ plane between the muon and the missing energy vector.

This section presents comparisons for $\mu^+\nu_\mu$ [128], Drell-Yan [129], and $\ell^+\nu j$ [131] production at a 14 TeV LHC. Results from the SHERPA implementation of the EW Sudakov approximation are compared to published cross-sections from these papers. All uncertainties shown on the distributions in this section are statistical. The MRST2004QED LO PDF set [132] is used throughout this section, and inclusive cross-sections are presented.

4.5.1 $pp \to \mu^+\nu_\mu + X$ **Production at a 14 TeV TeV LHC**

The first process considered in this validation is $W^\pm$ production at a hadron collider. This is a simple process to consider because it only has one helicity structure for massless muons. This also follows the calculation and cuts considered in Ref. [128], where Sudakov logarithmic effects were found to be dominant in the high-M_T region.

Set-Up

The cuts applied to this process are shown in Tab. 4.1, where η is the pseudorapidity, and $p_{\perp,\mathrm{miss}}$ is a cut on the transverse momentum of the neutrino. The renormalisation, μ_r, and factorisation, μ_f, scales used for this process were $\mu_r = \mu_f = M_W$.

Parameter	Value/GeV
M_W	80.403
M_Z	91.1876
Γ_W	2.141
Γ_Z	2.4952
M_H	115
M_t	172.6
G_F	1.16637e-5

Table 4.2: The EW input parameters for the G_μ scheme used to set all EW parameters as used in Ref. [128], for masses and widths, M_X and Γ_X for particle X and Fermi constant, G_F.

The weak parameters are set with the G_μ scheme with the inputs shown in Tab. 4.2. Ref. [128] uses a non-diagonal CKM matrix (diagonal in the loops) and uses the complex mass scheme. As the EW Sudakov approximation is currently implemented in SHERPA, these settings cannot be replicated. Therefore, a diagonal CKM matrix and the fixed width scheme are used in the calculation presented in this section. These alterations make very little impact on the final results. The mass of the muon is taken into account in Ref. [128], whereas it has been neglected in the calculation presented to make the identification between helicity and chirality exact.

Fig. 4.6 shows the behaviour of the EW correction normalised to the exact NLO EW correction to inclusive $\mu^+\nu$ production at a 14 TeV LHC. The literature values shown for this validation are from a dedicated calculation of the Sudakov logarithmic corrections, and this is compared to the general purpose implementation of the Sudakov logarithms in the SHERPA framework. Fig. 4.6 shows good agreement between the two calculations of the EW Sudakov approximations, as well as showing both approximations converging to the exact NLO EW result in the high-M_T limit. This is the limit in which the process enters the Sudakov regime, in which all relevant scales, $|(p_i + p_j)^2| \gg M_W^2$, where p_i and p_j represent all relevant final state particles in the process. Small differences between the calculations of the EW Sudakov approximation occur between the calculations as a result of the different initial set-ups, as described above, and different choices made during the calculation that amount to subleading effects.
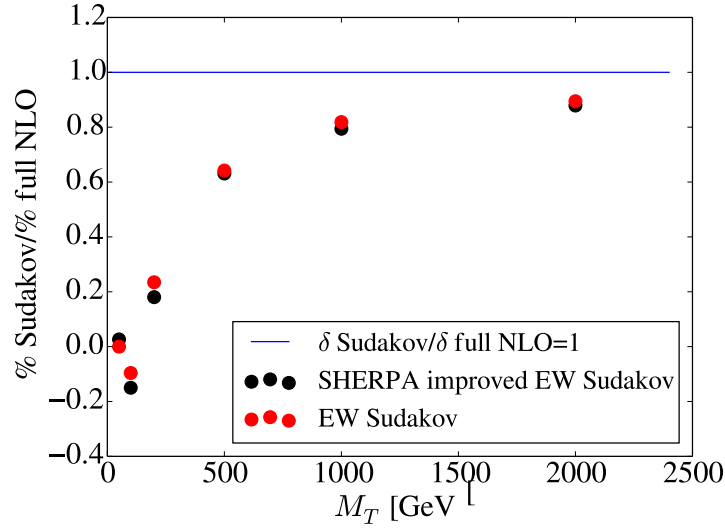
Figure 4.6: The plot of the ratio between the relative correction from the EW Sudakov approximation (literature values and SHERPA implementation shown) compared to the exact NLO EW computation, taken from Ref. [128]. This calculation is performed at 14 TeV for the LHC.

4.5.2 $pp \to \mu^+ \mu^- + X$ **Production at a 14 TeV LHC**

A second paper has been published by the same authors [129], which considers the Drell-Yan process, under similar conditions to W^+ production, which are outlined in Subsec. 4.5.1 in Tabs. 4.1 and 4.2. It is considered for a 14 TeV LHC with a scale choice of $\mu_r = \mu_f = M_Z$. One key difference to the previous validation study is that the cross-sections in this comparison are on the invariant mass of the lepton pair, as opposed to the transverse mass considered in Subsec. 4.5.1. This allows the centre-of-mass energy, $\sqrt{\hat{s}}$, to become large while other kinematic invariants are small. Therefore, the high invariant mass limit is not guaranteed to push the process into the Sudakov regime. This subsection presents a comparison between the results of Ref. [129] and the local SHERPA EW Sudakov implementation for inclusive muon pair production.

The effect of allowing these regions of phase-space into the Sudakov calculation can be seen in Fig. 4.7, the Sudakov approximation does not approach the exact NLO calculation as quickly as it did in Subsec. 4.5.1 in the high energy limit. This demonstrates the importance of removing these regions of
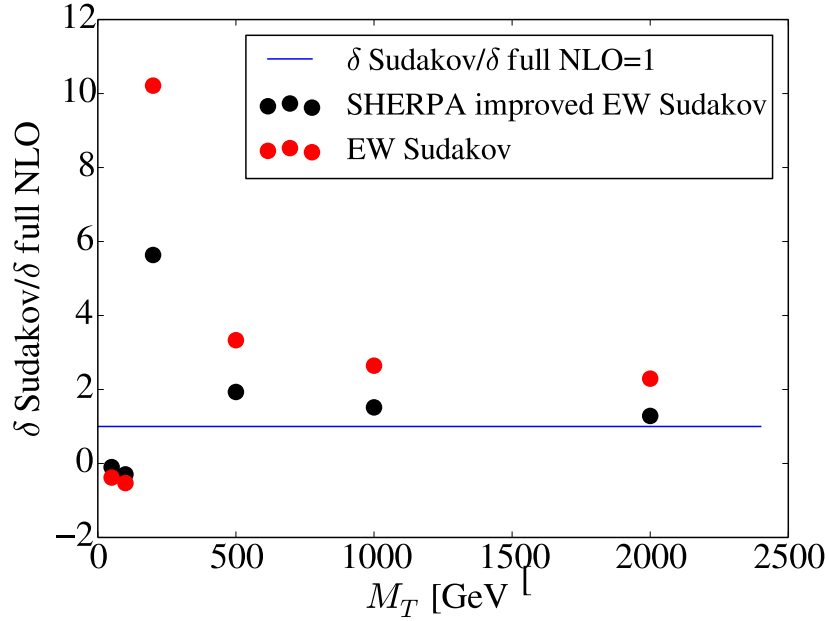
Figure 4.7:   Relative contribution of EW Sudakov logarithms from literature and SHERPA implementation normalised to the exact NLO EW correction for different cuts on invariant mass for inclusive $\mu^+\mu^-$ production at a 14 TeV LHC.

phase-space from the EW Sudakov correction. The SHERPA implementation is labelled as 'improved' in Fig. 4.7, as it does not extend into these regions of phase-space, as discussed in Subsec. 4.4.1. Therefore, the SHERPA implementation demonstrates a better convergence towards the exact NLO EW calculation than the pure EW Sudakov results presented in Ref. [129].

4.5.3 $pp \to \ell^+\nu j + X$ **Production at a 14 TeV LHC**

A further study, Ref. [131], presents an extension to $pp \to \ell^+\nu + X$ studied in Subsec. 4.5.1. This involves the consideration of an additional QCD radiation. As the Born process under consideration in Subsec. 4.5.1 was $q\bar{q}' \to \ell^+\nu$, this additional QCD radiation must introduce a gluonic external leg. As this is not charged under the EW interaction, the relevant difference between the two studies, for the EW Sudakov validation, is the altered phase-space. The process can be pushed by this radiation into regions of phase-space for which the EW Sudakov approximation does not hold, as seen in Subsec. 4.5.2.
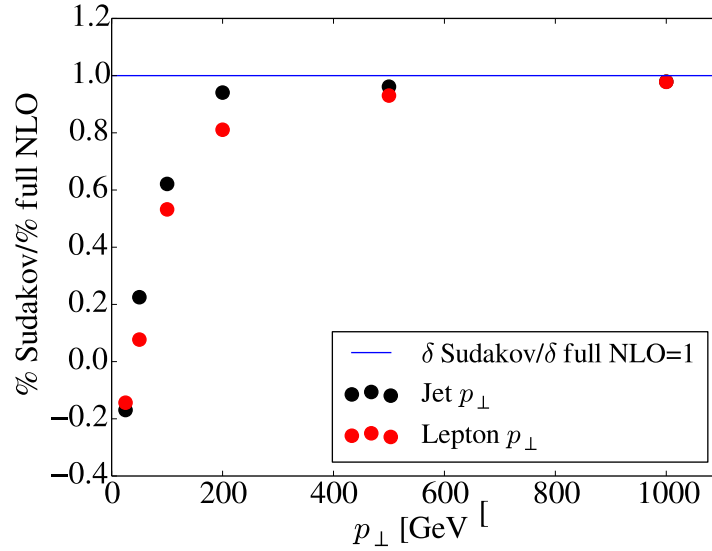
Figure 4.8:   Validation of EW Sudakov approximation implemented in SHERPA against exact NLO corrections from Ref. [131] for $pp \to \ell^+\nu j$ production at a 14 TeV LHC for increasing lepton $p_\perp$ and jet $p_\perp$. The Sudakov approximation converges to the NLO result in the high-$p_\perp$ limit.

Therefore, this process further tests the ability of the implementation to remove the correction from these regions.

Fig. 4.8 shows the validation for $\ell^+\nu j$ production at a 14 TeV LHC against the exact NLO EW calculation performed in Ref. [131]. The set-up for this process uses the same EW parameters as in the previous subsections, detailed in Subsec. 4.5.1 in Tabs. 4.1 and 4.2, with additional requirements on the additional jet. The jet is defined with the anti-k_T method, with $R = 0.4$. There must be at least one jet, which is well separated from the lepton, $\Delta R_{lj} > 0.4$, and satisfies $p_{\perp,j} > 25$ GeV and $|y_j| < 2.5$. The renormalisation and factorisation scales were set as

$$\mu_r = \mu_f = \sqrt{M_W^2 + p_{\perp,j}^2}. \tag{4.26}$$

Values of the total cross sections were presented in Ref. [131] for different values of the jet $p_\perp$ and lepton $p_\perp$. Fig. 4.8 shows the EW Sudakov implemenation in SHERPA approaches the exact NLO result for high-$p_\perp$ for both increasing lepton and jet $p_\perp$. The approximation converges slightly faster for increasing jet $p_\perp$ than lepton $p_\perp$.
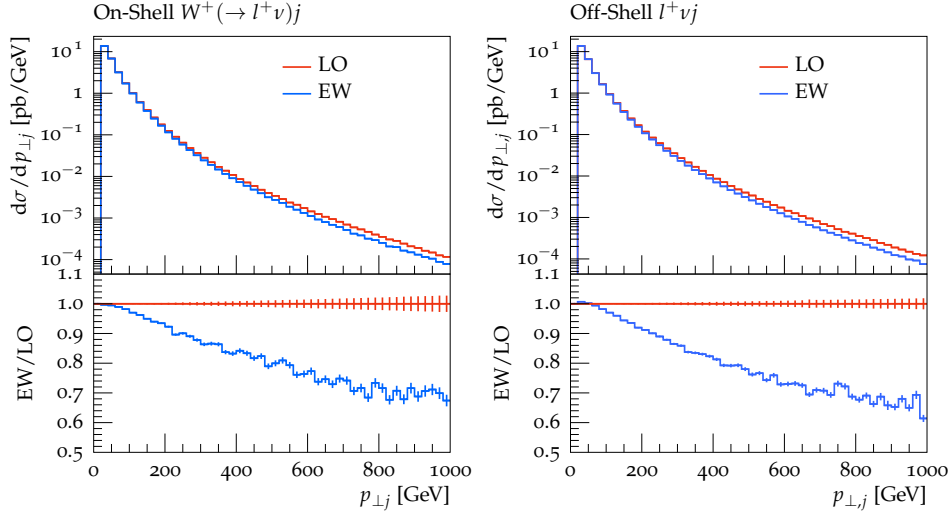
Figure 4.9: The effect of EW Sudakov logarithms on the $p_\perp$ distribution of the leading jet in $W^+(\to \ell^+\nu)j$, $\ell^+ = e^+, \mu^+$ inclusive events with a 25 GeV cut on the jet $p_\perp$ at a 14 TeV LHC for on-shell (left-hand-side) and off-shell (right-hand-side) production.

4.6 Results

This section presents some initial results obtained with the EW Sudakov implementation in SHERPA. It builds on the $pp \to \mu^+\nu + X$ and $pp \to \ell^+\nu j + X$ processes validated in Subsecs. 4.5.3 and 4.5.1, and presents results for $pp \to \ell^+\nu$+jets at a 14 TeV LHC. No hadronisation or underlying event affects were considered in these results.

4.6.1 Width effects for $pp \to W^+j + X$ production at a 14 TeV LHC

Firstly, the effect of the W^+ boson width is considered. For these results, the set-up used in Subsec. 4.5.3 was used, although the W boson width was set to 0 for the on-shell production of the W^+ boson. In contrast to the off-shell production case considered in Subsec. 4.5.3, the on-shell W^+j process involves flavour changes which necessitate momenta redistributions. However, it is still a simple $2 \to 2$ process which therefore does not frequently run into regions of phase-space for which the angle between relevant legs is sufficiently small as to move out of the appropriate regime for the Sudakov
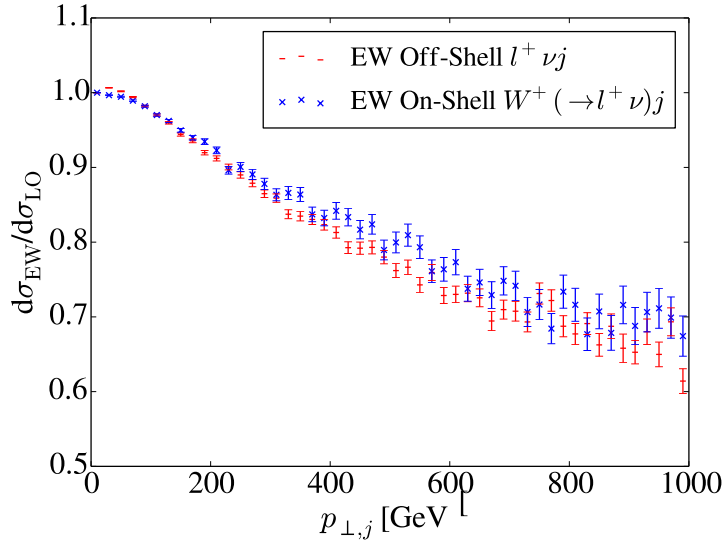
Figure 4.10: The effect of EW Sudakov logarithms on the $p_\perp$ distribution of the leading jet in $\ell^+\nu j$ inclusive events with a $25\,\text{GeV}$ cut on the jet $p_\perp$ at a $14\,\text{TeV}$ LHC. $\ell^+ = e^+, \mu^+$. The uncertainties shown are statistical.

approximation. Also, three of the external legs are required to be partons, indicating that one must be a gluonic leg. As gluons do not carry any EW charge, there are only three external legs sensitive to the EW Sudakov correction. The $W^+ \to \ell^+\nu$ decay is factorised from the production process, and spin correlations are not included.

Fig. 4.9 shows the full distribution for on-shell and off-shell W^+ boson production in leptonic decays to $\ell^+\nu$ for $\ell^+ = e^+, \mu^+$. The left-hand plot shows the effect on the distribution for W^+ bosons produced on-shell, and the right-hand plot shows the same distribution for off-shell production. The left-hand plot therefore shows the effect of the EW Sudakov corrections on the W^+ boson, whereas the right-hand plot shows the approximation on the decay products, but not the intermediate boson. The effect of considering the W^+ boson to be produced on-shell is small compared to the size of the EW Sudakov corrections in the limit of high jet-$p_\perp$.

Fig. 4.10 shows the direct comparison of the EW Sudakov corrections for the two distributions presented in Fig. 4.9. This shows similar behaviour for both cases; the correction becomes more negative with increasing jet-$p_\perp$. However, the on-shell W^+ production case tends to have a less negative correction than the off-shell production throughout the high-$p_\perp$ tail of the
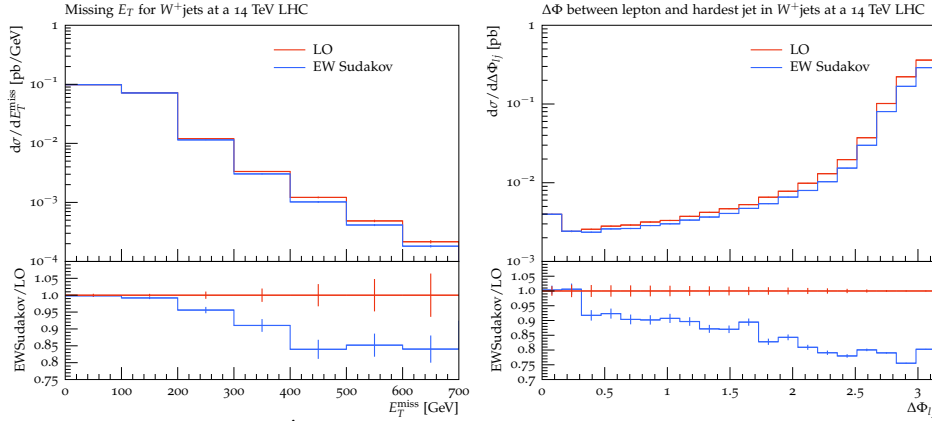
Figure 4.11:   The $E_\perp^{\text{miss}}$ (left-hand-side) and $\Delta\Phi$ between the lepton and hardest jet (right-hand-side) for $\ell^+\nu$+jets production at a 14 TeV LHC, at LO and including the SHERPA implementation of the EW Sudakov approximation. The uncertainties are statistical.

distribution. The Sudakov correction in Fig. 4.10 is negative over the full $p_\perp$ range. It is most significant in the highest $p_\perp$ region, where it reaches $\sim -30\,\%$. This demonstrates the increasing dominance of the leading soft-collinear logarithms over the single logarithms at increasing energy. This behaviour would therefore be more pronounced at even higher energies.

4.6.2 $pp \to \ell^+\nu$+**jets at a 14 TeV LHC**

Results are presented in this subsection are for the $pp \to \ell^+\nu$+jets process, with the 0,1 jet contributions from the ME, which include the EW Sudakov correction. On top of this, the parton shower radiates, without any higher-order correction. The off-shell production is considered, such that the decay of the W^+ boson is correctly treated with the EW Sudakov correction and including all spin correlations. The set-up is again consistent with Subsec. 4.5.1, with a merging scale of 30 GeV. The renormalisation and factorisation scales are set according to the CKKW prescription [133, 134].

The left-hand-side of Fig. 4.11 shows the $E_\perp^{\text{miss}}$ distribution at a 14 TeV LHC for $\ell^+\nu$+jet. The EW Sudakov correction increases with $E_\perp^{\text{miss}}$, to $\mathcal{O}(20\,\%)$ at 500 GeV. In the first bin of Fig. 4.11, the EW Sudakov correction is negligible. This implies that the total cross-section is not significantly affected by the EW Sudakov correction. Instead, the importance of the EW Sudakov

correction in Fig. 4.11 is in the the high-energy limit.

The right-hand-side of Fig. 4.11 shows the $\Delta\Phi$ distribution between the lepton and hardest jet in the event. This shows an increasingly negative correction from the EW Sudakov correction with increasing angular separation of the lepton and the jet, up to $\mathcal{O}(25\,\%)$. Fig. 4.11 demonstrates the behaviour of the EW Sudakov logarithms both with increasing energy (left-hand-side) and with angle (right-hand-side).

4.7 Conclusions

This chapter has detailed the implementation of Sudakov logarithms as an approximation to exact NLO EW processes in the high-energy limit. The theory behind the approximation has been outlined and the origin of the large logarithms explained. The implementation of these logarithms in SHERPA has been fully documented, the technical issues addressed, and the origins of theoretical uncertainty discussed.

This implementation has been validated against literature numbers for total cross sections for the following processes with increasingly hard final state cuts:

1. $pp \to \mu^+\nu$ at $14\,\mathrm{TeV}$ at the LHC with a cut on transverse mass.

2. $pp \to \mu^+\mu^-$ at $14\,\mathrm{TeV}$ at the LHC with a cut on invariant mass.

3. $pp \to \ell^+\nu j$ at $14\,\mathrm{TeV}$ at the LHC for a cut on both the jet $p_\perp$ and lepton $p_\perp$, separately.

The first and second processes considered comprised comparisons to independent calculations of the EW Sudakov correction, and to the exact NLO EW result. Good agreement was found for $pp \to \mu^+\nu$ with the independent EW Sudakov calculation, and the EW Sudakov implementations approached the exact result in the high energy limit. For the $pp \to \mu^+\mu^-$ process, the SHERPA EW Sudakov implementation converged to the exact NLO EW result faster than the independent calculation, as it included a phase-space cut on the regions where the EW Sudakov approximation is invalid. The final

comparison was with the exact NLO EW calculation alone. The NLO EW calculations for a $14\,\mathrm{TeV}$ LHC were considered, for various cuts on both the lepton $p_\perp$ and jet $p_\perp$. In both cases, the SHERPA implementation of the EW Sudakov logarithms converged to the exact NLO EW calcuation with increasing $p_\perp$.

Some initial results were then presented for W^+j and the $\ell^+\nu+$jets processes at a $14\,\mathrm{TeV}$ LHC. This demonstrated the difference in considering on-shell and off-shell effects for $\ell^+\nu j$ production. The results show that the difference between these two calculations is small, even in the high energy limit, although the off-shell production does have a slightly more negative correction than the on-shell production channel. Results were also presented for a merged $\ell^+\nu+$jets calculation, which showed the behaviour of the EW Sudakov approximation with increasing centre-of-mass energy, as well as its angular dependence. The size of the EW Sudakov correction grew both with increasing energy and increasing angular separation.

Part II

Physics at the LHC

Chapter 5

Tri-Lepton Production in the SM

This chapter presents results obtained to NLO QCD accuracy with the SHERPA + OPENLOOPS framework for tri-lepton final states in SM processes. In Higgs boson studies, the tri-lepton final state naturally allows the coupling between weak bosons and the Higgs boson to be studied. Furthermore, the tri-lepton final state is a rare final state in the SM, which greatly reduces the backgrounds to BSM processes, which is why multi-lepton final states are used frequently in such searches. In this case, the Higgs boson provides a significant contribution to the background.

In the light of all experimental determinations of the properties of the Higgs boson with SM expectations based on the BEH mechanism [3–8], it is clear that increasingly precise studies become necessary in order to look for subtle effects where new physics could manifest itself.

A prime candidate for such studies is the production of multiple gauge bosons: channels involving ZZ, $W^\pm W^\pm$ and $\gamma\gamma$ final states have been employed, among others, for the discovery of the Higgs boson, while processes with $W^\pm\gamma$, $W^\pm Z$, ZZ, and $Z\gamma$ final states are frequently used by the experiments to search for anomalous triple gauge boson couplings, see for instance Refs. [135–138]. Clearly, with higher energies, such searches can, and will, be extended to also include anomalous quartic gauge couplings. In addition, multi-boson channels, and in particular those that lead to final states

involving three leptons, are important backgrounds in searches for new particles; as an illustrative example consider neutralino-chargino pair production and their subsequent decay in supersymmetric extensions of the SM. This is discussed further in Sec. 5.2.

This chapter is divided into two sections:

- **Sec. 5.1**

  This section presents the work published in Ref. [139] on searches for the Higgs boson in tri-lepton final states.

- **Sec. 5.2**

  This section presents work from an ongoing study with K. Zapp and F. Krauss into rare SM processes that contribute to BSM backgrounds.

5.1 VH Associated Production in the Tri-Lepton Channel

Since the discovery of the Higgs boson at the LHC there has been considerable interest in the different available production modes. Both ATLAS and CMS have published papers on VH production at the LHC [140–142]. This section looks at the tri-lepton channel of these papers. These analyses naturally allow the coupling between the Higgs boson and the vector bosons to be studied.

5.1.1 Introduction

This section focuses on the production of a SM Higgs boson in the Higgsstrahlung process (associated VH production) and its subsequent decay into W- or τ-pairs. Apart from the signal, all relevant background channels will be studied as well. This includes multiple gauge boson final states such as $W^\pm Z$, $W^\pm W^+ W^-$, $ZW^\pm W^\pm$, ZZ, $W^\pm ZZ$ and ZZZ. The studies presented here follow closely the recent analyses by ATLAS and CMS [140–142].

In many of these processes, QCD corrections play a significant role, from highly phase-space dependent K-factors ranging between 1.5 and 2 to the fact that the emergence of additional jets can be used to shed light on the

actual production mechanism giving rise to triple gauge boson final states. In addition, quite often vetoing additional jets is a very good way to suppress unwanted backgrounds, a prime example being the large suppression of the $t(\to W^+ b)\bar{t}(\to W^- \bar{b})W$ background to $W^\pm W^+ W^-$ production or other signals, which allows this class of processes to be ignored here.

For the signal process, VH-associated production, parton-level results are available at NLO in the perturbative expansion of QCD [143] and NNLO results have been known for more than a decade [144, 145]. Resummed predictions were computed more recently [146]. The NLO QCD corrections to triple gauge boson production have first been calculated in [147, 148], the leptonic decay of the bosons has been discussed in [149, 150] and it has also been implemented in the VBFNLO code [151]. Predictions at NLO QCD for triple gauge boson production in association with one extra jet are presented.

For the calculation of the virtual corrections, OpenLoops [66] is employed. For the Born and real emission contributions, the ME generators Amegic++ [152] and Comix [64] are used. The mutual cancellation of infrared divergences in real and virtual contributions is achieved through the dipole formalism [77, 153] and its automated implementation in both Amegic++ [65] and Comix. The overall event generation is handled by Sherpa [19, 20]. For the first time, the NLO QCD calculations are combined consistently with parton showers, employing the S-MC@NLO variant [112, 113] of MC@NLO [109, 154] outlined in Subsec. 2.2.2. Parton showers are generated by Sherpa, based on Catani-Seymour dipole subtraction [77, 153] as suggested in Ref. [155] and implemented in Ref. [156]. In addition, a multijet merging with NLO QCD MEs including one additional jet is included, following the MEPS@NLO algorithm [134, 157] mentioned in Subsec. 2.2.3.

The Monte Carlo methods used to simulate jet production and evolution are discussed in Chap. 2. Subsec. 5.1.2 presents results obtained with the S-MC@NLO matching and MEPS@NLO merging methods. The discussion focuses on the treatment of signal and background with typical cuts as used by ATLAS and CMS [140–142]. This section closes with a summary and some outlook in Subsec. 5.1.3.

5.1.2 Results

Details of the Analyses

There are current efforts from both CMS and ATLAS to search for the tri-lepton ($\ell = e, \mu$) final states emerging from $W^{\pm}H$-associated production, where the Higgs boson decays either into $\tau^{\pm}$ or $W^{\pm}$ pairs [140–142][1]. These final states allow a direct probe of the coupling between the Higgs boson and the weak bosons. In the following, two analyses are presented: the first inspired by a recent search by the CMS collaboration [141], the second following searches from the ATLAS collaboration [140, 142]. The majority of the cuts that are applied in both are given in Tab. 5.1. Their crucial features in reducing unwanted backgrounds are a veto on Z bosons, which is realised differently in both analysis, and vetoes on jet activity to eliminate the large background from $t\bar{t}V$ production. Jets are reconstructed in both analyses using the anti-k_T algorithm [158, 159] with the parameters given in Tab. 5.1. In the ATLAS-inspired analysis, events are allowed to contain at most one jet, which must not be a b-tagged jet. The CMS-inspired analysis vetoes all events with a jet of $p_{\perp} > 40\,\text{GeV}$ and any containing b-tagged jets. Both analyses dress electrons with all surrounding photons within a cone of $\Delta R = 0.1$ while muons are left bare.

The ATLAS-inspired analysis requires exactly three isolated leptons of net charge ± 1. At least one of the leptons needs to have a transverse momentum of more than $25\,\text{GeV}$ for electrons and $21\,\text{GeV}$ for muons, the other two leptons $p_{\perp} > 10\,\text{GeV}$ each. They are labelled in the following way: the lepton with charge different from the others is called lepton 0, of the two others the one with smaller distance ΔR from lepton 0 is called lepton 1 and the remaining one is labelled as lepton 2. The leptons are considered isolated if the transverse energy of all visible particles in a cone of radius $\Delta R_{\text{iso}} = 0.2$ for leptons 0 and 1 and $\Delta R_{\text{iso}} = 0.4$ for lepton 2 around the lepton is less than 10% of the lepton $p_{\perp}$. After this, pre-selection events containing a same-flavour-opposite-sign (SFOS) lepton pair are classified as Z enriched, those that do not belong to the Z depleted sample. In this section only the

---

[1] Note that the ATLAS publication also includes similar searches in ZH-associated production which will not be considered here.

Cut	ATLAS	CMS
$p_{\perp,\text{min}}^{\ell}$	$10\,\text{GeV}$	$10\,\text{GeV}$
$|\eta_{\text{max}}^{e}|$	2.47	2.5
$|\eta_{\text{max}}^{\mu}|$	2.5	2.4
N_{leptons}	3	≥ 3
Z veto	no SFOS	$|m_Z - m_{\text{SFOS}}| > 25\,\text{GeV}$
$|\sum Q_\ell|$	+1	+1
Jet $p_{\perp,\text{min}}$	$25\,\text{GeV}$	$20\,\text{GeV}$
Jet $\text{d}R$	0.4	0.5
$E_{\perp,\text{min}}^{\text{miss}}$	–	$40\,\text{GeV}$

Table 5.1: Cuts for the ATLAS- and CMS-inspired analyses.

Z depleted subsample is considered. Contrary to the experimental analysis in Ref. [140], no requirement on the missing transverse energy is applied.

The CMS-inspired analysis, on the contrary, requires at least three isolated leptons of net charge ± 1. Of those, at least one is required to have $p_\perp > 20\,\text{GeV}$ while the others must only fulfil $p_\perp > 10\,\text{GeV}$. The lepton isolation in turn depends on lepton flavour rather than classification. Electrons are considered isolated if in a cone of radius $\Delta R_{\text{iso}} = 0.4$ the sum of the transverse energy of all visible particles does not exceed $15\,\%$ of the lepton $p_\perp$, while muons must satisfy this limit only in a cone of size $\Delta R_{\text{iso}} = 0.3$. In case a pair of SFOS leptons is present in the event, the event is discarded if its invariant mass is closer to the nominal Z boson mass than $25\,\text{GeV}$.

Both the ATLAS and CMS analyses include regions with more cuts than are described here, however the observables presented do not use these regions.

Monte Carlo Samples

Production of $pp \to 3\ell + E_\perp^{\text{miss}} + X$ is considered at the LHC for a centre-of-mass energy of $8\,\text{TeV}$. All processes with at least three leptons that involve an on-shell Higgs boson are considered as signal processes, and those which do not are considered background processes. Neutrinos do not necessarily need to be present since missing transverse energy can also be generated due to the limited detector acceptance in rapidity.

The signal is comprised primarily of $W^\pm H(\to W^+W^-)$, $W^\pm H(\to \tau^+\tau^-)$

and $ZH(\to W^+W^-)$, but includes also $ZH(\to \tau^+\tau^-)$, $W^{\pm}H(\to ZZ)$ and $ZH(\to ZZ)$ as subdominant contributions. All signal processes are calculated at MEPS@NLO accuracy, merging the respective processes accompanied by zero/one jets at NLO in QCD and by two jets at LO accuracy. The background processes considered are high-multiplicity bosonic final states: $W^{\pm}Z$, ZZ, $W^{\pm}W^+W^-$, W^+W^-Z, $W^{\pm}ZZ$ and ZZZ, which can evade the Z veto by the same method as $W^{\pm}Z$, and also include hadronic decays of the bosons. Higher multiplicity final states do not have a significant enough contribution to be considered. In addition, the production of an off-shell Higgs boson decaying to an on-shell V boson pair is also considered as part of the background. The cross-section for this process is very small as compared to the production of the on-shell Higgs boson, and it contributes mostly through its interference with the triple boson background. The $W^{\pm}Z$ boson background remains dominant over large portions of phase-space; this is due to lost leptons and, more importantly, due to decays into τ-leptons which enable the evasion of the Z veto. Of less importance is the $W^{\pm}W^+W^-$ process, nonetheless warranting high theoretical accuracy. Thus, both $W^{\pm}Z$ and $W^{\pm}W^+W^-$ are calculated at the same accuracy as the signal processes, while the remaining subdominant background processes, ZZ, W^+W^-Z, $W^{\pm}ZZ$ and ZZZ, are considered at MENLOPS accuracy, i.e. NLO QCD accuracy for the respective inclusive process and leading order accuracy when the gauge bosons are accompanied by one and two jets. Further, in order to prevent $tV_1V_2/\bar{t}V_1V_2$ contributions entering the $V_1V_2W^{\pm}j$ calculation, and $t\bar{t}V$ contributions entering the VW^+W^-jj calculation, only light quarks are considered in the ME final state.

The Higgs and W/Z gauge boson decays are treated in the narrow width approximation, including spin correlation effects throughout all decay chains. The kinematics are then corrected by redistributing the boson's propagator mass onto a Breit-Wigner distribution. In cases where $1 \to 2$ decays are not allowed kinematically their $1 \to 3$ substructure is resolved. This is relevant mainly for $H \to VV^*$ decays. Additionally, all decays receive higher-order QCD and QED corrections through intermediate parton showering or YFS-type soft-photon resummation (including full $\mathcal{O}(\alpha)$ corrections) [160], respectively. Throughout, all possible decays leading to the desired final state

are considered, including all invisible Z- and hadronic W-, Z- and τ-decay channels.

The distributions for the central values include hadronisation [161] and an underlying event simulation [162]. Scales are set according to the CKKW prescription [133, 134] and the uncertainties are evaluated as follows

- To determine the renormalisation scale, the event is clustered using the inverse of the parton shower, including electroweak splitting functions as introduced in Ref. [163], until a $2 \to 2$ core configuration is reached. The renormalisation scale μ_R is then defined through

$$\alpha_s^{k+n}(\mu_R) \;=\; \alpha_s^k(\mu_{\text{core}}) \prod_{i=1}^{n} \alpha_s(t_i) \,, \qquad (5.1)$$

  wherein k is the QCD order of the such determined core process at tree level, i.e. $k = 0$ for $q\bar{q}^{(\prime)} \to VV^{(\prime)}$ or $q\bar{q}^{(\prime)} \to VH$, $k = 1$ for $q\bar{q}^{(\prime)} \to Vg$ or $gq \to Vq^{(\prime)}$, and $k = 2$ for pure QCD core processes. n is the final state clustered jet multiplicity and the t_i their respective reconstructed emission scales. As core scale, $\mu_{\text{core}} = \sqrt{\hat{s}}$ is chosen for $k = 0$, $\mu_{\text{core}} = \frac{1}{2} m_\perp(V)$ for $k = 1$, and $\mu_{\text{core}} = \frac{1}{2} p_\perp$ for $k = 2$. For $n = k = 0$, $\mu_R = \mu_{\text{core}}$ is set. The factorisation scale is set to $\mu_F = \mu_{\text{core}}$ on the core configuration. The thus determined μ_R and μ_F are then varied by a factor of 2.

- The resummation scale μ_Q, also defined in Ref. [134], is set equal to the factorisation scale. It is varied by a factor of $\sqrt{2}$, cf. Ref. [164, 165].

- Q_{cut} is the merging scale. Three values are chosen for this scale, $15\,\text{GeV}$, $30\,\text{GeV}$ and $60\,\text{GeV}$.

The uncertainties in all figures are shown as two bands, one for the combined background and one for the combined signal, accumulated through their respective contributing processes only. They have been evaluated at the parton level. The full perturbative uncertainty for each process is obtained as the quadratic sum of the envelopes provided by the variation of the perturbative scales, μ_R, μ_F, and μ_Q, and the merging scale Q_{cut}. As non-perturbative uncertainties were found to be very small, these parton level uncertainties

Parameter	value
α	$1/128.802$
M_W	$80.419\,\mathrm{GeV}$
M_Z	$91.188\,\mathrm{GeV}$
M_H	$125\,\mathrm{GeV}$

Table 5.2: EW parameters used for the simulations of VH production and all relevant backgrounds.

are directly applicable to the hadron level results. The EW input parameters for this simulation are given in Tab. 5.2.

Results with MEPS@NLO

Results for selected observables defined on the event samples prepared with the analyses and scale uncertainties described above, are presented here. All observables considered below show a clear signal over background excess. They focus on the leptons from the hard process after the Z and jet veto. The Z veto is very important in these analyses, because without it the $W^{\pm}Z$ process is very dominant over both the signal and the background. Similarly, without the jet veto, top associated vector boson production would bury the Higgs processes.

The first observable considered is the tri-lepton invariant mass of events in the CMS-inspired analysis in Fig. 5.1. After the veto on the Z boson and final state b-tagged jets, the invariant mass distribution of the 3 leptons can be used to distinguish the signal from the background as a visible $30\,\%$ excess is seen in the peak region, far surmounting the background uncertainties displayed in the lower panel. Very similar findings are made when looking at events in the ATLAS-inspired analysis. Although the main signal process $W^{\pm}H(W^{+}W^{-})$ forms the majority of the excess, the contribution from $W^{\pm}H(\tau^{+}\tau^{-})$ is non-negligible, albeit of a slightly different shape. Regarding the background processes, the tri-boson processes have a significantly harder $m_{3\ell}$ spectrum, raising their relative contribution in the high-mass region, as can be seen in the logarithmically plotted inlay.

A somewhat complementary observable is the missing energy distribution, exhibited in Fig. 5.2, again effected on the event selection of the CMS-inspired
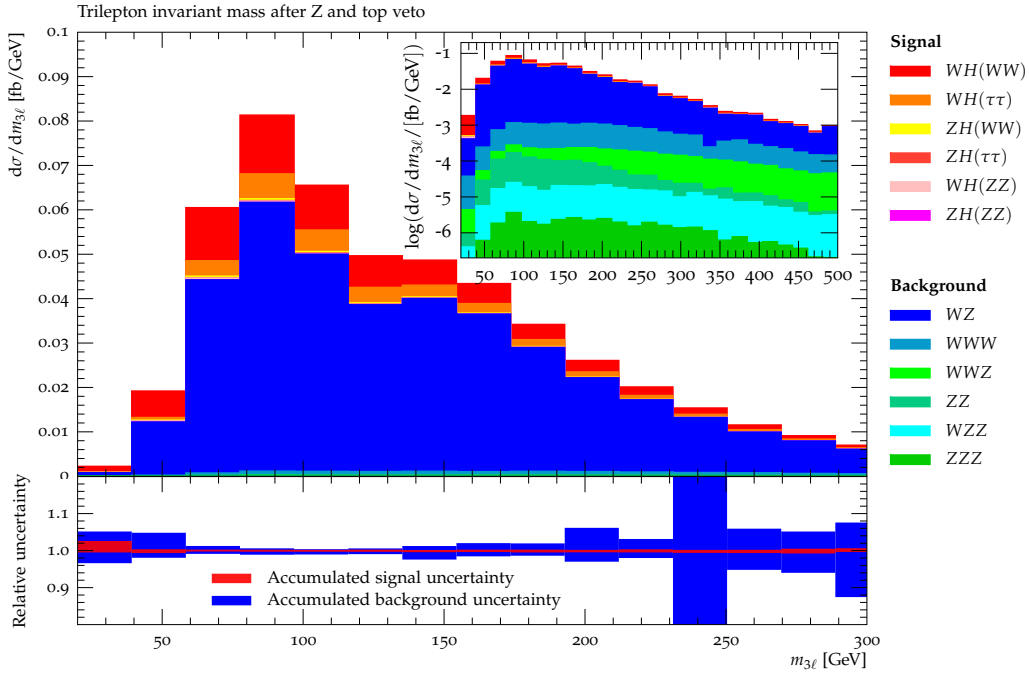
Figure 5.1: The tri-lepton invariant mass after CMS cuts. All contributing processes, grouped as whether considered signal or background and are added incoherently, ordered by relative contribution. The inset displays the same information on a logarithmic scale to better quantify the contributions of the rarer processes. Below the main plot the accumulated relative uncertainties originating from the respective signal and background processes to the total expected cross-section are detailed.

analysis. The findings indeed display a similar behaviour to the tri-lepton invariant mass distribution of Fig. 5.1, namely that the signal is clearly visible above the background for $E_\perp^{\rm miss} \lesssim 100\,{\rm GeV}$. Again, the dominant and subdominant signal processes, $W^\pm H(W^+W^-)$ and $W^\pm H(\tau^+\tau)^-$, exhibit somewhat different shapes, with $W^\pm H(\tau^+\tau^-)$ possessing less missing transverse momentum. In both observables, the $W^\pm Z$ background is the most dominant background. However, here the di-boson and tri-boson background have a very similar behaviour at large $E_\perp^{\rm miss}$.

The relatively small excess in the $E_\perp^{\rm miss}$ spectrum in the CMS-inspired event selection is enhanced in the ATLAS-inspired event selection with its stronger Z veto, implemented through a complete rejection on SFOS lepton pairs. Here, the $E_\perp^{\rm miss}$ distribution shows an excess of the signal over the background of up to 50%. This is displayed in Fig. 5.3. In contrast to the case of a Z
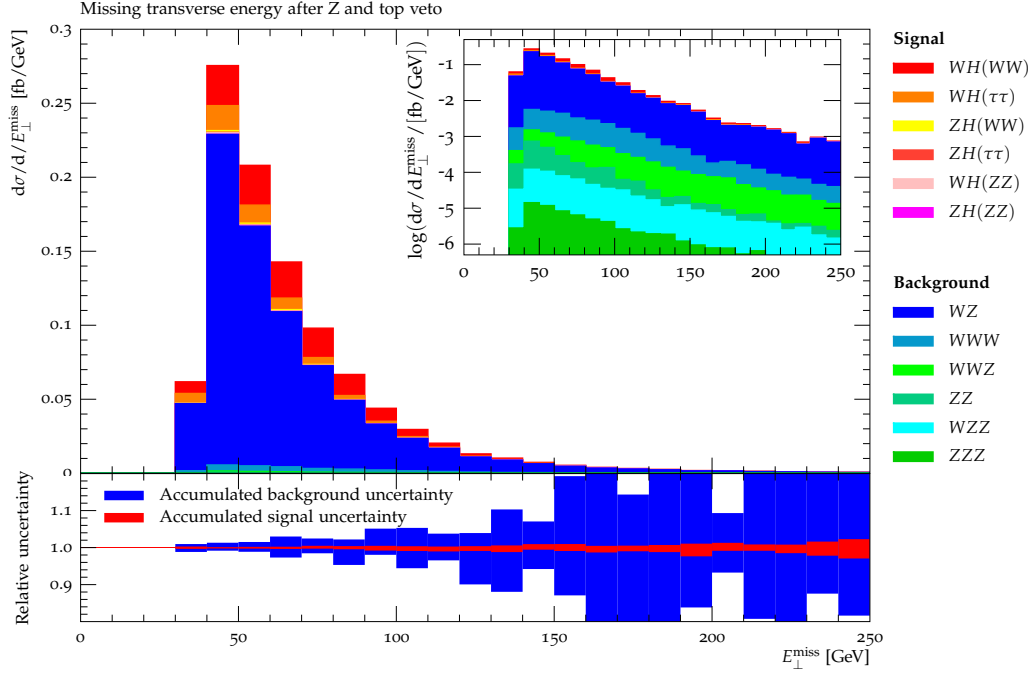
Figure 5.2: The missing transverse energy spectrum after CMS cuts. For details, see Fig. 5.1.
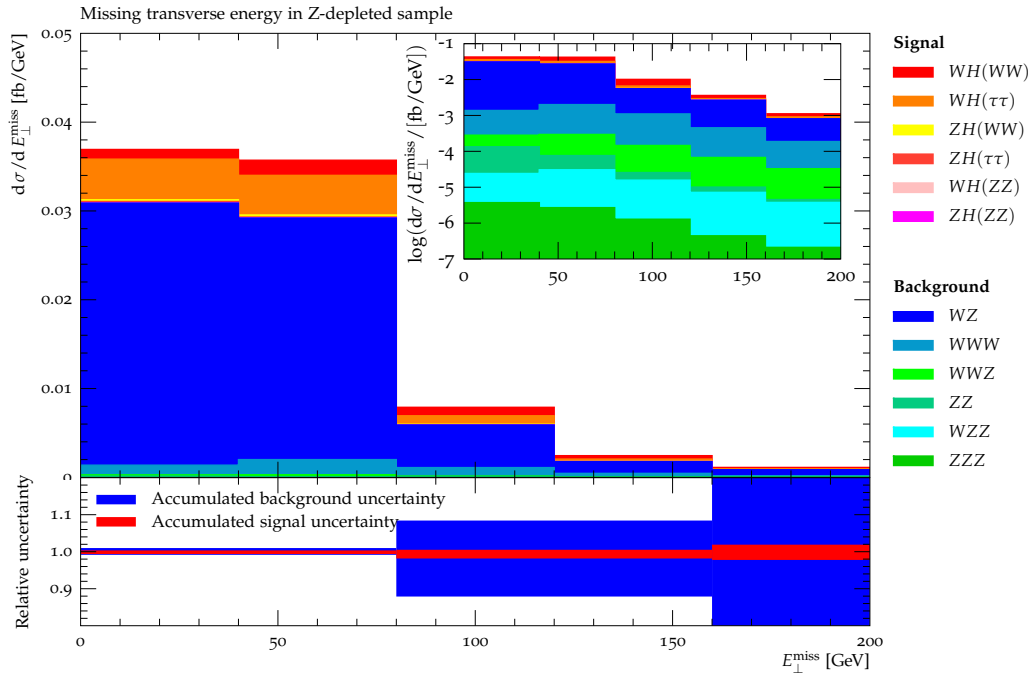
Figure 5.3: The $E_\perp^{\text{miss}}$ spectrum after ATLAS cuts. For details, see Fig. 5.1.
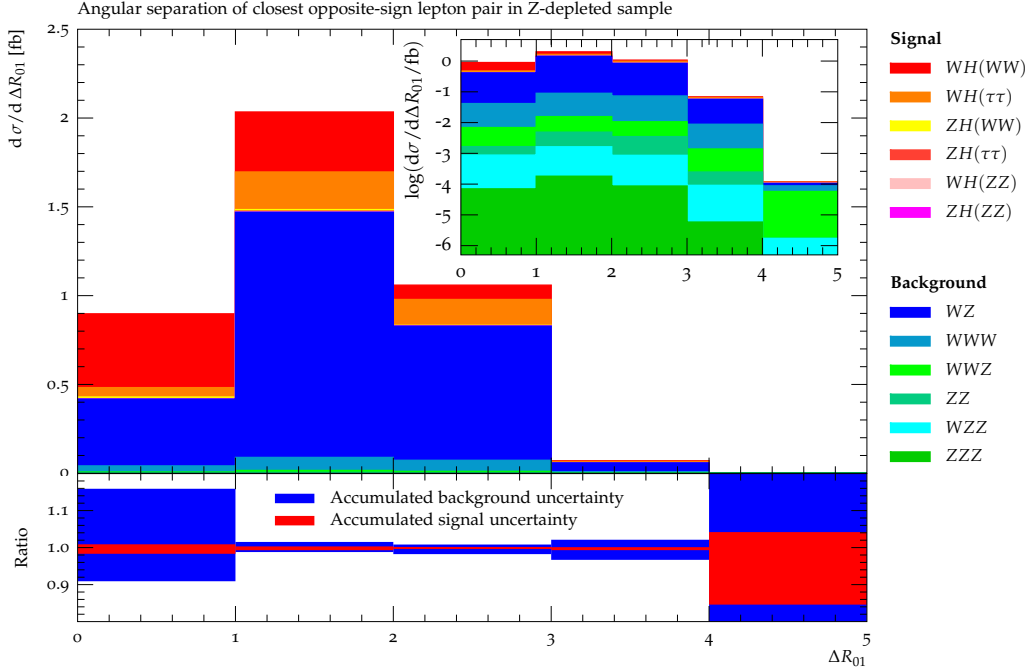
Figure 5.4: The angular separation of the closest pair of oppositely charged leptons in the case that no SFOS pair of leptons is found in the event after ATLAS cuts. For details, see Fig. 5.1.

veto through a mass window as in CMS, where the distribution especially for $W^\pm Z$ falls off smoothly, here the Z veto introduces a visible kink, while the signal remains unaffected. This, of course, could be further used to reduce the $W^\pm Z$ background by utilising this different impact on the respective shapes.

The angular separations between pairs of leptons are interesting observables for this process. Fig. 5.4 shows the distance ΔR between the closer of the two pairs of oppositely signed leptons, following the ATLAS-inspired event selection. These leptons do not have the same flavour, as this observable isolates the leptons that are most likely to be products of the Higgs boson decay to W^+W^- or τ pairs. This effect, in particular on the W^+W^- channel, stems from the spin correlations in the decay of the Higgs boson, as already discussed in Ref. [142]. As a result, this observable also has good discriminating power between signal and background, providing a clear excess in the region $\Delta R < 3$. It also, better than the other observables considered, separates the two main signal processes. While $W^\pm H(W^+W^-)$ constitutes approximately

80 % of the Higgs signal below $\Delta R = 1$, $W^{\pm}H(\tau^{+}\tau^{-})$ contributes roughly 60 % in the region $2 < \Delta R < 3$. There, however, the signal excess over the background has fallen from a factor of two to approximately 35 % of the background expectation.

The different uncertainties have been investigated individually for all processes to check for their dominant source. In nearly all bins of all observables considered in this section, the uncertainties are driven by the renormalisation and factorisation scale variation with a typical effect on the few-percent level up to about 10 % for the tri-boson processes. In regions dominated by jet activity, of course, the MENLOPS samples, being at leading order accuracy only, exhibit a stronger dependence than those processes simulated with MEPS@NLO. In addition, it is worth stressing that effects due to hadronisation and the underlying event are practically irrelevant for the uncertainties in the simulation of the processes for the observables considered here. Their main effect is on the isolation efficiency of the leptons. Although the non-perturbative corrections have a clear impact on the shape of tri-lepton invariant mass of Fig. 5.1, as the isolation is $p_{\perp}$-dependent, their uncertainties are barely noticeable. On the contrary, the missing transverse energies of Figs. 5.2 and 5.3 and the angular separation of Fig. 5.4 receive merely a change of the overall rate from effecting non-perturbative corrections. Again, their uncertainties are negligible.

5.1.3 Conclusions

In this section NLO QCD accurate predictions for multiple weak boson production at the LHC were presented, and their application to Higgs boson searches based in tri-lepton final states has been highlighted. The $W^{\pm}H$ and ZH Higgsstrahlung signals as well as the main backgrounds, $W^{\pm}Z$ and $W^{\pm}W^{+}W^{-}$ production, have been simulated at NLO in QCD including up to one extra jet in the MEPS@NLO multi-jet merging framework. The simulation of the $W^{\pm}W^{+}W^{-}$ background represents a non-trivial application of multi-jet merging at NLO QCD and plays an important role for all Higgs physics and new physics searches based on tri-lepton final states and jet vetoes. Also various other di-boson and tri-boson background processes have

been computed at NLO QCD, including matching to the parton shower and an improved description of extra jet radiation, based on the MENLOPS technique. It is confirmed, at NLO QCD, that the relevant backgrounds to $W^{\pm}H$ and ZH production are given by di-boson and tri-boson production processes, if jet vetoes can be applied. The residual perturbative uncertainties are shown to be, in large fractions of the relevant phase-space, of the order of 10% or even below. This will offer excellent opportunities for Higgs boson precision studies at the forthcoming LHC runs.

5.2 Rare SM Processes as BSM Backgrounds

This section studies a similar class of processes to Sec. 5.1, with a focus on their contribution to backgrounds for BSM studies. A notable difference is the inclusion of $t\bar{t}V$ processes in this section, since no jet veto is applied to remove them. Observables used by the ATLAS and CMS publications in tri-lepton BSM searches are presented, which focus on leptonic observables. These are naturally very stable against hadronisation and underlying event effects, neither of which are considered in this section.

5.2.1 Introduction

In addition to providing an interesting channel for Higgs studies, tri-lepton processes are very interesting as backgrounds to BSM physics, due to the rarity of high-multiplicity leptonic final state in the SM. This produces small backgrounds to BSM models capable of producing these high-multiplicity final states, the most prominent example of which being SUSY. See Ref. [166] for a complete set of Feynman rules in the MSSM, which is the minimal supersymmetric extension to the SM.

The existence of SUSY would introduce a partner to all observed particles, which would differ from its SM counterpart by half integer spin. These SUSY particles would need to acquire much larger masses than the SM particles by a process of symmetry breaking. The lightest superpartner (LSP) would be stable as a consequence of R-parity; which is a Z_2 symmetry, $R = \pm 1$, for which SM particles have $R = 1$ and supersymmetric particles have $R = -1$.

The LSP cannot be directly detected in an experiment, it would instead manifest itself as missing energy. Any SUSY particle created would then decay into familiar SM particles and missing energy. The searches for these particles are therefore confined to those SM signatures that introduce the least background. As such, the tri-lepton final state is ideal.

These tri-lepton final states would be a typical signature of the EW production of charginos and neutralinos. Charginos would be the superpartners to $W^{\pm}$ bosons, and the neutralinos would be a linear superposition of the superpartners to the neutral SM EW force carriers as well as Higgsinos. Charginos would produce a tri-lepton signature through decays via sneutrinos, sleptons or $W^{\pm}$ bosons, and neutralinos would produce similar final states through slepton and Z boson decays. As well as the tri-lepton SUSY searches at the LHC [69–74], similar studies have been completed at the TeVatron [167, 168] and at LEP [169–172].

This section uses an ATLAS-inspired analysis from Ref. [73] and a CMS-inspired analysis from Ref. [74].

From the ATLAS-inspired analysis, general event observables are considered, the scalar sum of visible particles, H_T and $E_{\perp}^{\mathrm{miss}}$ of the event. As well as this, angular distributions of the hardest leptons in the event are presented. These distributions are sensitive to spin correlation effects, and these effects will be different in SUSY processes than in the SM. This makes such observables good discriminators of SUSY processes.

The CMS-inspired analysis looks at the $E_{\perp}^{\mathrm{miss}}$ and H_T observables shown in Ref. [74]. This is binned by the invariant mass of the leptons identified as the most likely Z boson candidate, and the transverse mass of the remaining lepton and the missing energy. These distributions provide an insight into how the behaviour of the different backgrounds to the $E_{\perp}^{\mathrm{miss}}$ and H_T observables contribute with different invariant mass and transverse mass cuts.

5.2.2   Set-Up

This study is performed at S-MC@NLO level accuracy with SHERPA [19, 20] and OPENLOOPS [66] as the one-loop provider for the virtual MEs. As the

analyses employed in this section do not involve any jet vetoes, the increased accuracy of a MEPS@NLO calculation is not necessary for an accurate theoretical prediction. $W^\pm$, Z and Higgs bosons were produced on-shell, as were the top quarks. The decays of these particles were treated in a factorised way, with all spin correlations preserved. The kinematics of the production are corrected, with the kinematic distribution fitted on a Breit-Wigner curve as is explained more fully in Subsec. 5.1.2.

The effects of the weak boson width on typical observables can be seen in Fig. 5.5, where the distributions of the tri-lepton invariant mass and the missing energy distribution from the ATLAS analysis are shown for $t\bar{t}W^\pm$ production both for on-shell $W^\pm$ boson production, with the leptonic decay channel selected by the decay module during event generation, and direct production of $t\bar{t}\ell\nu$, where ℓ is a light lepton, either a muon or an electron. Decays to τ leptons are not considered for this check. Calculating the full final state naturally provides the decay to NLO QCD accuracy, whereas in the narrow-width approach these decays are factorised and calculated to LO accuracy only. Fig. 5.5 shows that the observables are not significantly impacted by the different treatments of the W boson decay.

While Fig. 5.5 shows general event observables, Fig. 5.6 shows the same comparison for angular distributions. The curves are the same to within the statistical uncertainty for both the ΔR distributions between the two hardest leptons in the event and between the two leptons of the same sign in the event. Therefore, these plots justify the use of MEs with on-shell W bosons for this study.

Similar plots are made for $t\bar{t}Z$ in Fig. 5.7. Here the invariant tri-lepton mass and ΔR between the two hardest leptons are presented, again normalised to unit area. For $t\bar{t}\ell^+\ell^-$ production the Z/γ^* interference is included, which is not present in $t\bar{t}Z$ production. This introduces a shift towards lower mass distributions, as can be seen in the left-hand plot of Fig. 5.7. However, in the angular distributions such as the right-hand plot of Fig. 5.7, these effects are not present, and the two simulations are equivalent to within the statistical uncertainties. This simulation of $t\bar{t}\ell^+\ell^-$ includes a cut on the invariant mass of the lepton pair, $M_{\ell^+\ell^-} > 5\,\text{GeV}$. In this analysis the narrow-width approximation is used for the $t\bar{t}Z$ process, as the effects of the inclusion of the
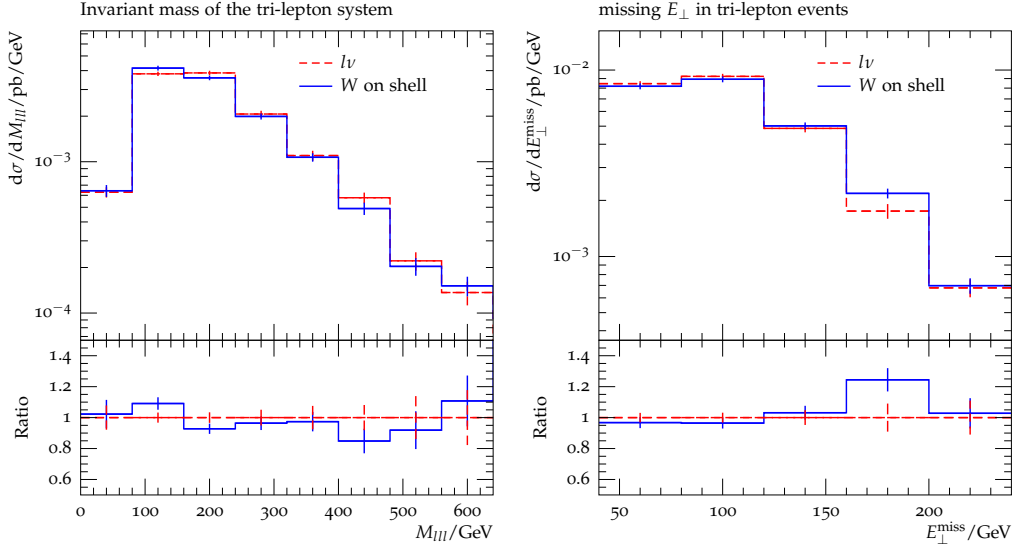
Figure 5.5: Left-hand-side shows the invariant mass distribution for the tri-lepton final state from the ATLAS analysis, and the right-hand-side shows the $E_\perp^{miss}$ distribution from the same analysis. Width effects are included in the red dashed curve and on-shell $W^\pm$ boson production is considered in the blue solid curve. Both plots are normalised to unit area, and the uncertainties are statistical.

Particle	Mass/GeV
M_W	80.414
M_Z	90.18
M_t	175
M_H	126

Table 5.3: Masses, M_X, of EW particles, X, used for this study.

full final state are too small to be significant in the observables considered.

Since the final state of all processes considered in this study are massive, no phase-space cuts were placed on the final state before passing the event through the experimentally-inspired analyses. The analysis was conducted at the parton level. This does not significantly impact the distributions because the observables considered, such as leptonic observables as well as H_T and $E_\perp^{miss}$, are stable with respect to hadronisation. The scales for these processes are set according to the CKKW procedure as described in Ref. [117]. The masses used in this study for the EW particles can be found in Tab. 5.3.
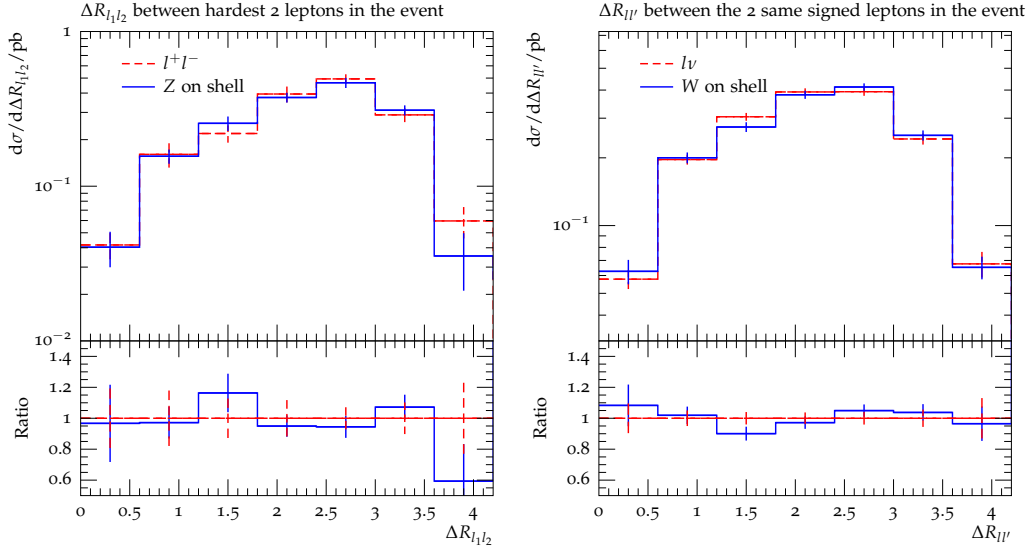
Figure 5.6: Left-hand-side shows the ΔR between the 2 hardest leptons for the tri-lepton final state from the ATLAS analysis, and the right-hand-side shows the ΔR between the 2 leptons of the same sign from the same analysis. Width effects are included in the red dashed curve and on-shell $W^{\pm}$ boson production is considered in the blue solid curve. Both plots are normalised to unit area, and the uncertainties are statistical.
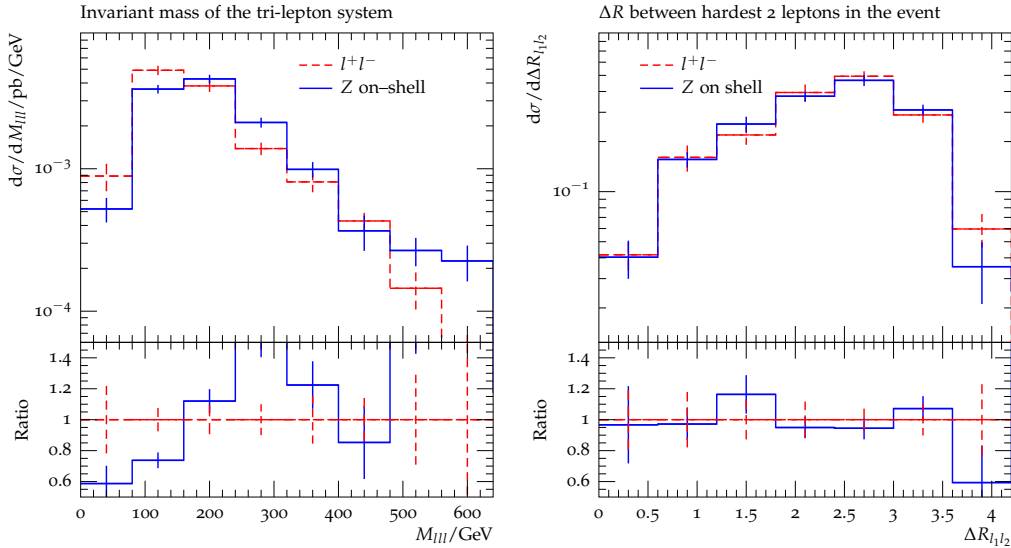
Figure 5.7: These plots show $t\bar{t}Z$ tri-lepton events for the calculation in the narrow width approximation for the Z boson and for the NLO QCD calculation of $t\bar{t}\ell^{+}\ell^{-}$. Left-hand-side shows the invariant tri-lepton mass and right-hand-side shows the ΔR distribution between the hardest 2 leptons in the event. These plots are normalised to unit area.

Parameter	cut
$E_\perp^{\text{miss}}$	$> 50\,\text{GeV}$
jet R	0.4
jet $p_\perp$	$> 20\,\text{GeV}$
jet $|\eta|$	< 2.5
no. leptons	3
SFOS	veto

Table 5.4: List of cuts in ATLAS tri-lepton SUSY search for the second validation region. Jet R is the radius used in the jet reconstruction.

5.2.3   Analyses

Two experimental analyses were translated into Rivet routines for this study. One from the ATLAS paper on chargino and neutralino searches in the tri-lepton channel from Ref. [73]. This ATLAS search was conducted at $\sqrt{s} = 8\,\text{TeV}$ and excluded chargino masses up to $580\,\text{GeV}$ with light sleptons in the range 150-300 GeV. This note includes several different signal and validation regions. In two of the three validation regions no veto on Z boson production is made. Therefore, in these regions the $W^\pm Z$ region is by far the most dominant process of all the irreducible backgrounds. In this section the focus is on rare SM processes, which are most relevant in the validation region with a veto on Z boson production. This is the VR2 region in Ref. [73], where a veto is applied to all SFOS lepton pairs.

On top of the cuts in Tab. 5.4, there is a requirement on the leptons to fulfil the experimental triggering requirement. This trigger condition depends on the flavour combination of the two hardest leptons in the event. In the case that both the leading and the subleading leptons in $p_\perp$ are muons, they are required to either both have $p_\perp > 14\,\text{GeV}$ or the leading muon to have $p_\perp > 18\,\text{GeV}$ and the subleading to have $p_\perp > 8\,\text{GeV}$. If both leptons are instead electrons, the condition is that either both electrons to have $p_\perp > 14\,\text{GeV}$ or for the leading electron to have $p_\perp > 25\,\text{GeV}$ and the subleading to have $p_\perp > 10\,\text{GeV}$. The final possibility is for mixed flavours, an electron and a muon as the hardest two leptons in the event. Here it is required that either the electron has $p_\perp > 14\,\text{GeV}$ and the muon has $p_\perp > 8\,\text{GeV}$ or the electron has $p_\perp > 10\,\text{GeV}$ and the muon has $p_\perp > 18\,\text{GeV}$. Jet reconstruction makes use of FASTJET [159] and the anti-k_T algorithm [158].

Parameter	cut
$E_\perp^{\text{miss}}$	$> 50\,\text{GeV}$
no. leptons	3
jet R	0.6
jet $p_\perp$	$> 20\,\text{GeV}$
jet $|\eta|$	< 5

Table 5.5: List of cuts for CMS-inspired SUSY search. Jet R is the radius used in the jet algorithm.

Leptons are required to be isolated from both jets and other leptons. If a jet is reconstructed to be within $\Delta R_{\ell j} < 0.2$ of an electron, where $\Delta R = \sqrt{\Delta\Phi^2 + \Delta\eta^2}$, it is discarded. This procedure provides a subset of the jets which are well separated from the electrons in the event, which are labelled as 'isolated jets'. Then, if any pair of leptons are within $\Delta R_{\ell\ell} < 0.1$ of each other, both leptons are discarded. An exception is made to this rule in the case that the leptons are both electrons. In this case, only the softer of the pair is discarded. The leptons are also required to be separated by $\Delta R_{j\ell} > 0.4$ from any of the isolated jets.

The CMS analysis for the tri-lepton SUSY search in Ref. [74] involves searches for leptonic final states. This study makes use of its tri-lepton analysis. This CMS analysis is also at $8\,\text{TeV}$ and bins results by the invariant mass of a lepton pair and the transverse mass of the remaining lepton and the missing energy. The cuts implemented for this analysis are given in Tab. 5.5.

The triggering requirement for the leptons in the CMS-inspired analysis is that the leading lepton in $p_\perp$ has $p_\perp > 10\,\text{GeV}$. Further, the CMS-inspired analysis includes isolation criteria for jets and leptons similar to the ATLAS-inspired analysis: a jet is discarded if it is reconstructed within $\Delta R_{\ell j} < 0.1$ of an electron; both leptons are discarded if they are within $\Delta R_{\ell\ell} < 0.1$ of each other, unless both leptons are electrons, in which case the softer of the two electrons is discarded.

Tab. 5.6 shows the different bins employed in this analysis. First, the events are separated into two regions, one with a SFOS pair, and one with no such pair. This other region has same flavour leptons with the same sign, and is therefore labelled the SSSF region. The invariant mass is taken from the pair of oppositely signed leptons with reconstructed invariant mass closest to

Binned Observables	$M_{\ell\ell}$		M_T
	SFOS	SSSF	
low/GeV	< 75	< 100	< 120
middle/GeV	$75 > M_{\ell\ell} < 105$	-	$120 < M_T < 160$
high/GeV	> 105	> 100	> 160

Table 5.6: Bins used in CMS analysis for invariant mass, $M_{\ell\ell}$, and transverse mass, M_T. For $M_{\ell\ell}$, the bins vary depending on whether a SFOS lepton pair is found. If not, the same-sign same-flavour (SSSF) bins apply.
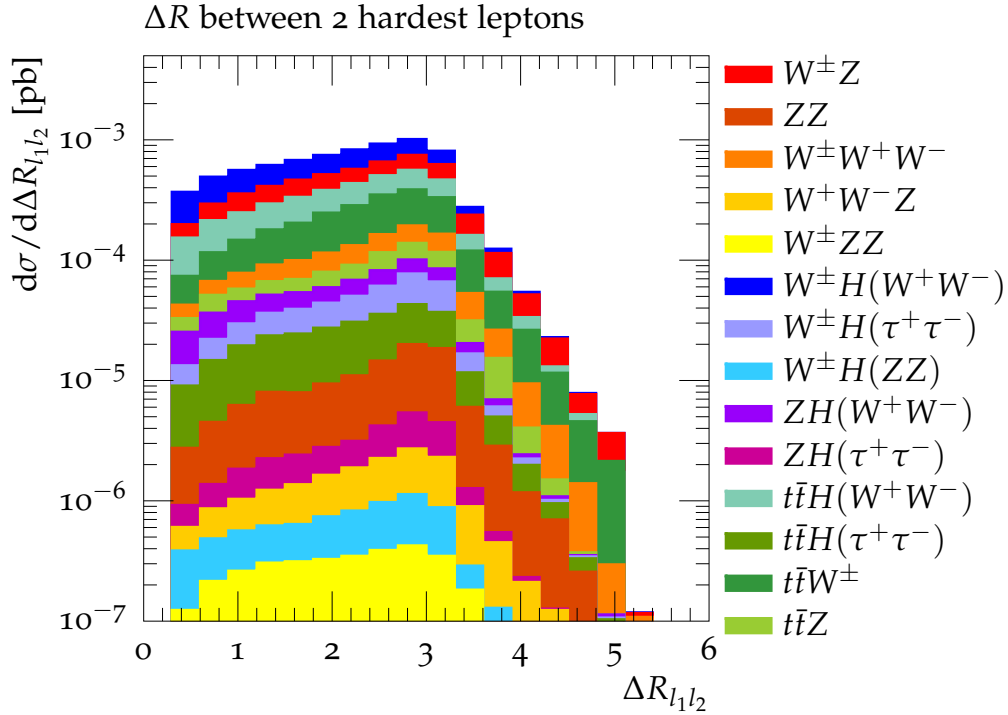
Figure 5.8: Distribution for ΔR between the hardest 2 leptons for the ATLAS-inspired analysis.

that of a typical Z boson decay to leptons via τ pairs. This is taken to be $50\,\text{GeV}$, as in Ref. [74].

5.2.4   Results

The results of the study are presented in this subsection, for both the ATLAS-inspired and the CMS-inspired analyses.
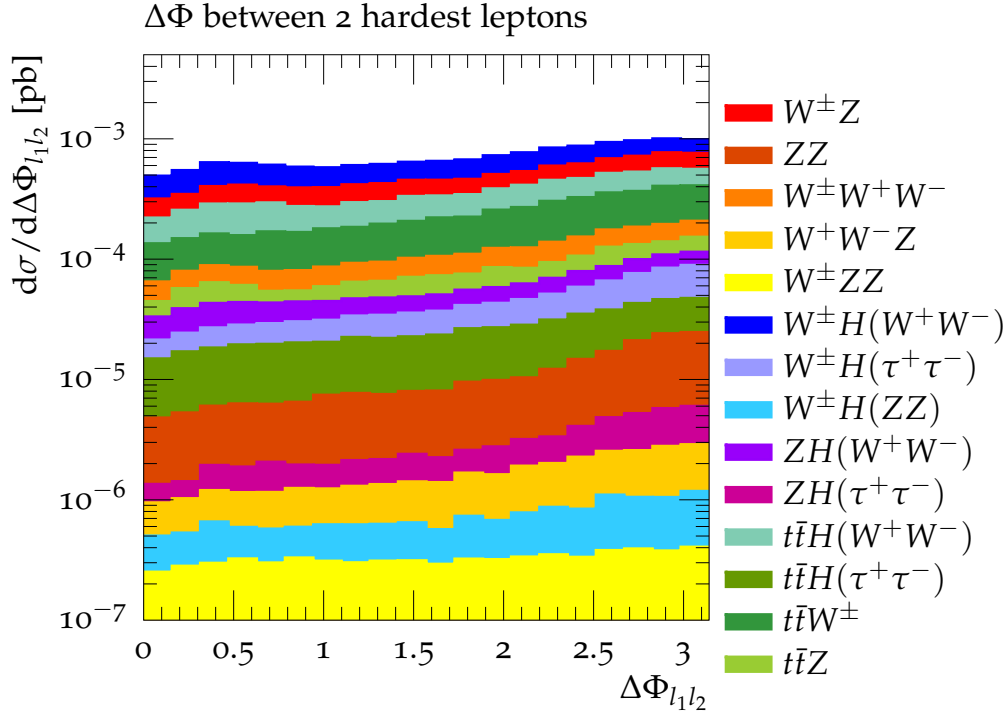
Figure 5.9: Distribution for $\Delta\Phi$ between the 2 hardest leptons for the ATLAS-inspired analysis.

ATLAS-Inspired Analysis

Fig. 5.8 shows the distribution for the ΔR between the 2 hardest leptons from the ATLAS-inspired analysis. The dominant contribution from the processes considered here is the di-boson $W^{\pm}Z$ production. $t\bar{t}W^{\pm}$ is the leading subdominant channel. The processes with Z boson production tend to fall off more quickly in the high $\Delta R_{\ell_1\ell_2}$ region, because the hardest leptons in this process are likely to both come from a single Z boson, which limits the distance between these decay products.

The $\Delta\Phi$ distribution between the two hardest leptons in the ATLAS-inspired analysis is shown in Fig. 5.9. $W^{\pm}Z$ di-boson production is similarly the most dominant process, with $t\bar{t}W^{\pm}$ as the leading subdominant process. The distribution for the total background shows an increasing trend towards $\Delta\Phi_{\ell_1\ell_2} = \pi$. This trend exists in all the background processes, but is weaker in the most dominant processes such that the sum of the backgrounds only sees an increase of a factor of ~ 2 between the first and last bins.

The two remaining observables shown from the ATLAS-inspired analysis are

Scalar sum of $p_\perp$ of visible particles
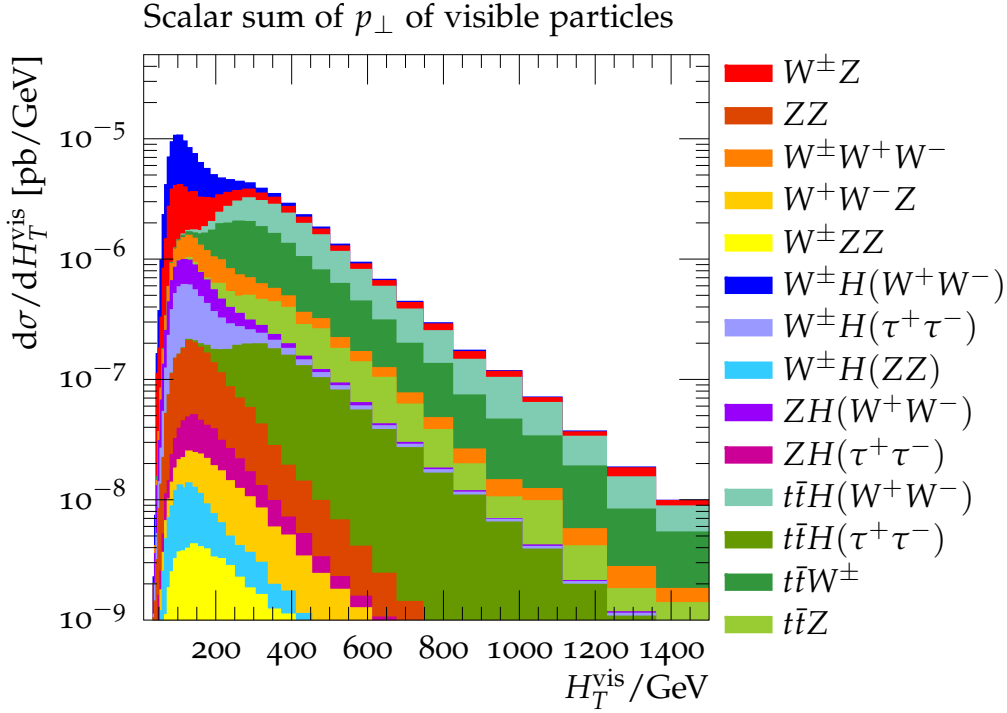
Figure 5.10: H_T from the ATLAS-inspired analysis for SM processes yielding a tri-lepton final state.
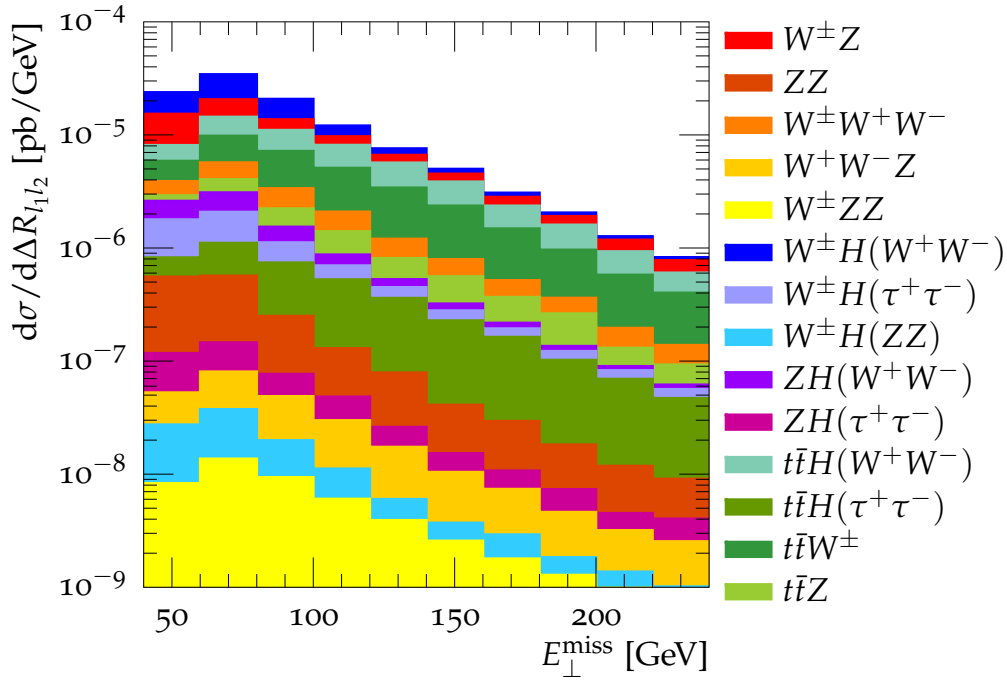
Figure 5.11: $E_\perp^{\text{miss}}$ from the ATLAS-inspired analysis for tri-lepton final states from SM processes.

the global event observables of the H_T of all objects in the event in Fig. 5.10, including leptonic activity and missing energy, and the $E_\perp^{\mathrm{miss}}$ of the event in Fig. 5.11.

Fig. 5.10 confirms the structure seen in Figs. 5.8 and 5.9, in that $W^\pm Z$ is the dominant process with $t\bar{t}W^\pm$ as the leading subdominant channel. It is clear from Fig. 5.10 that the $t\bar{t}W^\pm$ process becomes more dominant in the high-H_T region. This behaviour results from the increased mass of the final state of $t\bar{t}W^\pm$, which forces it into higher H_T regions than multi-boson production. This is clear from the shape differences observed in Fig. 5.10 between top-associated weak boson production and di-boson production. The top-associated production channels peak at $\sim 380\,\mathrm{GeV}$, whereas the multi-boson contributions peak earlier in the distributions at $\sim 200\,\mathrm{GeV}$. Therefore, it is important for this observable to have control over accurate calculations of both the $W^\pm Z$ process and the $t\bar{t}Z$ process which can dominate the shape in the high H_T tail.

Besides these most dominant contributions, Fig. 5.10 demonstrates the importance of Higgs boson production in association with a $W^\pm$ boson. The $H \to WW^*$ and $H \to \tau^+\tau^-$ decay modes, combined, contribute roughly $\frac{1}{3}$ of the total cross-section at the $W^\pm Z$ peak. The ZZ production contributions is also significant, of the order of one percent of the total cross-section. $t\bar{t}Z$ follows a similar pattern to $t\bar{t}W^\pm$, so while being negligible in the peak region, it can impact the shape of the tail. The smallest contribution shown here is that of $ZH(\to ZZ)$, which only contributes at the sub-percent level throughout the distribution.

The $E_\perp^{\mathrm{miss}}$ distribution in Fig. 5.11 shows a behaviour similar to that in Fig. 5.10. The dominant process at small values of $E_\perp^{\mathrm{miss}}$ is $W^\pm Z$ production, and the $t\bar{t}W^\pm$ process begins to dominate the shape effects in the high $E_\perp^{\mathrm{miss}}$ tail. However, Fig. 5.11, in contrast to Fig. 5.10, does not contain such a clear shape difference between $W^\pm Z$ and $t\bar{t}W^\pm$ production. Both of these processes peak at low values of $E_\perp^{\mathrm{miss}}$. The fall-off in the tail of the distributions is faster in the case of $W^\pm Z$ than it is in $t\bar{t}W^\pm$, but the effect is not as strong as it was in Fig. 5.10. The distributions are softer for those processes that require the $E_\perp^{\mathrm{miss}}$ to come from neutrinos from $\tau^\pm$ decays, which are on average much softer than those neutrinos originating from $W^\pm$ or Z boson

Figure 5.12: Histograms of missing energy of SFOS leptons closest to Z boson mass binned by di-lepton mass and transverse mass from the CMS-inspired analysis.

decay.

CMS-Inspired Analysis

Fig. 5.12 shows the plots of $E_\perp^{\mathrm{miss}}$ for the CMS-inspired analysis for the SFOS case according to Tab. 5.6. The top row shows the distributions in the lowest invariant mass, $M_{\ell\ell}$, bin. The first column provides distributions in the lowest transverse mass, M_T, bin. The largest contrast, therefore, is between the upper left-hand plot and the lower right-hand plot.

The $W^\pm Z$ process is dominant in all bins in Fig. 5.12. The leading sub-dominant channel, however, varies across the bins. The middle row of the plots corresponds to the Z mass peak, so here the processes which include a Z boson are naturally very dominant. This leads to the suppression of the $t\bar{t}W^\pm$ process, which is otherwise the leading sub-dominant process, and the $W^\pm H(\to WW^*)$ and $W^\pm H(\to \tau^+\tau^-)$ processes.

Mirroring the behaviour in the ATLAS-inspired analysis, the $t\bar{t}V$ process becomes more significant in the lower right-hand plot, which contains the events with the highest values of $M_{\ell\ell}$ and M_T. These top-associated weak boson production channels become more significant relative to the $W^{\pm}Z$ dominant process both as M_T is increased along the rows in Fig. 5.12 and in the highest $M_{\ell\ell}$ bin as compared with the lowest $M_{\ell\ell}$ bin. In the lowest right-hand plot, $t\bar{t}W^{\pm}$ and $t\bar{t}Z$ contribute $\mathcal{O}(10\,\%)$ and $\mathcal{O}(1\,\%)$ respectively of the $W^{\pm}Z$ contribution.

Conversely, the Higgs boson associated production channels in Fig. 5.12 tend to provide a more significant contribution in the lower $M_{\ell\ell}$ and M_T bins. The $W^{\pm}H(\to WW^*)$ process is most significant in the top left-hand plot, the lowest $M_{\ell\ell}$ and M_T bin. Here, the $W^{\pm}H(\to WW^*)$ process contributes $\mathcal{O}(1\,\%)$ of the $W^{\pm}Z$ cross-section. The distribution in the top left-hand plot shows a strong preference for the $W^{\pm}H(\to WW^*)$ process to contain only a small amount of $E_{\perp}^{\mathrm{miss}}$, with the distribution falling off sharply with increasing $E_{\perp}^{\mathrm{miss}}$. The exception to this trend is the $W^{\pm}H(\to \tau^+\tau^-)$ process, which is a sub-percent effect. This process remains a relatively stable contribution as a percentage of the total cross-section across the bins highest and lowest in $M_{\ell\ell}$. It is suppressed in the lowest left-hand plot, which corresponds to $M_{\ell\ell} > 105\,\mathrm{GeV}$ and $M_T < 120\,\mathrm{GeV}$.

The complementary plots to Fig. 5.12 are given in Fig. 5.13. These show the same observable, $E_{\perp}^{\mathrm{miss}}$, for the SSSF region of the CMS-inspired analysis. This naturally includes a Z boson veto, by excluding any SFOS pair of leptons. The binning is given by the SSSF section of Tab. 5.6. The top row of Fig. 5.13 presents the lowest $M_{\ell\ell}$ bin, $M_{\ell\ell} < 100\,\mathrm{GeV}$, and the first column contains the distributions with $M_T < 120\,\mathrm{GeV}$.

Fig. 5.13 shows $t\bar{t}W^{\pm}$ becoming the dominant process in the bins for $M_{\ell\ell} > 100\,\mathrm{GeV}$, to an extent that was not observed in the previous plots from either the CMS- or ATLAS-inspired analyses. The $W^{\pm}Z$ process is dominant for low $M_{\ell\ell}$, although there are sizeable contributions from both the $t\bar{t}W^{\pm}$ and $W^{\pm}H(\to WW^*)$ processes in these bins as well.

The $W^{\pm}H(\to WW^*)$ process follows a similar pattern in these plots as it did in Fig. 5.12, since it has its most significant contribution in the lowest $E_{\perp}^{\mathrm{miss}}$
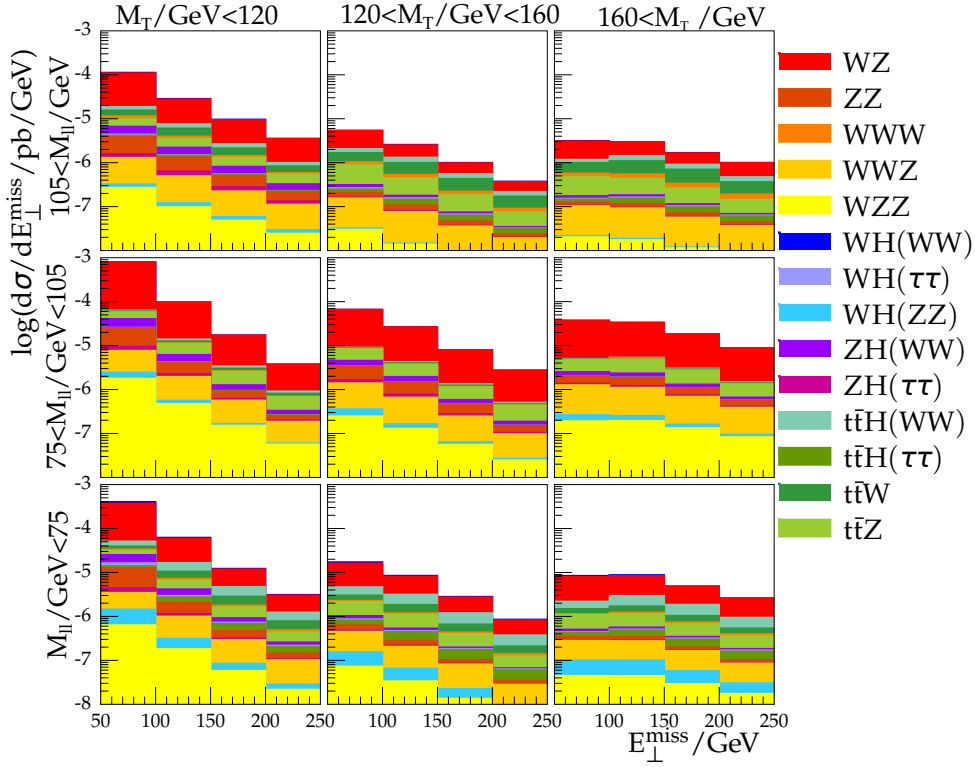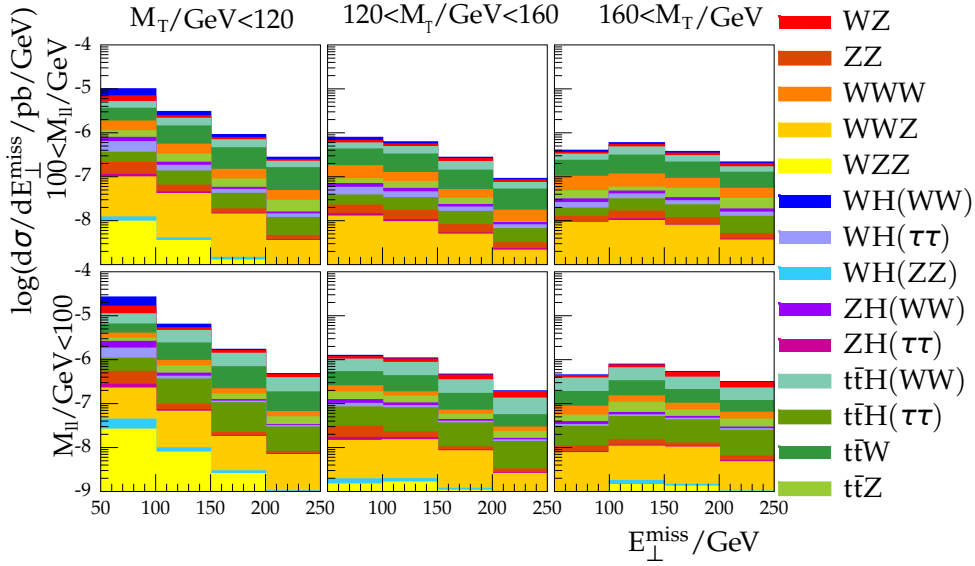
Figure 5.13: Histograms of missing energy of SSSF leptons binned by di-lepton mass and transverse mass from the CMS-inspired analysis.

bin of the top left-hand plot. The trend seen in $t\bar{t}W^{\pm}$ is also familiar from Fig. 5.12, however its effect is enhanced as a result of the SSSF requirement. As this requirement is a veto on SFOS pairs, the Z boson in $W^{\pm}Z$ production is required to decay to τ pairs. This greatly impacts on its contribution to distributions in the SSSF region. Similarly, in Fig. 5.13, the $t\bar{t}Z$ process contributes less significantly than in Fig. 5.12, now becoming less dominant than $W^{\pm}H(\to \tau^{+}\tau^{-})$.

5.2.5   Conclusions

This section presented precision calculations of SM backgrounds to tri-lepton searches performed at ATLAS and CMS in neutralino and chargino searches. Relevant background processes have been modelled with the SHERPA + OPENLOOPS interface at NLO QCD level accuracy, and making use of the S-MC@NLO variant of the MC@NLO method to consistently match the ME to the parton shower.

It was shown that the $W^{\pm}Z$ boson production provides the dominant irreducible background for tri-lepton chargino and neutralino searches, with the $t\bar{t}W^{\pm}$ process contributing significantly in the high-energy tails of these dis-

tributions, and even becoming the dominant irreducible background once a SFOS veto is applied. It was shown that several subleading contributions to the irreducible tri-lepton background are significant enough under realistic experimental cuts to require a precise theoretical modelling.

This section also introduces the NLO QCD computation of top-associated weak boson production, which was not introduced in Sec. 5.1. This introduces a large contribution to the observables, which could be effectively removed with a veto on b-tagged jets in the final state. With this addition, this section presents NLO QCD accurate calculations of rare SM processes which are important for current searches in for new physics in regions not typically populated with SM processes.

Chapter 6

$t\bar{t}HH$ Production at a $14\,\mathrm{TeV}$ LHC

This chapter draws heavily from a collaborative project in Ref. [173].

Searches for multi-Higgs boson final states can constrain parameters of the SM (or extensions thereof) that directly relate to the mechanism of EW symmetry breaking. Multi-Higgs boson production cross-sections, however, are small and the phenomenologically accessible final states are challenging to isolate in the busy multi-jet hadron collider environment of the LHC run 2 and HL-LHC. This makes the necessity to extend the list of potentially observable production mechanisms obvious. Most of the phenomenological analyses in the past have focused on $gg \to HH + $ jets; in this chapter the $pp \to t\bar{t}HH$ process is studied at the HL-LHC and it is found that this channel for $H \to b\bar{b}$ and semi-leptonic and hadronic top decays has the potential to provide an additional handle to constrain the Higgs tri-linear coupling in a global fit at the end of the high luminosity phase.

6.1   Introduction

As was noted in Chap. 1, the properties of the Higgs boson have so far been aligned with the SM expectation [174, 175] for standard measurements. The next step in demystifying the nature of the EW scale will therefore crucially

rely on precise measurements of the Higgs boson's properties at low as well as high momentum transfers during run 2 and the high luminosity phase, and on constraining or even measuring the Higgs boson's properties that have not been in the sensitivity reach during run 1.

A parameter in the SM that is directly sensitive to spontaneous symmetry breaking is the quartic Higgs coupling, η

$$V(\Phi^\dagger\Phi) \;=\; \mu^2\Phi^\dagger\Phi \;+\; \frac{\eta}{2}(\Phi^\dagger\Phi)^2 \;\supset\; \frac{1}{2}m_H^2 H^2 \;+\; \frac{\sqrt{\eta}}{2}m_H H^3 \;+\; \frac{\eta}{8}H^4\,, \quad (6.1)$$

where the unitary gauge $\Phi^T = (0, (v+H)/\sqrt{2})$ is used and $v \simeq 246\,\text{GeV}$. The second independent parameter in the SM Higgs potential $\mu^2 < 0$ is reverse-engineered to obtain an acceptably large value of the EW symmetry breaking scale and pole mass

$$(173\,\text{GeV})^2 \simeq \frac{v^2}{2} = \frac{-\mu^2}{\eta}\,, \quad m_H^2 = \eta v^2 \qquad (6.2)$$

for a given Higgs self-coupling, η. These relations determine a unique value of the Higgs self-coupling in the SM, $\eta = m_H^2/v^2$, as required by renormalisablility.

To obtain a measurement of η, Eq. (6.1) may be thought of as the lowest order in an effective field theory expansion in a new physics scale Λ. A new operator possibly relevant for softening the correlation of Higgs boson mass and EW scale is, e.g., $O_6 = (\Phi^\dagger\Phi)^3$. Consequently, in the absence of additional new resonant phenomena related to EW symmetry breaking and in order to prove or disprove the existence of such operators, a question that needs to be addressed is how well the Higgs self-interaction parameter can be constrained assuming the standard low-energy Higgs boson phenomenology only.

The best option to phenomenologically access the relevant parameter, η, at the LHC is via its impact on di-Higgs boson production [176–182] via the tri-linear Higgs self-coupling. Inclusive di-Higgs boson cross-sections typically have cross-sections in the $\mathcal{O}(10\,\text{fb})$ range [75, 183]. This implies that, in order to analyse them, the large SM-like Higgs boson branching ratios $H \to b\bar{b}, \tau^+\tau^-$ [184–186] and $H \to W^+W^-$ [187] must be employed. Ad-

vanced substructure techniques [188–196] or small irreducible backgrounds such as in $HH \to b\bar{b}\gamma\gamma$ [197–199] are crucial in most analyses to date, which have focused on the dominant di-Higgs boson production cross-section, gluon fusion (GF) with $\sigma^{\mathrm{NLO}} \simeq 30\,\mathrm{fb}$ [200–202]. To increase sensitivities in this channel, emission of an additional jet has been discussed in Refs. [184, 203]; a complete analysis of WBF-like production in $pp \to HHjj$ has become available only recently [204].

Common to all realistic di-Higgs boson analyses discussed in the literature is that they will be sensitive to systematic uncertainties at the end of run 2 and the high luminosity phase, and it is quite likely that measurements in only a single di-Higgs boson channel will not provide enough information to formulate a significant constraint on the Higgs self-interaction in the above sense [205]. Hence, it is mandatory to extend the list of potential phenomenologically interesting search channels in proof-of-principle analyses.

This chapter details a study of $pp \to t\bar{t}HH$, and studies semi-leptonic and hadronic top decays $t \to \ell\nu b, t \to jjb$ and $H \to b\bar{b}$. In particular, it discusses the phenomenological appeal of this particular di-Higgs boson final state as a function of the number of applied b-tags. Firstly, the qualitative behaviour of $pp \to t\bar{t}HH$ is studied in Sec. 6.2, which also comments on the signal and background event generation employed in the remainder of the chapter. The analysis is detailed in Sec. 6.3, where the sensitivity of $pp \to t\bar{t}HH$ to the Higgs tri-linear coupling is discussed in detail before conclusions are presented in Sec. 6.4.

6.2 Signal Cross-Section Sensitivity and Event Generation

The sensitivity of di-Higgs boson cross-sections from GF and WBF is dominated by destructive interference of continuum HH production and the sub-amplitude proportional to the tri-linear coupling λ. In GF this is apparent

from low-energy effective theory arguments [206–208] by expanding

$$\mathcal{L}_{\text{LET}} = -\frac{\alpha_s}{12\pi}G^a_{\mu\nu}G^{a\,\mu\nu}\log\left(1+\frac{H}{v}\right) = \frac{\alpha_s}{12\pi}G^a_{\mu\nu}G^{a\,\mu\nu}\left(\frac{H^2}{2v^2}-\frac{H}{v}\right), \quad (6.3)$$

which makes the relative minus sign between the continuum and the $gg \to H \to HH$ diagrams explicit. As a consequence, the GF cross-section is a decreasing function with $\lambda \gtrsim \lambda_{\text{SM}} = \sqrt{\eta}m_H/2$. In WBF the destructive character is explicit from nested cancellations that are similar to unitarity-based cancellations observed in longitudinal gauge boson scattering.

Qualitatively different from GF- and WBF-induced di-Higgs boson production, $pp \to t\bar{t}HH$ is impacted by *constructive* interference, yielding an increasing cross-section with $\lambda > \lambda_{\text{SM}}$, Fig. 6.1. $pp \to t\bar{t}HH$ production is the biggest di-Higgs boson cross-section among the production modes which exhibit this behaviour ($pp \to WHH$ and $pp \to ZHH$ [75]). Quite different to loop-induced GF di-Higgs boson production, there is no characteristic threshold scale involved in $pp \to t\bar{t}HH$ that can be exploited in a targeted boosted search strategy [184, 185]; the $t\bar{t}HH$ cross-section is a rather flat function of λ [75], as can be seen in Fig. 6.2. Further, differential distributions away from the production threshold do not show a significant deviation apart from a global rescaling of the differential distribution by $\sigma(\lambda \neq \lambda_{\text{SM}})/\sigma(\lambda_{\text{SM}})$ for a transverse momentum range that is interesting for the experiments (Fig. 6.1). Furthermore, the expected inclusive $t\bar{t}HH$ cross-section with $\sigma \simeq 1\,\text{fb}$ at a 14 TeV LHC asks for a selection as inclusive as possible to be sensitive to the signal contribution even for a target luminosity of $3\,\text{ab}^{-1}$ in the first place.

Treating the top-Yukawa interaction as legacy measurement and setting $y_t = y_t^{\text{SM}}$, a physics situation can be imagined which has an enhanced trilinear coupling that renders the dominant GF modes suppressed but leaves an excess in $pp \to t\bar{t}HH$ production. In the general dimension six extension alluded to in the introduction this corresponds to a negative Wilson coefficient of O_6. Enhanced Higgs self-couplings have been discussed more concretely in the context of conformal Coleman-Weinberg-type extensions of the SM in [209]. Obviously, the opposite phenomenological situation of $\lambda < \lambda_{\text{SM}}$ is accompanied by enhanced GF and WBF di-Higgs boson cross-sections while $pp \to t\bar{t}HH$ becomes smaller (however the cross-section becomes rather flat).
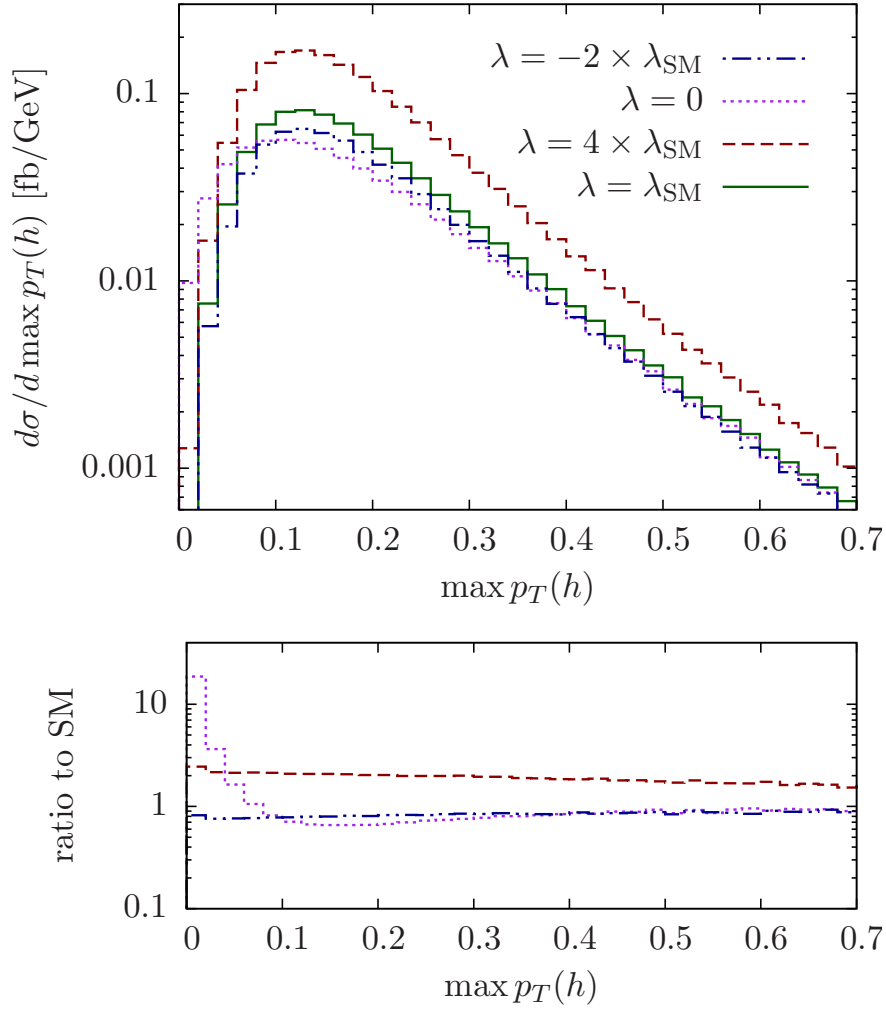
Figure 6.1: Differential distributions at 14 TeV centre of mass energy of the inclusive maximum Higgs boson transverse momentum for different values of the Higgs tri-linear coupling λ. The lower panel displays the ratio of the $\max p_\perp(H)$ distribution with respect to the SM ($\lambda = \lambda_{SM}$).

Such a situation occurs for instance in composite Higgs scenarios [181, 182], which typically have a smaller Higgs tri-linear coupling than predicted in the SM (in addition to modified top Yukawa interactions). Therefore, comparing the measured rates and (ideally) distributions in all three channels, i.e. GF, WBF and in association with a top quark pair, provides a precision tool for BSM EW symmetry breaking.

	signal		backgrounds					
	$\lambda = \lambda_{\mathrm{SM}}$	$\lambda = 4\,\lambda_{\mathrm{SM}}$	$t\bar{t}bbbb$	$t\bar{t}hbb$	$t\bar{t}hZ$	$t\bar{t}Zbb$	$t\bar{t}ZZ$	$Wbbbb$
trigger	0.10	0.23	4.75	1.38	0.64	1.37	1.36×10^{-2}	1.33
jet cuts	7.40×10^{-2}	0.17	1.44	0.76	0.40	0.65	8.74×10^{-3}	7.46×10^{-2}
5 b tags	1.23×10^{-2}	2.83×10^{-2}	4.46×10^{-2}	6.19×10^{-2}	7.24×10^{-3}	4.43×10^{-2}	1.25×10^{-3}	5.35×10^{-4}
$2\times h \to b\bar{b}$	7.33×10^{-3}	1.69×10^{-2}	1.59×10^{-2}	2.71×10^{-2}	3.41×10^{-3}	1.56×10^{-2}	4.28×10^{-4}	$<1\times10^{-4}$
lep./had. t	5.04×10^{-3}	1.12×10^{-2}	9.50×10^{-3}	1.66×10^{-2}	2.29×10^{-3}	9.42×10^{-3}	2.69×10^{-4}	$<1\times10^{-4}$
lep. t only	2.33×10^{-3}	5.29×10^{-3}	5.03×10^{-3}	9.36×10^{-3}	1.14×10^{-3}	4.90×10^{-3}	1.39×10^{-4}	$<1\times10^{-4}$
had. t only	2.71×10^{-3}	5.93×10^{-3}	4.47×10^{-3}	7.20×10^{-3}	1.16×10^{-3}	4.44×10^{-3}	1.30×10^{-4}	$<1\times10^{-4}$
6 b tags	2.21×10^{-3}	4.97×10^{-3}	3.80×10^{-3}	8.01×10^{-3}	9.57×10^{-4}	5.10×10^{-3}	1.86×10^{-4}	$<1\times10^{-4}$
$2\times h \to b\bar{b}$	1.81×10^{-3}	5.94×10^{-3}	2.01×10^{-3}	5.47×10^{-3}	6.60×10^{-4}	3.28×10^{-3}	1.11×10^{-4}	$<1\times10^{-4}$

Table 6.1: Cut flow for the analysis outlined in Subsec. 6.3.1. Boson decays in the background samples are generated fully inclusive.
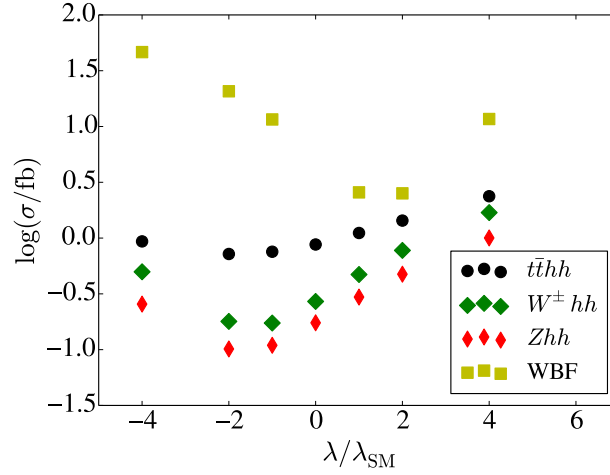
Figure 6.2: cross-sections for different HH production channels at 14 TeV for different values of the Higgs boson tri-linear self-coupling, λ as a fraction of the SM value, λ_{SM}.

Given the small production cross-sections, in the following a combination of semi-leptonic and hadronic decays of the final state top pair are focused on, with both Higgs bosons decaying $H \rightarrow b\bar{b}$. SHERPA v2.1.1 is used with the COMIX ME generator [20, 64] to generate signal and background events for modified tri-linear Higgs couplings with SM-like top Yukawa interactions and normalised to the signal events. These event samples are normalised to the NLO cross-sections extracted from Ref. [75] for the different values of λ, after validating the calculation against the leading order results of Ref. [75], provided in Fig. 6.2. This means applying a flat K-factor to the signal events. The signal and background samples have been generated at purely leading order matched to the parton shower, with modelling of hadronisation effects and underlying event. Unstable particles are treated in the narrow width approximation; any spin correlations are included in the SHERPA simulation.

Fig. 6.2 shows the behaviour of some Higgs boson production mechanisms. As well as those shown here, Ref. [75] includes single-top associated Higgs boson production and loop-improved effective field theory calculations of GF. The $tt̄HH$ process provides the second largest contribution to the di-Higgs boson production channels in Fig. 6.2. The WBF process is more dominant, but involves the same destructive interferences of the GF process. The associated production channels become larger with respect to the $tt̄HH$ process in the

limit $\lambda/\lambda_{\mathrm{SM}} \gg 1$.

The scales are set according to Ref. [133], and the masses and widths of the SM particles used in the event generation are

$$
\begin{aligned}
M_Z &= 91.188\,\mathrm{GeV}\,, \\
M_W &= 80.419\,\mathrm{GeV}\,, \\
M_H &= 126\,\mathrm{GeV}\,, \\
M_t &= 173\,\mathrm{GeV}\,.
\end{aligned}
\tag{6.4}
$$

6.3 $tt̄HH$ at HL-LHC

6.3.1   Final State Reconstruction

While this high-multiplicity final state might allow to trigger in multiple ways, an isolated lepton (muon or electron) with $p_{\perp,l} > 10\,\mathrm{GeV}$ is relied on for this purpose due to the low $p_\perp$ threshold for the jets. A lepton is defined
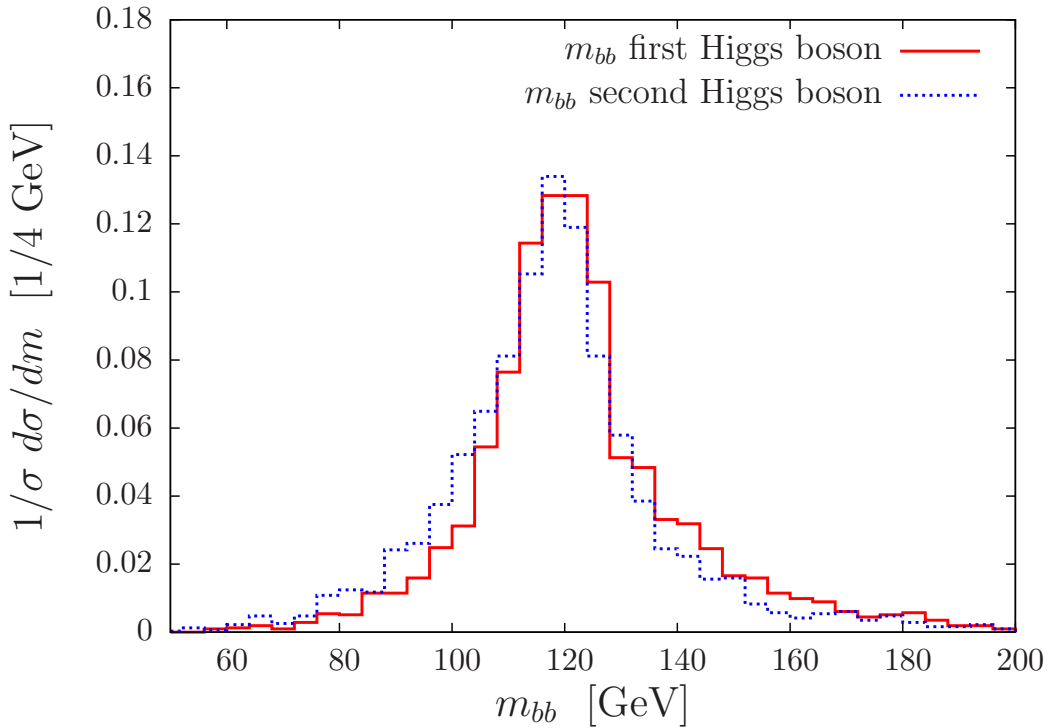
Figure 6.3: Reconstructed invariant mass of bottom-quark pairs based on Eq. (6.5) for $\lambda = \lambda_{\mathrm{SM}}$.

to be isolated if the hadronic energy deposit within a cone of size $R = 0.3$ is smaller than $10\,\%$ of the lepton candidate's transverse momentum and $|y_l| < 2.5$.

After removing the isolated leptons from the list of input particles ($|y| < 4.5$) of the jet finder, jets are reconstructed with $R = 0.4$ and $p_{\perp,j} > 30\,\text{GeV}$ using the anti-k_T algorithm [158] of FASTJET [159]. Events are vetoed with less than 6 reconstructed jets.

Out of the 6 jets, at least 5 are required to be b-tagged by matching the b-meson before the decay to the jet. A b-tagging efficiency of $70\,\%$ and a fake rate of $1\,\%$ [210] is assumed.

As the signal rate after these inclusive cuts is already fairly small, $\mathcal{O}(10^{-2}\,\text{fb})$ for $\lambda = \lambda_{\text{SM}}$, the Higgs-decay jets are found by minimising

$$\chi^2_{HH} = \frac{(m_{b_i,b_j} - m_H)^2}{\Delta^2_H} + \frac{(m_{b_k,b_l} - m_H)^2}{\Delta^2_H} , \qquad (6.5)$$

where $k \neq l \neq i \neq j$ run over all b-tagged jets and $m_H = 120\,\text{GeV}$ (This choice is commented on further below) and $\Delta_H = 20\,\text{GeV}$. For the combination which minimises χ^2, $|m_{b_i,b_j} - m_H| \leq \Delta_H$ and $|m_{b_k,b_l} - m_H| \leq \Delta_H$ is required. These 4 b-tagged jets are then removed from the event.

To confidently reduce the large gauge boson induced backgrounds, e.g. $W^{\pm}$+jets, at least one top quark is further required to be reconstructed. Cross-sections are provided after the reconstruction of the leptonic top only; after reconstructing the hadronic top quark only; or after reconstructing either the leptonic or the hadronic top quark.

To avoid biasing the vector boson backgrounds towards the top quark signal, for the leptonic top quark reconstruction the invariant mass of the sum of the lepton, a b-jet and the missing transverse energy vector, built from all visible objects within $|y| < 4.5$, is required to fulfil

$$|m_{\ell,b,\not{E}} - m_t| \leq \Delta_t . \qquad (6.6)$$

with $m_t = 170\,\text{GeV}$ and $\Delta_t = 40\,\text{GeV}$, which reflects the incomplete missing energy reconstruction from the top decay. To identify the b-jet for $m_{\ell,b,\not{E}}$, all
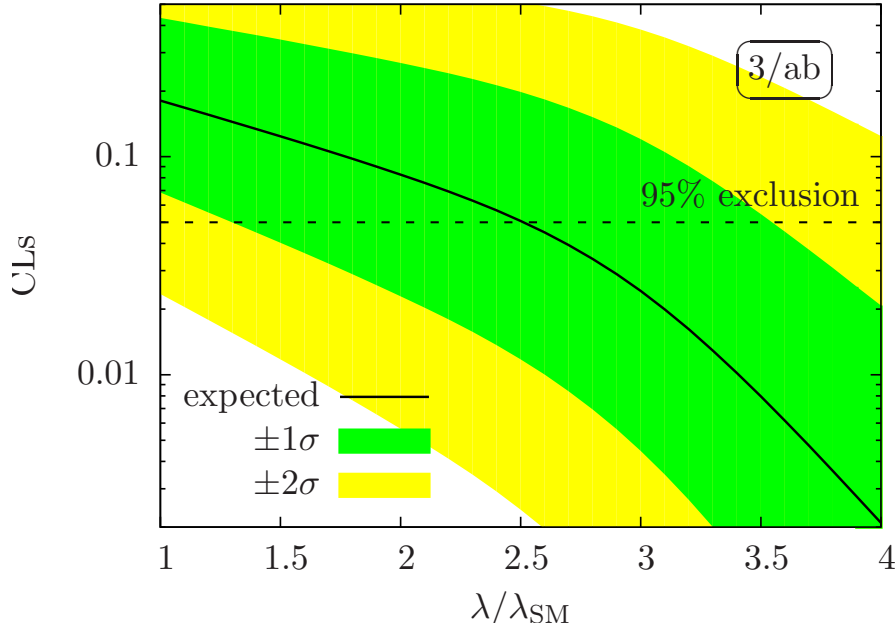
Figure 6.4: Expected confidence levels for the analysis of Subsec. 6.3.1 as a function of the tri-linear Higgs coupling λ.

remaining b-jets in the event are considered and

$$\chi^2_{t_\ell} = \frac{(m_{\ell,b_i,\not{E}} - m_t)^2}{\Delta^2_t} \qquad (6.7)$$

is minimised. Similarly, for the hadronic top quark reconstruction, all remaining jets are looped over and

$$\chi^2_{t_H} = \frac{(m_{j_i,j_k,j_l} - m_t)^2}{\Delta^2_t} \qquad (6.8)$$

is minimised. Then

$$|m_{j_i,j_k,j_l} - m_t| \leq \Delta_t \qquad (6.9)$$

is requested.

The cut flow for the described analysis steps is shown in Tab. 6.1.

6.3.2 Discussion

At a centre-of-mass energy of 14 TeV, the signal cross-section for $t\bar{t}HH$ is in the sub-femtobarn range before decays are included. Therefore, the reconstruction requires an approach that on the one hand retains an as-large-as

possible signal yield and on the other hand triggers in the high-luminosity regime. Therefore this study focuses on the Higgs boson decays to bottom quarks and semi-leptonic $t\bar{t}$ decays. Other channels can be combined with this to improve the sensitivity on measuring the self-coupling.

Already after fulfilling the trigger requirement, minimal jet cuts and 5 b tags, a signal-to-background ratio, $S/B \simeq 1/15$, is found for the backgrounds considered. To confirm the measurement of a di-Higgs boson event, both Higgs bosons have to be fully reconstructed. At this stage it is found that $S/B \simeq 1/9$ with 5 b tags and $S/B \simeq 1/6$ with 6 b tags respectively. The reconstructed masses of the hardest and second hardest Higgs boson are shown in Fig. 6.3. Due to the partly invisible decay of B-mesons, m_H is systematically shifted to slightly lower values. This is why $m_H = 120$ GeV is chosen for the minimisation procedure for the purpose of this chapter, guided by comparisons against Monte Carlo truth. In measurements, the experiments can compensate for this systematic shift in the invariant Higgs boson mass using b-jet calibrations. Further, at this point with the chosen b-tagging-efficiency working point, $W^{\pm}$+jets backgrounds are already subleading. Thus, choosing a higher b-tagging efficiency working point at the cost of a larger fake rate could be beneficial in this analysis to retain a larger signal yield and improve the statistical significance expressed in $S/\sqrt{B}$.

In a further step, a leptonic or hadronic top quark reconstruction is performed using the remaining measured final state objects. This can help to further suppress potentially large reducible QCD-induced backgrounds, e.g. $W^{\pm}$+jets. However, for the top-rich irreducible backgrounds focused on in this study, an improvement in S/B cannot be achieved using the signal-sparing χ^2 minimisation applied.

From Tab. 6.1 it becomes obvious that the signal vs. background ratio is expected to be in the 10 % range for $\lambda = \lambda_{\rm SM}$. After 3 ab^{-1} 13 signal events are expected including the reconstruction of a top quark and 22 signal events reconstructing only the two Higgs bosons. While the signal yield is too small to claim a discovery at this stage, the number of observed events is high enough to formulate an expected 95% confidence level limit on λ assuming $y_t = y_t^{\rm SM}$. In order to do this, the CLs method [211–214] is employed, inputting the expected number of signal and background events for a luminosity of 3 ab^{-1}

including the reconstruction of at least one top quark. The result is shown in Fig. 6.4; and yields

$$\lambda \lesssim 2.51 \ \lambda_{\mathrm{SM}} \text{ at } 95\,\% \text{ CLs.} \tag{6.10}$$

Together with analyses of the $b\bar{b}\gamma\gamma$ and $b\bar{b}\tau\tau$ channels that yield a confidence interval $\lambda \gtrsim 1.3 \ \lambda_{\mathrm{SM}}$ [185, 197, 198], depending on systematic uncertainties, $t\bar{t}HH$ will allow to extend the sensitivity to λ to a parameter region that is not accessible via the former modes.

6.4 Summary and Conclusions

With current Higgs boson property measurements strongly indicating a SM-like character of the discovered Higgs boson, analysis strategies for parameters relevant for EW symmetry breaking that remain unconstrained in standard Higgs boson searches will play a central role in the search for new physics beyond the SM during run 2. Constraining the Higgs self-interaction, as one of the most interesting couplings in this regard, is an experimentally challenging task, and will require a large accumulated data set.

As is discussed in this chapter, the role of $pp \to t\bar{t}HH$ production in this regard is twofold:

1. It provides an additional channel that can be added to a global Higgs boson self-coupling analysis across the phenomenologically viable channels. Signal vs. background ratios indicate that top-pair associated Higgs boson pair production can provide significant statistical power to increase the sensitivity to this crucial coupling at a targeted $3\,\mathrm{ab}^{-1}$ and extend the sensitivity coverage to the Higgs boson tri-linear coupling.

2. If a situation with $\lambda \gtrsim \lambda_{\mathrm{SM}}$ exists, $pp \to t\bar{t}HH$ provides the *leading* channel, where an excess over the SM expectation can be expected. A negative search outcome in GF and WBF dominated search strategies in addition to an excess in $t\bar{t}HH$ final states would therefore be a

strong indication of $\lambda > \lambda_{\mathrm{SM}}$, eventually allowing strong constraints to be placed on BSM scenarios such as composite Higgs boson models.

Part III

Physics at future colliders

Chapter 7

EW Processes at a $100\,\mathrm{TeV}$ pp Collider

This chapter presents studies of SM processes extended to a proton-proton collider with a centre-of-mass energy of $100\,\mathrm{TeV}$. This explores the possibilities and challenges faced at such high energies for SM processes relevant for new physics searches at high energies, with a focus on the rare processes with high lepton multiplicity. It provides an extension of the studies in Chap. 5.

7.1 Introduction

Previous chapters have focussed on LHC physics. Chap. 5 detailed studies into some of the rare EW SM processes relevant for the LHC, while Chap. 6 investigated a channel for one remaining avenue of searches in the Higgs sector; the Higgs boson self-couplings. Current searches for di-Higgs boson production are restricted by a low cross-section at $8\,\mathrm{TeV}$ [215, 216]. However, given the potential at higher energy colliders, there have been significant theoretical studies into the potential for di-Higgs boson production for 14 and $100\,\mathrm{TeV}$ [217] machines. Chap. 6 provides details on the current theory for a $14\,\mathrm{TeV}$ LHC.

While the physics from the Higgs sector has been very rich from the LHC, the search for physics beyond the SM has not been as rewarding. As a result of this, searches for new particles are being pushed to higher and higher

energies, and to fully investigate any high scale new physics, a future collider
will be essential. A recently proposed 100 TeV collider (VLHC) could reach a
total luminosity of $1\,\mathrm{ab}^{-1}$ [17], where many processes too rare for study at the
LHC could be investigated. In particular, this is of interest in multi-Higgs
boson production, where measurements of the Higgs boson self-couplings
would provide the final SM parameters.

There has been considerable interest on the theory side in the possibilities of
a 100 TeV collider. To date, many of these studies have focused on:

1. Higgs boson production [217–221]

2. The discovery potential for BSM physics [222–231].

3. Studies into the general properties of a 100 TeV collider and SM pro-
   cesses [17, 232, 233].

This chapter falls into the third category, providing an overview of some key
SM processes at high energy studies. These involve backgrounds to BSM
studies as well as Higgs boson self-coupling studies.

Studying known SM physics in a 100 TeV pp environment is vital for any
definitive statements to be made about new physics at such a machine. As
Higgs boson couplings and BSM physics are the most immediate motivations
for a high energy pp collider, this chapter focuses on SM processes relevant
to these searches, as well as providing some insights into further stringent
tests of the SM that would become available at a 100 TeV collider.

7.1.1   Processes Studied

This chapter presents total cross-section results for multiple weak boson pro-
duction, both in pure weak boson production and in top pair associated
production, as a 100 TeV extension to the multi-lepton studies in Chap. 5.
Differential distributions are also shown for these processes, binned by lep-
ton multiplicity. This provides a handle on the 100 TeV backgrounds to BSM
searches carried out as a continuation of LHC studies.

Beyond their importance as backgrounds in many BSM searches, these multi-
ple weak boson production processes are interesting in their own right. Top

quarks are unique in the SM, being the only fundamental fermion with a mass of order of the EW scale, their interactions with the EW gauge bosons is of considerable theoretical and experimental interest. At the LHC, $t\bar{t}V$ production has been studied both in its own right and as a background to BSM physics, as in Chap. 5. V^n processes, for $V = W^{\pm}, Z$, are studied in searches for anomalous gauge couplings, for which limits have been placed by both the ATLAS and CMS experiments at the LHC [234–237]. These studies will continue at any future high energy collider.

Furthermore, measurements of multiple weak boson production can provide insights into the restoration of SU(2) invariance at high energies. This symmetry would imply an equal production rate for each weak boson, W^+, W^- and Z. At the TeVatron and the LHC, the interaction energies are typically too close to the mass threshold for this symmetry to be realised. At the TeVatron, the proton-antiproton collisions provided an equal treatment of valence quarks and anti-quarks. This initial state therefore has no preference for the production of W^+ bosons over W^- bosons, and while there was an introduced asymmetry in the rapidity distributions, the overall rates were equivalent. However, the production rate of Z bosons was not equivalent to that of the $W^{\pm}$ bosons, and therefore the broken nature of SU(2) could be observed. At the LHC, the symmetric proton-proton initial state includes an intrinsic bias towards quarks over anti-quarks, and u quarks over d quarks. This manifests itself as an increased production of W^+ bosons over W^-. At the relatively low energy of the LHC, it is very rare to observe events with 3 or more weak bosons, making the study of production rates as a function of boson multiplicity impossible. However, at a 100 TeV collider the total cross-section for high-multiplicity boson states increases, allowing the production rate of each weak boson to be studied as a function of total boson multiplicity. This behaviour then allows the possible restoration of SU(2) symmetry to be studied.

The second class of processes considered in this chapter are WBF production of multiple Higgs bosons. Total cross-section results are presented for $H^n j^{m+2}$, where $n = 1, 2, 3$ and $m = 0, 1, 2$. The effect the inclusion of additional Higgs bosons and QCD radiation has on the total cross-sections is discussed, and the potential for Higgs boson self-coupling measurements to

be made for this production channel is analysed.

7.1.2 Limitations

Extrapolating current physics models to 100 TeV is not trivial, with such a large increase in centre-of-mass energy introducing several new theoretical considerations. Since many SM processes exist naturally about the EW scale, studying these processes at a 100 TeV collider means probing partons with very small momentum fractions, x. At sufficiently small x the parton distribution functions are not well measured, and the appropriate factorisation scheme is not obvious. It is possible to begin to enter a regime in which the typical DGLAP [238–240] factorisation does not provide an accurate description and an alternative, such as BFKL [241–245], may need to be implemented. However, the processes studied in this chapter should not require probing sufficiently small x that this consideration is significant to the results.

A similar concern regarding the limitations of the parton distribution functions is that the high hadronic centre-of-mass energy motivates the consideration of EW scale particles in the parton distribution functions, such as top quarks and the weak bosons.

This chapter does not attempt to address these potential limits of current physics understanding, although it is important to bear them in mind for any theoretical predictions of 100 TeV physics. Modelling of multiple parton interactions has not been studied or validated at such high energies. It is important to study these events in their own right before considering these as underlying events to hard processes. As a result, multiple parton interactions are not included in the distributions, only the hard process and subsequent parton showering.

7.1.3 Scaling

The radiation pattern of QCD partons in SM processes obey scaling laws, which permit calculations at low parton multiplicity to be extended to higher multiplicity regions without the full calculation of the more complicated

hard process becoming necessary. These scaling studies can be performed at 100 TeV to establish how scaling behaves with increasing centre-of-mass energy.

Scaling discussions are often focused on QCD radiation. However, at high energies such as 100 TeV the emission of weak bosons and Higgs bosons can occur at scales much below the centre-of-mass energy of a collision. It is possible that this radiation of weak bosons is also subject to similar scaling laws as are familiar with QCD emissions. This is investigated in pure weak boson production as well as $t\bar{t}V^n$. The scaling behaviour observed in QCD radiation falls into two categories, as discussed in Refs. [246, 247], staircase and Poisson. Staircase scaling implies a ratio, $R_{(n+1)/n}$, of cross-sections for $(n+1)$ QCD emissions to n QCD emissions of some constant K, as

$$R_{(n+1)/n} = \frac{\sigma_{n+1}}{\sigma_n} = K \,. \tag{7.1}$$

The other known behaviour for the scaling behaviour is Poisson scaling, where the same ratio of cross-sections is now given by

$$R_{(n+1)/n} = \frac{\sigma_{n+1}}{\sigma_n} \propto \frac{1}{n+1} \,. \tag{7.2}$$

7.1.4 Set-Up

The set-up of the calculation is in line with Chap. 5, however the calculations are performed with LO SHERPA [20] event generation with the COMIX [64] ME generator. For the distributions, two additional QCD jets are included from the hard process with the CKKW method [117] described in Chap. 2. The weak bosons and top quarks in the distributions are calculated on-shell in the narrow width approximation, and the decays are factorised with spin information preserved. The kinematics are then reshuffled onto a Breit-Wigner distribution, as described in Subsec. 5.1.2. No hadronisation or multiple parton interaction effects are included in the distributions, although for the generic event observables shown these effects should be small.

For scale choices and cuts for specific processes see the relevant section.

N jet	0		1	
QCD Order	LO/pb	NLO/pb	LO/pb	LO/pb
Jet Cut/GeV			50	100
$t\bar{t}W^{\pm}$	6.795(8)	18.91(6)	12.68(4)	9.35(3)
$t\bar{t}Z$	37.5(1)	61.7(2)	42.7(2)	24.3(1)
$t\bar{t}W^{+}W^{-}$	0.814(3)		1.138(6)	0.689(3)
$t\bar{t}ZZ$	0.1277(4)		0.1822(8)	0.1138(5)
$t\bar{t}W^{\pm}Z$	0.0820(1)		0.1580(6)	0.1127(5)
$t\bar{t}W^{+}W^{-}W^{\pm}$	0.002414(5)		0.00481(1)	0.00375(2)
$t\bar{t}W^{+}W^{-}Z$	0.01418(5)		0.0241(1)	0.01535(7)
$t\bar{t}W^{\pm}ZZ$	0.00113(3)		0.002204(9)	0.001708(8)
$t\bar{t}ZZZ$	0.0009450(4)		0.00147(1)	0.000940(1)

Table 7.1: Cross-sections for inclusive multiple vector boson production in association with a top pair, with up to 1 additional QCD jet from the ME, given for a $p_{\perp}$ cut on the jet of 50 and 100 GeV. The scale used in these calculations is the sum of the masses and $p_{\perp}$ of all final state particles divided by the number of final state particles.

7.2 $t\bar{t}V^{n}$ Production

This section presents total cross-sections for $t\bar{t}V^{n}$ production, where $V = W^{\pm}, Z$. Tab. 7.1 shows that these processes will be observable at a 100 TeV collider up to $n = 3$, where processes typically have cross-sections in the femtobarn range. This is a considerable improvement in sensitivity over the LHC, which typically only reaches $n = 1$.

Tab. 7.1 presents cross-sections for $t\bar{t}Vj^{m}$ production, for $m = 0, 1$. Two different jet $p_{\perp}$ definitions are considered, $p_{\perp} > 50$ GeV and $p_{\perp} > 100$ GeV. The effect the additional QCD radiation from the hard process on the cross-section is significant; it demonstrates that these processes are more frequently than not associated with a 50 GeV jet. This preference results from the introduction of the quark-gluon initial state with the additional QCD radiation. Without this QCD radiation, $t\bar{t}V^{n}$ requires a quark-antiquark initial state for charged V^{n}, and either a quark-antiquark or a pure gluonic initial state for neutral V^{n}. In both of these cases, the mixed quark-gluon initial state is unavailable, leading to a significant restriction of phase-space. This implies that higher order corrections are likely to be very important to $t\bar{t}V^{n}$, as demonstrated by the large NLO QCD K-factors in Tab. 7.1. This shows
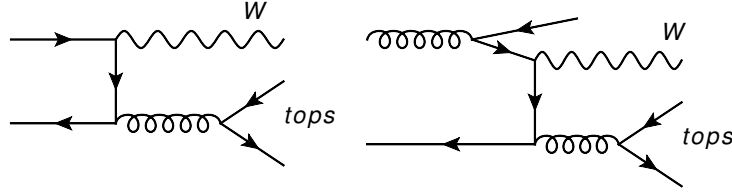
Figure 7.1: Diagrams for the production of $t\bar{t}W^{\pm}$ with (left-hand-side) and without (right-hand-side) an additional QCD radiation. An example diagram for $t\bar{t}W^{\pm}j$ production, from the dominant qg production channel, is shown.

the NLO QCD K-factor for $t\bar{t}W^{\pm}$ to be 2.78, and a smaller K-factor of 1.65 for $t\bar{t}Z$. The kinematics of the event could easily be dominated by this additional QCD radiation, implying that many observables in the NLO QCD calculation will only be LO accurate.

The gluon PDF distribution increases more rapidly in the low-x region than the quark PDF, implying a gluon-dominated regime in the low-x region. Therefore, for purely gluonic initial states, the production of neutral final states suffers from the typical low energy scale of the gluons. This restricts the contribution they provide to hard processes such as $t\bar{t}V^n$ production. Consequently, in all $t\bar{t}V^n$ boson production processes the quark-gluon channel (which is opened up with the additional QCD radiation) introduces a considerable contribution to the cross-section.

Considering the production of a charged final state, at leading order with no additional jets from the hard process, the initial state partons are necessarily a quark pair such that the $W^{\pm}$ boson can be emitted from the initial quark line, as shown in the left-hand diagram in Fig. 7.1. Once an additional QCD radiation is forced from the ME, the quark-gluon initial state becomes available, shown in the right-hand diagram of Fig. 7.1, which therefore greatly increases the overall cross-section for the process. It is the case for a charged final state that considering both a jet $p_{\perp}$ of 50 and 100 GeV in addition to the $t\bar{t}V^n$ process yields a larger cross-section than when no QCD radiation from the ME is considered. The result of the NLO QCD calculation is given for the $t\bar{t}W^{\pm}$ process in Tab. 7.1, which shows similar behaviour to the real emission of QCD radiation from the LO process with a K-factor of 2.78.

The discussion is not as simple for neutral final states, because a neutral final state can include either 0 or 2 final state $W^{\pm}$ bosons. Since the behaviour

Process	1 jet 50 GeV/LO	1 jet 100 GeV/LO
$t\bar{t}W^{\pm}$	1.866(6)	1.376(5)
$t\bar{t}Z$	1.139(6)	0.648(3)
$t\bar{t}W^{+}W^{-}$	1.398(9)	0.846(5)
$t\bar{t}ZZ$	1.427(8)	0.891(5)
$t\bar{t}W^{\pm}Z$	1.927(8)	1.553(9)
$t\bar{t}W^{+}W^{-}W^{\pm}$	1.993(6)	1.553(9)
$t\bar{t}W^{+}W^{-}Z$	1.700(9)	1.083(6)
$t\bar{t}W^{\pm}ZZ$	1.950(9)	1.512(8)
$t\bar{t}ZZZ$	1.56(1)	0.995(4)

Table 7.2: The ratio of the 1 jet cross-section to 0 jet cross-section at LO calculated from the cross-section for an additional jet at $p_{\perp} = 50\,\text{GeV}$ and $p_{\perp} = 100\,\text{GeV}$ for 100 TeV proton-proton production of $t\bar{t}V^{n}$.

of $W^{\pm}$ bosons differs greatly from Z bosons in this process, the two cases of differing $W^{\pm}$ boson multiplicity will be considered separately.

Beginning with 0 $W^{\pm}$ bosons, it can be seen from Tab. 7.1 that for $t\bar{t}Z^{n}$ production, the increase in cross-section produced by the presence of an additional jet falls off more sharply with jet $p_{\perp}$ than for $t\bar{t}W^{\pm n}$ production. The $t\bar{t}Z$ production process can access the gluonic initial state that the $t\bar{t}W^{\pm}$ process cannot, which partially reduces the penalty received for lacking the dominant quark-gluon initial state production channel. $t\bar{t}Z^{n}j$ processes have a larger cross-section than $t\bar{t}Z^{n}$ for jets with $p_{\perp} = 50\,\text{GeV}$, whereas for jets with $p_{\perp} = 100\,\text{GeV}$, $t\bar{t}Z^{n}j$ has a smaller cross-section than $t\bar{t}Z^{n}$. This indicates the reduced sensitivity of $t\bar{t}Z^{n}$ to the quark-gluon initial state over $t\bar{t}NW^{\pm}$, where N represents a neutral combination of $(n-1)$ gauge bosons.

The third final state to consider is that of a neutral final state which contains $W^{+}W^{-}$. $W^{+}W^{-}$ can be produced via a neutral boson propagator or as a result of emission from the initial state. For the latter production channel, the initial state is again forced to be a quark-quark interaction. Tab. 7.1 shows $t\bar{t}W^{+}W^{-}$ as having a similar behaviour to $t\bar{t}ZZ$ with respect to additional radiation. $t\bar{t}W^{+}W^{-}Z$ is alone in the neutral processes as having a larger cross-section when a jet is produced with $p_{\perp} = 100\,\text{GeV}$ than with no jet from the hard process.

A list of the relative corrections to the LO process from an additional QCD emission is given in Tab. 7.2. This shows that for each final state as sep-

n	$\frac{\sigma_{t\bar{t}V^{n+1}}}{\sigma_{t\bar{t}V^{n}}}$	+1 jet (50 GeV)	+1 jet (100 GeV)
1	0.02331(9)	0.0267(1)	0.0272(1)
2	0.01824(8)	0.0220(1)	0.0238(1)

Table 7.3: The scaling ratios for $t\bar{t}V^n$ production in association with weak bosons $W^\pm$, Z for $n =$1,2 bosons.

arated above, charged, $t\bar{t}Z^n$ and $t\bar{t}W^+W^-Z^m$, there is a tendency for the 1 jet cross-section to increase with respect to the 0 jet cross-section. This behaviour becomes more pronounced with increasing final state boson multiplicity. As the number of bosons in the final state increases, so does the required centre-of-mass energy. Therefore, as the boson multiplicity increases, the 50 and 100 GeV jet cuts are increasingly soft in comparison. This pushes the calculation into a regime where the soft limit is included in the hard process. The definition of a jet in $p_\perp$ must be sufficiently high as to remove this contribution.

The scaling behaviour of $t\bar{t}$ production with weak boson multiplicity is difficult to see with the available EW boson multiplicities. Tab. 7.3 shows the relevant ratio for the 0 and 1 jet case, and this suggests a possible approximate staircase scaling. Tab. 7.3 shows a reasonably constant ratio $\sigma_{n+1}/\sigma_n \sim K$, where K is some constant, and σ_n represents the total cross-section for $t\bar{t}$ production associated with n weak bosons. The constant K increases when an additional QCD jet is included from the hard process. It is higher again for a jet $p_\perp > 100$ GeV. This behaviour is observed for the sum over all weak bosons, and a similar behaviour is not observed for any subcategory, such as $W^\pm$ boson emission only, or exclusively charged or neutral final states.

7.3 Multiple Weak Boson Production

This section presents total cross-sections for V^m production. Fig. 7.2 gives the average numbers of W^+, W^- and Z bosons which are produced per event of each exclusive boson multiplicity. The increased weak boson multiplicity corresponds to increased centre-of-mass energy of a collision, and, as this energy becomes much larger than the EW scale, the SU(2) symmetry of the weak bosons should be restored. It is therefore expected that the produc-
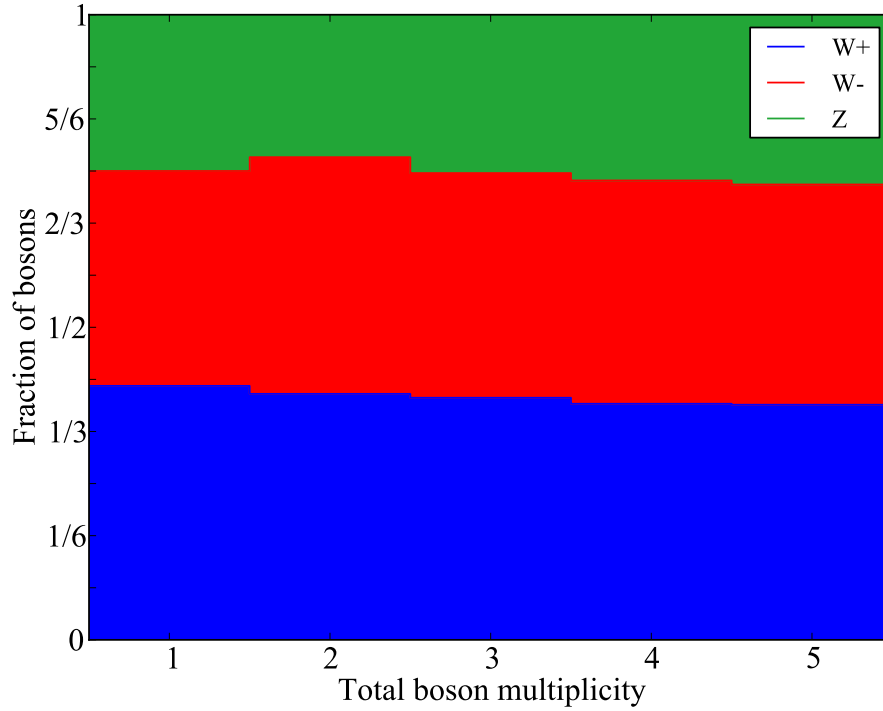
Figure 7.2: The relative abundance of each weak boson at different multiplicities of weak boson production at a scale of $\hat{s}$.

tion fraction of each of these bosons tends towards $\frac{1}{3}$ with increasing boson multiplicity.

Fig. 7.2 shows a trend towards the restoration of the SU(2) symmetry at high weak boson multiplicity. There is a clear preference for the production of W^+ bosons for single boson production, and a suppression of Z boson production. The relative abundance of W^- bosons increases in di-boson final state due to the large cross-section for W^+W^- production. At the higher boson multiplicities, however, the relative production of the $W^\pm, Z$ bosons tend towards $\frac{1}{3}$ in each case, indicating the restoration of SU(2) invariance. The trend is very slow and towards the high end of the boson multiplicity begins to level out, with a residual preference for W^+ production over the other weak bosons.

The total cross-sections for each boson multiplicity can be found in Tab. 7.4. This shows a rapid decline in the overall cross-section for the production of
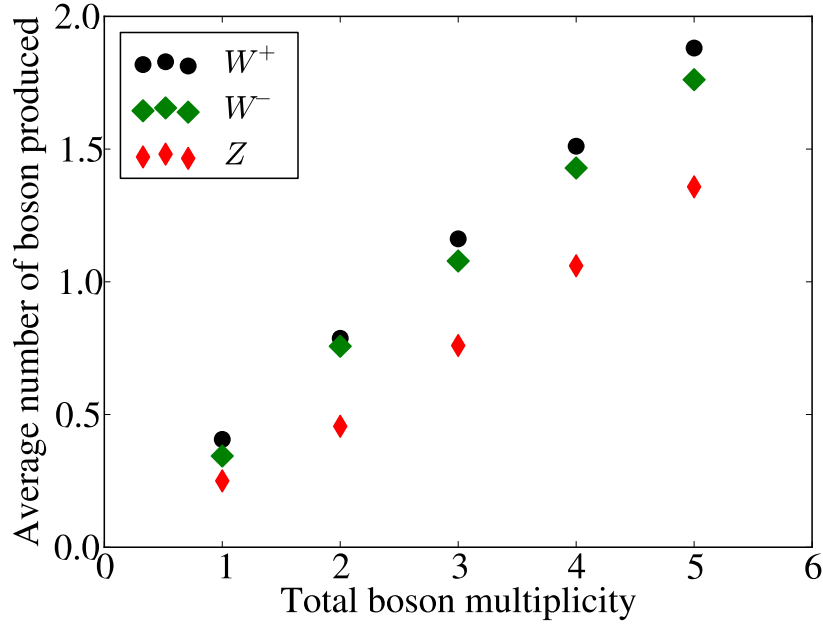
Figure 7.3: The number of each weak boson produced, on average, for each exclusive total boson multiplicity.

gauge bosons as a function of gauge boson multiplicity. This spans a range of 9 orders of magnitude, and in the highest multiplicity case considered, 5 final state weak bosons, the production rate is of the order of femtobarns. Such cross-sections should be readily available to a 100 TeV collider, and a study into the behaviour of SU(2) invariance at high energies would therefore be feasible.

Fig. 7.3 illustrates the behaviour of the average number of each weak boson produced at each boson multiplicity. The expected production rate of the W^+ boson is consistently higher than that of either of the other weak bosons. The average multiplicity of each kind of weak boson increases linearly with increasing total boson number.

The production of multiple weak bosons with no other associated particle is the cleanest environment to consider weak boson scaling. The ratio of $R = \sigma_{n+1}/\sigma_n$, where n denotes weak boson multiplicity, tends to increase with n in Tab. 7.4. From the categories considered – Z boson production, $W^\pm$ boson production, neutral final states and charged final states – pure Z boson production has the most constant scaling ratio. No distinction was made between those charged final states which were positive and those

n	σ/pb
1	$1.5230(6){\times}10^{6}$
2	$1.3589(4){\times}10^{3}$
3	$4.736(2)$
4	$5.3582(1){\times}10^{-2}$
5	$1.460(3){\times}10^{-3}$

Table 7.4: This table shows the total cross-section for exclusive multiplicities, n, of gauge boson production at $100\,\mathrm{TeV}$ with a scale of $\sqrt{\hat{s}}$. The production range spans several orders of magnitude but even the smallest cross-section considered here would be within reach of a $100\,\mathrm{TeV}$ collider.

which were negative. The scaling behaviour of Z^n boson production being more staircase-like in scaling than any other weak boson process suggests that much of the non-constant behaviour of R comes from the weak boson self-interactions, for which there are none in Z^n production. These scaling behaviours can be seen in Fig. 7.5. This demonstrates how the scaling behaviour is more staircase-like for the individual weak boson multiplicities, shown on the right-hand plot of Fig. 7.5. Including mixed $W^{\pm}Z$ boson final states causes a steeper increase in the value of $R_{(n+1)/n}$ with n. The exact cause of this different scaling behaviour requires a more detailed study than is possible in this thesis.

Fig. 7.5 can be compared with the QCD scaling observed in Fig. 7.4. The scaling behaviour in Fig. 7.4 shows a Poisson scaling behaviour across all EW processes and for each jet cut considered. The trend in Fig. 7.5 shows the opposite behaviour, with the ratio increasing with increasing boson multiplicity. This difference between the weak and QCD interactions suggests the behaviour is linked to the longitudinal polarisation of the weak bosons.

7.4   Multi-Higgs Boson Production by WBF

The selection criteria and cuts used for the cross-sections in Fig. 7.6 are given in Tab. 7.5. The factorisation, μ_f, and renormalisation, μ_r, scales used for this process were

$$\mu_r = \mu_f = \sum_j p_{\perp,j} + N M_H \,, \qquad (7.3)$$
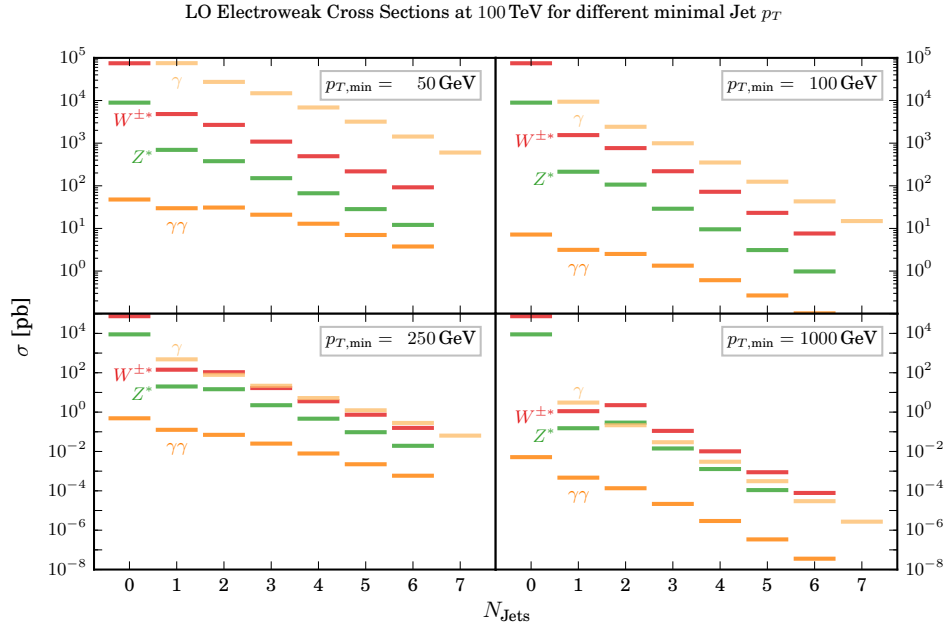
Figure 7.4: The scaling behaviour for EW processes with QCD radiation for different jet $p_\perp$ cuts. Figure prepared by Enrico Bothmann.
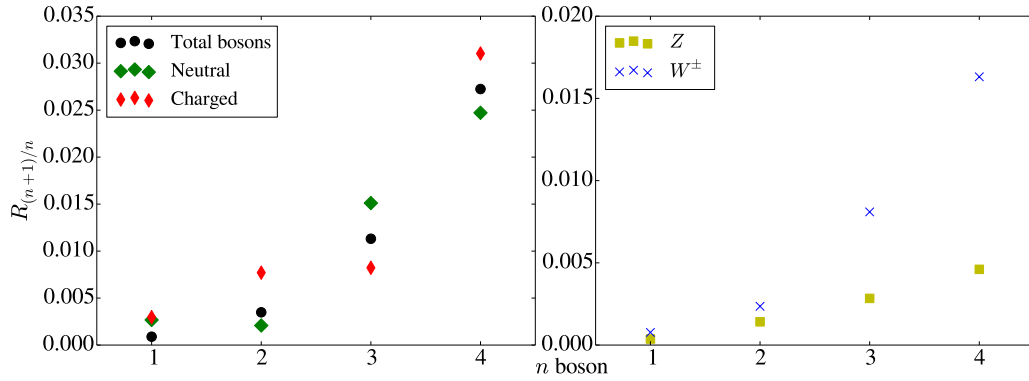

Figure 7.5: Left-hand-side shows the weak boson scaling, $R_{(n+1)/n}$, for the total weak boson multiplicity, charged and neutral final states and right-hand-side shows the scaling behaviour for $W^\pm$ and Z boson multiplicities separately.

Observable	Cut
$m_{j_1 j_2}$	1 TeV
$\Delta\eta_{j_1 j_2}$	5
$p_{\perp,j}$	50 GeV
ΔR	0.4
Jet Algorithm	anti-k_T

Table 7.5: Cuts on the jets for WBF total cross-sections. j denotes a jet, and j_i denotes the ith jet ordered in $p_\perp$. ΔR is the jet radius used in the jet finding algorithm.

where $p_{\perp,j}$ denotes the $p_\perp$ of final state parton j, M_H the mass of the Higgs boson and N the number of Higgs bosons produced.

The cross-sections at 100 TeV for multiple Higgs boson production via WBF are presented in Fig. 7.6. The calculations include the tri-linear and quartic Higgs boson couplings in the di-Higgs boson and tri-Higgs boson channels. The cross-sections fall off with increasing jet and Higgs boson multiplicity. Even at a 100 TeV collider, tri-Higgs boson production via WBF would be very rare, especially if any additional jets are included. It is therefore not possible to study the quartic Higgs boson couplings via WBF at a 100 TeV proton-proton collider, as Fig. 7.6 shows that the cross-section for this process is 20 ab.

However, di-Higgs boson production via WBF has a cross-section of 25 fb, which would allow for studies into the tri-linear Higgs boson coupling in the WBF production channel at 100 TeV.

The scaling behaviour of the different multiplicities of Higgs boson production at 100 TeV is shown in Fig. 7.6. This shows a constant scaling behaviour with jet multiplicity for 0, 1 and 2 Higgs boson being produced. Increasing the Higgs boson multiplicity decreases the production cross-section by a factor ~ 1000.

7.5 BSM Backgrounds

This section produces distributions of the H_T and $E_\perp^{\text{miss}}$ of events at a 100 TeV binned by lepton multiplicity as relevant background SM processes for BSM searches. These distributions have been produced at parton level with up to

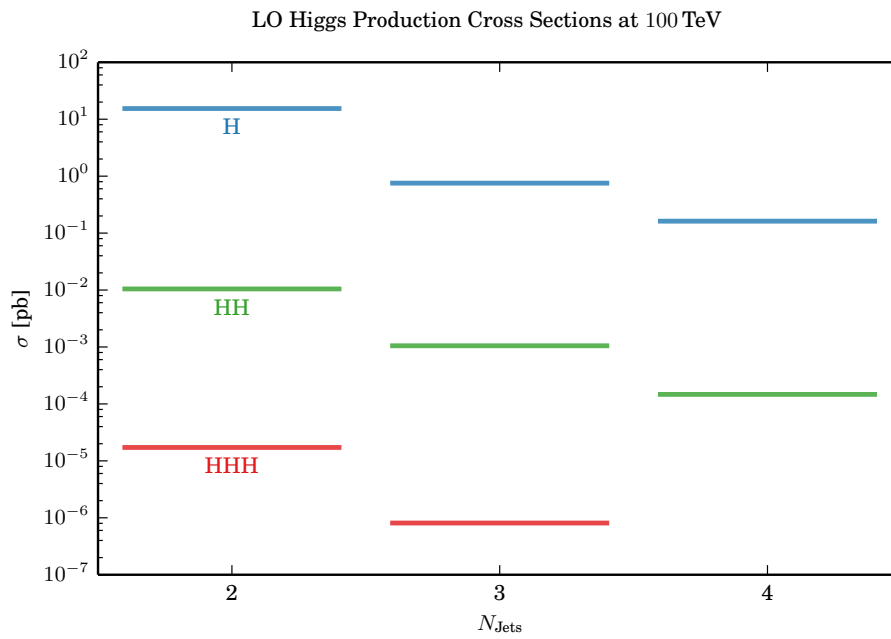**Figure 7.6:** WBF production cross-sections for single, double and triple Higgs boson production, with the two leading jets satisfying $m_{jj} > 1\,\text{TeV}$ and $\Delta\eta_{jj} > 5$ in conjunction with additional jets. For the jet definition and the scale choices see text.

2 additional jets merged in from the ME. These cover the most significant backgrounds to multi-lepton searches for BSM physics in the SM. The scale used in these processes was the CKKW scale as described in Ref. [117].

These figures demonstrate how the behaviour of the background processes differs over the distribution and how the dominant background processes vary depending on the number of final state leptons required. There is also a Z veto applied in the case of two final state leptons, and the effect implementing this veto has on the distributions is discussed. This veto applies to any event with a same flavour opposite sign lepton (SFOS) pair.

The analysis used in this section is the same as the ATLAS-inspired analysis for the 14 TeV BSM background study in Chap. 5. However, for this study the requirement that the number of final state leptons be exactly 3 is removed and events are binned into final state lepton multiplicity, of which distributions are presented for the exclusive 1, 2 and 3 final state lepton cases.

Figs. 7.7 and 7.8 show the contribution of multi-lepton SM final states to the H_T and $E_\perp^{\mathrm{miss}}$ distributions, respectively. In addition to the processes shown, single top and Higgs boson processes can contribute to multi-lepton final states.

The plots in Figs. 7.7 and 7.8 show the contributions binned by lepton multiplicity as:

- **top-left** 1 lepton

- **bottom-left** 2 leptons

- **top-left** 3 leptons

- **bottom-right** 2 leptons with SFOS veto

Figs. 7.7 and 7.8 demonstrate similar patterns. As such, the following provides a detailed discussion of Fig. 7.7 which can be largely extended to Fig. 7.8. The points specific to Fig. 7.7 are then made in a brief paragraph at the end of the section.

In Fig. 7.7, for the 1 lepton bin, top production and single boson production are the most dominant processes. $W^\pm$ boson production is predictably more

Figure 7.7: H_T of events binned by lepton multiplicity. The top plots shows the 1 and 3 lepton bins, and the lower plots show the 2 lepton multiplicity with(out) a Z boson veto on the right-(left-)hand-side.

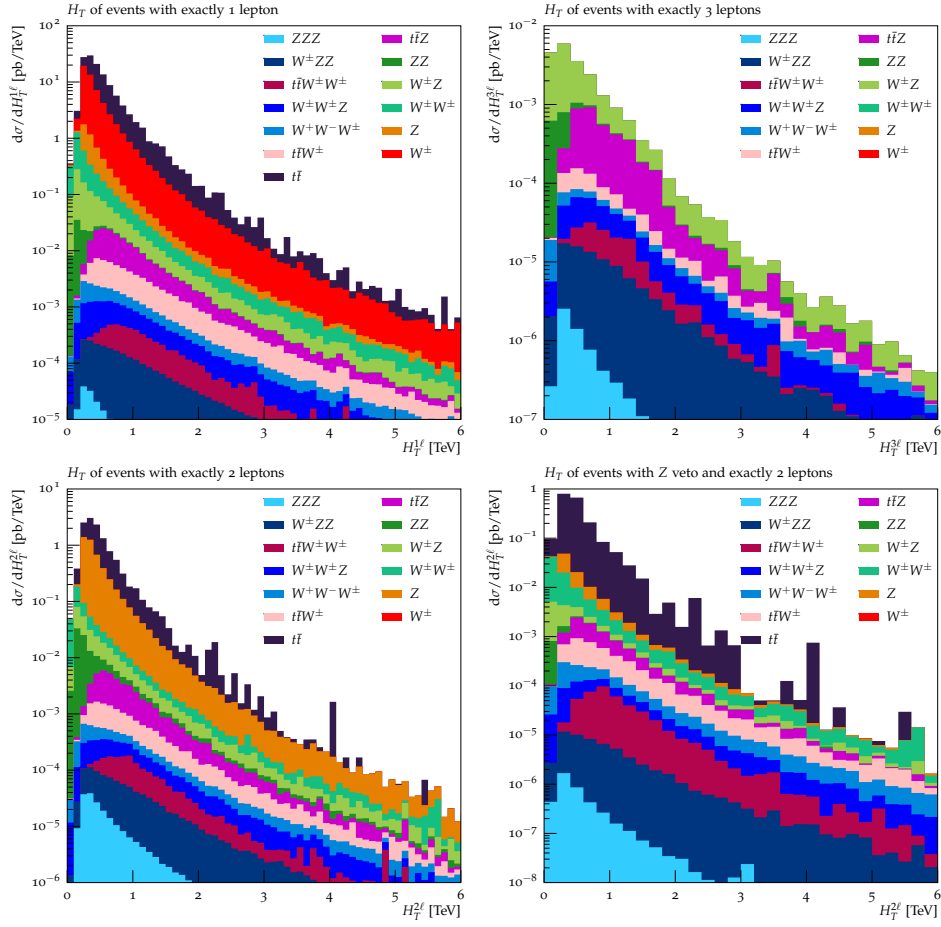**Figure 7.8:** $E_\perp^{\mathrm{miss}}$ of events binned by lepton multiplicity. The top plot shows the 1 and 3 lepton bins, and the lower plots show the 2 lepton multiplicity with(out) a Z boson veto on the right-(left-)hand-side.
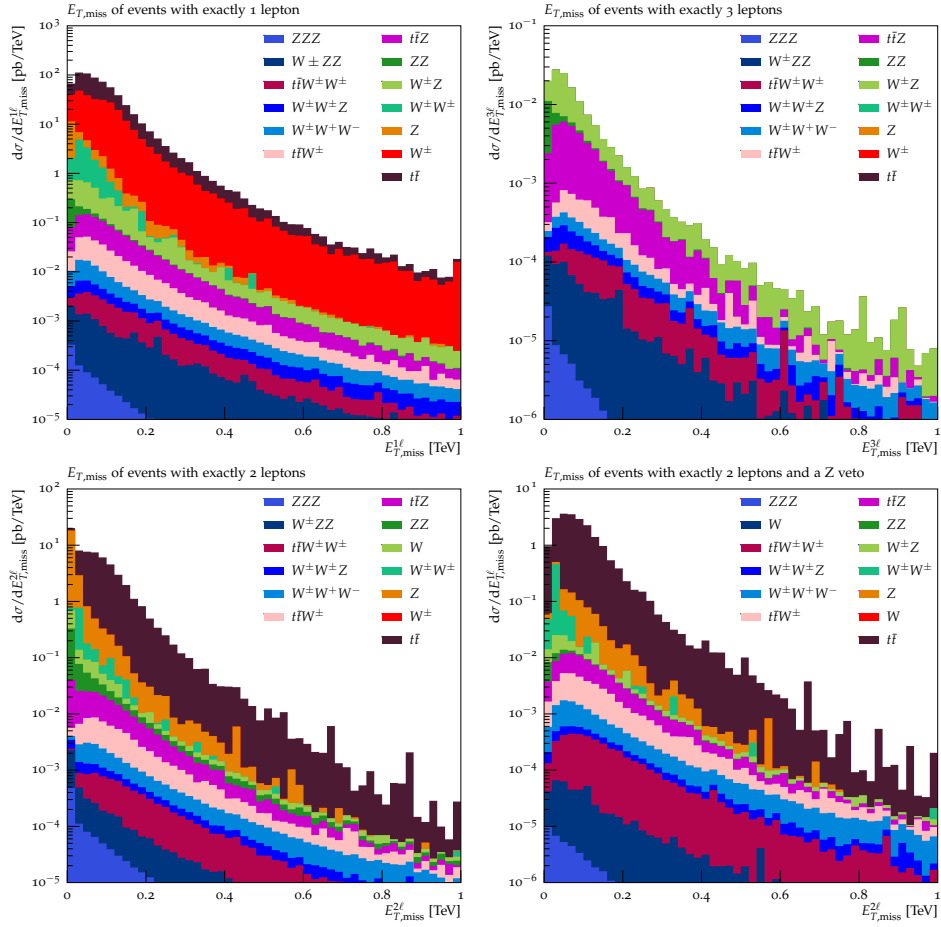
dominant than Z boson production. The contributions from $t\bar{t}$ and $W^{\pm}$ are approximately the same, with $W^{\pm}$ beginning to be more dominant in the high H_T region.

The cross-section for $W^{\pm}$ production disappears in the 2 lepton bin, and the contribution from $t\bar{t}$ is reduced by a factor of ~ 5. It is clear that $W^{\pm}$ production cannot contribute to the 2 lepton final state, and that the $t\bar{t}$ process is suppressed in the 2 lepton bin by the small $W^{\pm}$ branching ratio to leptons, which is $\sim \frac{1}{4}$, considering the further decays of any τ leptons. The contribution from the Z production, however, is very similar between the 1 lepton and 2 lepton bin. The Z boson decays to leptons relatively infrequently, and can contribute to the 1 lepton final state through the $\tau^{+}\tau^{-}$ channel. It is most significant, however, in the 2 lepton final state where it is comparable to $t\bar{t}$ production in the low H_T region and the dominant process in the high H_T tail.

The 3 lepton final state does not contain any contribution from the processes which have been dominant thus far. In this plot it is the di-boson contributions that are the most significant, with $W^{\pm}Z$ boson production most dominant. Whilst the contribution from $W^{\pm}Z$ is still suppressed compared to the lower lepton multiplicity plots, it is the most dominant process in the tri-lepton final state by an order of magnitude. It is clear that the overall contribution of all the SM processes in this tri-lepton final state is greatly suppressed compared to the previous plots. This is the reason that this channel is of more interest in searches for BSM physics than the lower multiplicity channels. Of the subleading processes in this channel, ZZ and $t\bar{t}Z$ are the most significant. ZZ is the dominant subleading contribution in the low H_T region and $t\bar{t}Z$ is the dominant subleading contribution at high H_T.

The remaining plot, the lower right-hand-side, includes the SFOS veto. The most significant impact of this veto is on the Z boson contribution, which is $\sim \frac{1}{20}$ of the cross-section from before the veto was applied. The $t\bar{t}$ contribution is not substantially affected, and as this was previously one of the 2 dominant processes, the overall contribution to the di-lepton final state from all considered processes is only reduced by about a factor of 3.

In all of the plots for H_T the $t\bar{t}V^{n}$ plots, where $n = 0, 1, 2$, show a peak at

higher H_T than the multiboson contributions.

Fig. 7.8 is the complementary distributions to Fig. 7.7. This shows the same processes as in Fig. 7.7 for the $E_\perp^{\mathrm{miss}}$ distribution. The same pattern of dominant processes is seen in Fig. 7.7 and Fig. 7.8. Here the SFOS veto eliminates the Z boson contribution in the lower end of the $E_\perp^{\mathrm{miss}}$ spectrum. However, the high energy tail of the Z boson process remains in similar proportion to the $t\bar{t}$ process. The most significant impact of the Z boson veto is on the ZZ boson process. The contribution, which is confined to the low $E_\perp^{\mathrm{miss}}$ region, is almost entirely eliminated by the Z boson veto. This reduction is a result of the forced τ decays of both Z bosons.

7.6 Conclusions

This chapter detailed the 100 TeV extension of SM processes with the SHERPA Monte Carlo event generator, and provides cross-section numbers for key processes and distributions for multi-lepton production.

The behaviour of multiple weak boson production was discussed, and the issue of SU(2) restoration was analysed at 100 TeV. While there was a tendency in the high weak boson limit for the SU(2) symmetry to be restored, there was still a preference for W^+ production over other weak bosons in a proton-proton collider with a multiplicity of up to 6 weak bosons. The scaling behaviour with weak boson radiation was also analysed as compared to QCD scaling behaviour in the high energy limit. For pure weak boson production, Z boson production displayed the most staircase-like scaling, however weak boson production, in general, does not demonstrate the same behaviours familiar from QCD. Instead, the ratio $R_{(n+1)/n}$ typically increases with increasing n. An approximate staircase scaling was also present in the $t\bar{t}V^n$ production for the sum of all possible V.

The effects of including one additional QCD radiation in $t\bar{t}V^n$ production demonstrates the dependence that cross-sections have on the $p_\perp$ cut of associated jets. The increased cross-section arising from the requirement of one QCD radiation is a result of the increased cross-section for quark-gluon interactions over either gluon-gluon or quark-quark interactions.

The final class of processes considered was multiple Higgs boson production via WBF. This is complementary to the multiple Higgs boson production via gluon fusion. The cross-sections show a staircase scaling behaviour with both the jet multiplicity and with Higgs boson multiplicity.

Finally, distributions were shown for general event observables demonstrating the behaviour of SM processes to multi-lepton events. The dominant processes in each lepton bin from 1 to 3 was shown, along with the effect of including a veto on all SFOS leptons.

Part IV

Conclusions

Chapter 8

Conclusions

The work in this thesis demonstrates the state-of-the art technology available within Monte Carlo event generators for particle physics processes. The move to NLO QCD ME calculations within the SHERPA software is detailed in Chap. 2, with a focus on the OPENLOOPS method, which is employed through the SHERPA + OPENLOOPS interface for this thesis. The OPEN-LOOPS formalism allows for fast and flexible calculations of NLO QCD cross-sections, and these results can be interfaced with the SHERPA parton shower with use of the S-MC@NLO variant of the MC@NLO matching method. Chap. 3 presents a proof-of-concept study for the SHERPA + OPENLOOPS interface in calculations of total cross-sections to NLO QCD accuracy. There is good agreement found between the SHERPA + OPENLOOPS interface and published MADGRAPH + aMC@NLO numbers.

NLO QCD merged samples, such as those prepared by using the MEPS@NLO procedure, are currently the state-of-the art for calculating differential cross-sections with Monte Carlo event generators. Improving the perturbative accuracy of the hard process can be achieved through NNLO QCD calculations, or the inclusion of NLO EW corrections. These are typically of a similar order of magnitude. Sudakov logarithms provide a high-energy approximation to NLO EW corrections, which is simple to include on top of NLO QCD calculations as it can be implemented as a K-factor. These logarithms allow for a very precise determination to be made in high-$p_\perp$ tails, where hints of heavy resonances are possible, as well as precise determination

of the angular distributions of particles in decay planes, again important in the search for new physics and heavy resonances. The implementation of this formalism within the SHERPA framework has been detailed in Chap. 4 along with validation plots, which find good agreement in the comparison of the SHERPA implementation with published numbers, and initial results.

This thesis also presented some phenomenological results, which made use of the technology validated in the first part of the thesis. The SHERPA + OPENLOOPS set-up was applied in Chap. 5 to important and challenging processes relevant to both Higgs physics and BSM searches. The processes considered were multiple weak boson production, with tri-lepton final states produced from the decays. The phenomenological studies presented were a Higgs boson study, and an application of the processes as SUSY backgrounds. In the first case, Higgs boson processes contribute significantly to the SM tri-lepton final state, via VH production, for $V = W^{\pm}Z$. This channel, therefore, is a useful probe of Higgs sector physics. These processes were calculated to MEPS@NLO accuracy, which provides a solid handle on the signal and backgrounds. In addition, the rarity of the tri-lepton final state in the SM makes this a very useful channel for SUSY searches. The same processes were considered in this context, along with $t\bar{t}V$. These processes were calculated to only S-MC@NLO accuracy, as the additional precision of the extra jets was not required by this analysis. It was shown that although $W^{\pm}Z$ provides the leading background, associated Higgs boson production contributes significantly to tri-lepton backgrounds to SUSY searches. It was also demonstrated that $t\bar{t}V$ production becomes most significant to these searches in the high-$p_{\perp}$ tails.

One top pair production process of interest is the $t\bar{t}HH$ process, where the Higgs can be produced via a direct coupling to a standard model fermion. This process was considered in Chap. 6 at LO accuracy along with all relevant backgrounds. The $t\bar{t}H(\to HH)$ process does not suffer the negative interference with the $t(\to tH)\bar{t}(\to \bar{t}H)$ process that occurs in many di-Higgs production channels, such as the main production channel, gluon fusion. The negative interference arises as a result of the triangle and box structures that exist in gluon fusion. The tree-like structure of $t\bar{t}HH$ production allows for the completely positive interference between production channels. This pro-

cess therefore provides a complementary search channel for non-SM tri-linear Higgs boson couplings, which is a key area for new physics to be observed. Using this channel, this thesis presented theoretical bounds on the allowed region for BSM physics in the tri-linear Higgs couplings.

The $t\bar{t}HH$ process can be studied at a 14 TeV LHC, although it does suffer from a low cross-section. It is therefore likely to still be of interest at a potential future 100 TeV collider. Physics at 100 TeV provides many new challenges and a far more active QCD environment, and the investigation of how to treat physics in this environment is still in the early stages. Chap. 7 provides a study of some EW processes at 100 TeV. This thesis presented LO merged predictions for processes with leptonic final states, binned by lepton multiplicity, at 100 TeV. It further presented the behaviour of multiple gauge boson production and plots have been presented to demonstrate a slow convergence towards the restoration of SU(2) invariance at high weak boson multiplicity. Cross-sections have also been presented for multiple Higgs boson production via WBF, and for the production of weak gauge bosons in association with a top pair. Additional QCD radiation was shown to be very common at a 100 TeV proton-proton collider, even for jet definitions of up to $p_{\perp,j} > 100$ GeV, for these processes. The scaling behaviour with respect to EW radiation was investigated, and compared to QCD scaling behaviour. The scaling with EW radiation was seen to typically have a different behaviour to traditional QCD patterns.

This thesis presented extensions of the SHERPA functionality which increase the available precision. The calculations at 14 TeV and 100 TeV were then completed to the highest possible precision with SHERPA and OPENLOOPS. The combination of higher order technologies presented in this thesis for QCD and EW corrections will provide an important insight into future measurements at high energy colliders.

Appendix A

SHERPA + OPENLOOPS Consistency Checks

In order to check agreement between SHERPA and OPENLOOPS on the values of the Born ME and the pole coefficient, the following settings were employed:

- OL_BORN_CHECK=1

- OL_POLE_CHECK=1

These settings output the ratio relative difference between the SHERPA and OPENLOOPS calculation. This ratio, R, and difference, D, are defined as

$$R = \frac{X_{\text{OL}}}{X_{\text{SHERPA}}} \tag{A.1}$$

$$D = \frac{X_{\text{SHERPA}} - X_{\text{OL}}}{X_{\text{SHERPA}}}, \tag{A.2}$$

where X_{Sherpa} and X_{OL} denote the value of X calculated by SHERPA and OPENLOOPS, respectively. X is B for OL_BORN_CHECK=1, and P_ϵ, P_{ϵ^2} in turn for OL_POLE_CHECK=1. In both of these cases, the calculation was considered to be in conflict for $D > 10^{-12}$. This procedure was automated with the use of a python script, and a results file was produced with any failing phase-space points.

Appendix B

EW Sudakov Look-Up Tables

This appendix provides the table of look-up values used for the coefficients to the logarithms for the K_{EW}^{LSC}, K_{EW}^{SSC} and K_{EW}^{C} components of K_{EW}, as defined in Chap. 4 as

$$K_{EW} = K_{EW}^{LSC} + K_{EW}^{SSC} + K_{EW}^{C} + K_{EW}^{PR}. \qquad (B.1)$$

K_{EW}^{LSC}, K_{EW}^{SSC} and K_{EW}^{C} contain a factorised numerical coefficient, Δ_{EW}, and a matrix element dependent structure. This appendix details the values used to determine Δ_{EW} for each flavour and helicity combination.

In this appendix, $\cos\theta_W$ and $\sin\theta_W$ of the weak mixing angle are denoted as c, s, respectively.

B.1 Coefficients for Leading Soft-Collinear Logarithms

This section provides the relevant coefficients for Δ_{EW}^{LSC} as defined in Chap. 4. This coefficient depends on the type of EW boson exchanged, and the flavour and chirality of the external particles. This is included in the EW Sudakov

l,σ	$\Delta_{\mathrm{LSC}}(i_l, W^{\pm})$	$\Delta_{\mathrm{LSC}}(i_l, Z)$	$\Delta_{\mathrm{LSC}}(i_l, \gamma)$
ν,L		$\frac{1}{8s^2c^2}$	0
ℓ,L	$\frac{1}{4s^2}$	$\frac{c^2-s^2}{8s^2c^2}$	$\frac{1}{2}$
u,L		$\frac{(3c^2-s^2)^2}{72s^2c^2}$	$\frac{2}{9}$
d,L		$\frac{(3c^2+s^2)^2}{72s^2c^2}$	$\frac{1}{18}$
ℓ,R		$\frac{s^2}{2c^2}$	$\frac{1}{2}$
u,R	0	$\frac{4s^2}{18c^2}$	$\frac{2}{9}$
d,R		$\frac{s^2}{18c^2}$	$\frac{1}{18}$
$W^{\pm}$,T	$\frac{1}{2s^2}$	$\frac{c^2}{2s^2}$	$\frac{1}{2}$
$Z(\to\gamma)$,T	$-\frac{c}{s}$		
$Z(\to Z)$,T	$\frac{c^2}{s^2}$	0	0
$\gamma(\to\gamma)$	1		
$\gamma(\to Z)$	$-\frac{c}{s}$		
H	$\frac{1}{s^2}$	$\frac{1}{8s^2c^2}$	0
Z,L			
W,L	$\frac{1}{s^2}$	$\frac{1}{8s^2c^2}$	0

Table B.1: This table shows the coefficients logarithms in the leading soft collinear piece. These are broken down into each EW particle, and the brackets indicate a mixing and therefore a new underlying Born term. In the leading case, these changes can only be caused by W boson exchange. L/R denotes the left/right handed helicities for fermions. For the massive bosons, T represents the transverse polarisation and L the longitudinal polarisation. The case for antiparticles is identical to that of the corresponding particle.

correction as

$$\delta\mathcal{M}_{\mathrm{EW}}^{\mathrm{LSC}\,i_1\ldots i_n} = -\frac{\alpha}{4\pi}\sum_l\sum_V \Delta_{\mathrm{LSC}}(i_l, V)\mathcal{M}_0^{i_1\ldots i_{l'}\ldots i_n} \times$$
$$\left[\log^2\left(\frac{\hat{s}}{M_W^2}\right) + 2\log\left(\frac{\hat{s}}{M_W^2}\right)\log\left(\frac{M_W^2}{M_V^2}\right)\right]. \tag{B.2}$$

Tab. B.1 presents the values of $\Delta_{\mathrm{LSC}}(i_l, V)$ for external lines i_l, with flavour l and helicity σ.

B.2 Coefficients for Subleading Soft-Collinear Logarithms

For the subleading logarithms, the look-up table must be used twice, once for each of the external particles involved in the EW boson exchange. The

l,σ	$\Delta_{\mathrm{SSC}}(i_l, W^\pm)$	$\Delta_{\mathrm{SSC}}(i_l, Z)$	$\Delta_{\mathrm{SSC}}(i_l, \gamma)$
$\nu_L(\overline{\nu}_L)$		$(-)\frac{1}{\sqrt{2}sc}$	0
$\ell^-(\ell^+),\mathrm{L(R)}$	$(-)\frac{1}{s}$	$(-)\frac{2s^2-1}{\sqrt{2}sc}$	$(-)\sqrt{2}$
$u(\overline{u}),\mathrm{L(R)}$		$(-)\sqrt{2}\frac{3-4s^2}{6sc}$	$(+)-2\frac{\sqrt{2}}{3}$
$d(\overline{d}),\mathrm{L(R)}$		$(-)\sqrt{2}\frac{2s^2-3}{6sc}$	$(-)\frac{\sqrt{2}}{3}$
$\ell^-(\ell^+),\mathrm{R(L)}$		$(-)\frac{\sqrt{2}s}{c}$	$(-)\sqrt{2}$
$u(\overline{u}),\mathrm{R(L)}$	0	$(+)-\sqrt{2}\frac{2s}{3c}$	$(+)-2\frac{\sqrt{2}}{3}$
$d(\overline{d}),\mathrm{R(L)}$		$(-)\sqrt{2}\frac{s}{3c}$	$(-)\frac{\sqrt{2}}{3}$
$W^\pm(Z)(W^\pm),\mathrm{T}$	$\mp\sqrt{2}\frac{c}{s}$	$\pm\sqrt{2}\frac{1-s^2}{sc}$	$\mp\sqrt{2}$
$W^\pm(\gamma)(-),\mathrm{T}$	$\pm\sqrt{2}$	$-$	$-$
$Z(W^\pm),\mathrm{T}$	$\mp\sqrt{2}\frac{c}{s}$	0	0
$\gamma(W^\pm)$	$\pm\sqrt{2}$	0	0
$H(W^\pm)(Z),\mathrm{L}$	$\pm\frac{1}{\sqrt{2}s}$	$-\frac{1}{\sqrt{2}sc}$	
$Z(W^\pm)(H),\mathrm{L}$	$-\frac{1}{\sqrt{2}s}$	$\frac{1}{\sqrt{2}sc}$	0
$WL^\pm(H)(W^\pm),\mathrm{L}$	$\mp\frac{1}{\sqrt{2}s}$	$\pm\frac{1-2s^2}{\sqrt{2}sc}$	$\mp\sqrt{2}$
$W^\pm(Z)(-),\mathrm{L}$	$\frac{1}{\sqrt{2}s}$	$-$	$-$

Table B.2: This table shows the coefficients logarithms in the subleading soft collinear piece. These are broken down into each EW particle. For the fermions, where the EW partner is unique, the brackets show the behaviour of the anti-particle. However, for the EW bosons the first bracket indicates the EW partner in the case of W boson emission, and the second bracket (if this exists) shows the partner in the case of Z boson emission. L/R denotes left- and right-handed for fermions, and L/T denotes longitudinal and transverse polarisations for vector bosons.

coefficients are then included in the EW Sudakov approximation as

$$\delta\mathcal{M}_{\mathrm{EW}}^{\mathrm{SSC}i_1\ldots i_n} = \frac{\alpha}{4\pi}\sum_l\sum_{k<l}\sum_V \Delta_{\mathrm{SSC}}(i_l, V)\Delta_{\mathrm{SSC}}(i_k, \overline{V})\mathcal{M}_0^{i_1\ldots i_{l'}\ldots i_{k'}\ldots i_n}\times$$
$$\log\left(\frac{\hat{s}}{M_W^2}\right)\log\left(\frac{|(p_l+p_k)^2|}{\hat{s}}\right). \tag{B.3}$$

Tab. B.2 lists the values for $\Delta_{\mathrm{SSC}}(i_l, V)$ for external line i_l with flavour l and helicity σ.

j,σ	$\Delta_{\mathrm{C}}(i_j)$
ν,L	$3\frac{s^2+3c^2}{8c^2s^2}$
ℓ,L	$3\frac{s^2+3c^2}{8c^2s^2}$
ℓ,R	$\frac{3}{2c^2}$
u,L	$\frac{9s^2+3c^2}{24c^2s^2} - \frac{m_d^2}{8s^2M_W^2}$
d,L	$\frac{9s^2+3c^2}{24c^2s^2} - \frac{m_u^2}{8s^2M_W^2}$
u,R	$\frac{2}{3c^2} - \frac{m_u^2}{4s^2M_W^2}$
d,R	$\frac{1}{6c^2} - \frac{m_d^2}{4s^2M_W^2}$
$W^\pm$,T	$\frac{19}{12s^2}$
$Z(\to Z)$,T	$\frac{19-38s^2-22s^4}{12s^2c^2}$
$Z(\to \gamma)$,T	$-\frac{19+22s^2}{6sc}$
γ	$-\frac{11}{6}$
H	
Z,L	$\frac{1+2c^2}{s^2c^2} - \frac{N_C^t m_t^2}{4s^2M_W^2}$
$W^\pm$,L	

Table B.3: The coefficients for the logarithms in the single collinear case. N_C^f is the colour factor associated with fermion f. L/R represent the left and right handed polarisations for fermions, and L/T represent the longitudinal and transverse polarisations of massive gauge bosons. The masses of the light quarks and all generations of leptons are ignored.

B.3 Coefficients for Single Collinear Logarithms

In analogy to the previous two sections which document the coefficients for the soft-collinear limit, $\mathrm{K}_{\mathrm{EW}}^{\mathrm{C}}$ can be factorised as

$$\mathrm{K}_{\mathrm{EW}}^{\mathrm{C}} = \frac{\alpha}{4\pi} \sum_V \sum_j \Delta_{\mathrm{C}}(i_j, V) \frac{2\Re[\mathcal{M}_{\mathrm{LO}}^* \mathcal{M}_0^{i_1...i_j'...i_n}]}{|\mathcal{M}_{\mathrm{LO}}|^2} L_W(\hat{s}) \,. \tag{B.4}$$

Tab. B.3 lists $\Delta_{\mathrm{C}}(i_j, V)$ for external line i_j with flavour j and helicity σ.

Appendix C

Plotting Tools

The plots in this thesis are produced mostly using the Rivet [248] package, and the Feynman diagrams produces with JaxoDraw [249]. However, the following plots were produced with matplotlib [250]:

- Figs. 3.1 and 3.2.

- Figs. 4.6 and 4.7.

- Fig. 6.2.

- Figs. 7.2, 7.3 and 7.5.

Further to these exceptions, Fig. 7.4 was prepared by Enrico Bothmann. Enrico Bothmann also plotted Fig. 7.6, although the cross-sections displayed in this figure were prepared by the author of this thesis. Both Figs. 7.4 and 7.6 make use of matplotlib.

Bibliography

[1] G. Aad et al., ATLAS, *Observation of a new particle in the search for the Standard Model Higgs boson with the ATLAS detector at the LHC*, Physics Letters **B716** (2012), no. 1, 1 – 29.

[2] S. Chatrchyan et al., CMS, *Observation of a new boson at a mass of 125 GeV with the CMS experiment at the LHC*, Physics Letters **B716** (2012), no. 1, 30 – 61.

[3] F. Englert and R. Brout, *Broken Symmetry and the Mass of Gauge Vector Mesons*, Phys. Rev. Lett. **13** (1964), 321–323.

[4] P. Higgs, *Broken symmetries, massless particles and gauge fields* , Physics Letters **12** (1964), no. 2, 132 – 133.

[5] P. W. Higgs, *Broken Symmetries and the Masses of Gauge Bosons*, Phys. Rev. Lett. **13** (1964), 508–509.

[6] G. S. Guralnik, C. R. Hagen and T. W. B. Kibble, *Global Conservation Laws and Massless Particles*, Phys. Rev. Lett. **13** (1964), 585–587.

[7] P. W. Higgs, *Spontaneous Symmetry Breakdown without Massless Bosons*, Phys. Rev. **145** (1966), 1156–1163.

[8] T. W. B. Kibble, *Symmetry Breaking in Non-Abelian Gauge Theories*, Phys. Rev. **155** (1967), 1554–1561.

[9] S. Chatrchyan et al., The CMS Collaboration, *Evidence for the 125 GeV Higgs boson decaying to a pair of τ leptons*, Journal of High Energy Physics **2014** (2014), no. 5, , (English).

[10] S. Chatrchyan et al., CMS, *Evidence for the direct decay of the 125 GeV Higgs boson to fermions*, Nature Physics **10** (2014), 557 – 560.

[11] G. Aad et al., ATLAS, *Evidence for the Higgs-boson Yukawa coupling to tau leptons with the ATLAS detector*, Journal of High Energy Physics **1504** (2015), 117, [arXiv:1501.04943 [hep-ex]].

[12] G. Aad et al., ATLAS, *Measurements of Higgs boson production and couplings in diboson final states with the ATLAS detector at the LHC*, Physics Letters **B726** (2013), 88 – 119.

[13] S. Chatrchyan et al., CMS, *Measurement of Higgs boson production and properties in the WW decay channel with leptonic final states*, Journal of High Energy Physics **2014** (2014), no. 1, , (English).

[14] S. Chatrchyan et al., CMS, *Measurement of the properties of a Higgs boson in the four-lepton final state*, Phys. Rev. **D89** (2014), 092007.

[15] S. Chatrchyan et al., CMS, *Study of the Mass and Spin-Parity of the Higgs Boson Candidate via Its Decays to Z Boson Pairs*, Phys. Rev. Lett. **110** (2013), 081803.

[16] G. Aad et al., ATLAS, *Evidence for the spin-0 nature of the Higgs boson using ATLAS data*, Physics Letters **B726** (2013), 120 – 144.

[17] A. Avetisyan, J. M. Campbell, T. Cohen, N. Dhingra, J. Hirschauer et al., *Methods and Results for Standard Model Event Generation at $\sqrt{s} = 14$ TeV, 33 TeV and 100 TeV Proton Colliders (A Snowmass Whitepaper)*, arXiv:1308.1636 [hep-ex].

[18] A. Buckley et al., *General-purpose event generators for LHC physics*, Phys. Rept. **504** (2011), 145–233, [arXiv:1101.2599 [hep-ph]].

[19] T. Gleisberg, S. Höche, F. Krauss, A. Schälicke, S. Schumann and J. Winter, *Sherpa 1.α, a proof-of-concept version*, Journal of High Energy Physics **02** (2004), 056, [hep-ph/0311263].

[20] T. Gleisberg, S. Höche, F. Krauss, M. Schönherr, S. Schumann, F. Siegert and J. Winter, *Event generation with Sherpa 1.1*, Journal of High Energy Physics **02** (2009), 007, [arXiv:0811.4622 [hep-ph]].

[21] B. Andersson, G. Gustafson, G. Ingelman and T. Sjstrand, *Parton fragmentation and string dynamics*, Physics Reports **97** (1983), no. 23, 31 – 145.

[22] B. Andersson, *The Lund Model*, Cambridge University Press, 1998, Cambridge Books Online.

[23] D. Amati and G. Veneziano, *Preconfinement as a property of perturbative QCD*, Physics Letters B **83** (1979), no. 1, 87 – 92.

[24] K. A. Olive et al., Particle Data Group, *Review of Particle Physics*, Chin. Phys. **C38** (2014), 090001.

[25] *The infrared divergence phenomena and high energy processes: D. R. Yennie, S. C. Frautschi and H. Suura*, Annals of Physics **13** (1961), no. 2, 309 – 310.

[26] A. G.-D. Ridder, T. Gehrmann, E. Glover and J. Pires, *Second order QCD corrections to jet production at hadron colliders: the all-gluon contribution*, Phys.Rev.Lett. **110** (2013), no. 16, 162003, [`arXiv:1301.7310` [hep-ph]].

[27] R. Boughezal, F. Caola, K. Melnikov, F. Petriello and M. Schulze, *Higgs boson production in association with a jet at next-to-next-to-leading order in perturbative QCD*, Journal of High Energy Physics **1306** (2013), 072, [`arXiv:1302.6216` [hep-ph]].

[28] M. Czakon, P. Fiedler and A. Mitov, *Total Top-Quark Pair-Production Cross Section at Hadron Colliders Through $O(\alpha_S^4)$*, Phys.Rev.Lett. **110** (2013), 252004, [`arXiv:1303.6254` [hep-ph]].

[29] J. Currie, A. G.-D. Ridder, E. Glover and J. Pires, *NNLO QCD corrections to jet production at hadron colliders from gluon scattering*, Journal of High Energy Physics **1401** (2014), 110, [`arXiv:1310.3993` [hep-ph]].

[30] L.-S. Ling, R.-Y. Zhang, W.-G. Ma, L. Gan, W.-H. Li et al., *NNLO QCD corrections to Higgs pair production via vector boson*

fusion at hadron colliders, Phys.Rev. **D89** (2014), no. 7, 073001, [`arXiv:1401.7754` [hep-ph]].

[31] L. Wei-Hua, Z. Ren-You, M. Wen-Gan, G. Lei, L. Liu-Sheng et al., *Next-to-next-to-leading order QCD corrections to light Higgs pair production via vector boson fusion in the type II two-Higgs-doublet model*, Phys.Rev. **D89** (2014), no. 7, 075011, [`arXiv:1403.2782` [hep-ph]].

[32] M. Brucherseifer, F. Caola and K. Melnikov, *On the NNLO QCD corrections to single-top production at the LHC*, Phys.Lett. **B736** (2014), 58–63, [`arXiv:1404.7116` [hep-ph]].

[33] F. Cascioli, T. Gehrmann, M. Grazzini, S. Kallweit, P. Maierhöfer et al., *ZZ production at hadron colliders in NNLO QCD*, Phys.Lett. **B735** (2014), 311–313, [`arXiv:1405.2219` [hep-ph]].

[34] J. Gao and H. X. Zhu, *Electroweak prodution of top-quark pairs in e^+e^- annihilation at NNLO in QCD: the vector contributions*, Phys.Rev. **D90** (2014), no. 11, 114022, [`arXiv:1408.5150` [hep-ph]].

[35] J. Pires, *Precise QCD predictions for jet production at the LHC*, EPJ Web Conf. **90** (2015), 07005, [`arXiv:1412.3427` [hep-ph]].

[36] Vittorio Del Duca and Claude Duhr and Gábor Somogyi and Francesco Tramontano and Zoltán Trócsányi, *Higgs boson decay into b-quarks at NNLO accuracy*, Journal of High Energy Physics **1504** (2015), 036, [`arXiv:1501.07226` [hep-ph]].

[37] C. Anastasiou, J. Cancino, F. Chavez, C. Duhr, A. Lazopoulos et al., *NNLO QCD corrections to $pp \to \gamma^*\gamma^*$ in the large N_F limit*, Journal of High Energy Physics **1502** (2015), 182, [`arXiv:1408.4546` [hep-ph]].

[38] W. Hollik, M. Kollar and M. K. Trenkel, *Hadronic production of top-squark pairs with electroweak NLO contributions*, Journal of High Energy Physics **0802** (2008), 018, [`arXiv:0712.0287` [hep-ph]].

[39] S. Mao, M. Wen-Gan, Z. Ren-You, G. Lei and W. Shao-Ming, *Precise predictions for the Higgs production in association with a W-boson pair*

at ILC, Eur.Phys.J. **C59** (2009), 761–768, [`arXiv:0808.3018` [hep-ph]].

[40] Dao Thi Nhung and Le Duc Ninh and Marcus M. Weber, *NLO corrections to WWZ production at the LHC*, Journal of High Energy Physics **1312** (2013), 096, [`arXiv:1307.7403` [hep-ph]].

[41] Y. Zhang, W.-G. Ma, R.-Y. Zhang, C. Chen and L. Guo, *QCD NLO and EW NLO corrections to $t\bar{t}H$ production with top quark decays at hadron collider*, Phys.Lett. **B738** (2014), 1–5, [`arXiv:1407.1110` [hep-ph]].

[42] Stefan Höche and Ye Li and Stefan Prestel, *Higgs-boson production through gluon fusion at NNLO QCD with parton showers*, Phys.Rev. **D90** (2014), no. 5, 054011, [`arXiv:1407.3773` [hep-ph]].

[43] G. Ferrera, M. Grazzini and F. Tramontano, *Associated ZH production at hadron colliders: the fully differential NNLO QCD calculation*, Phys.Lett. **B740** (2015), 51–55, [`arXiv:1407.4747` [hep-ph]].

[44] Stefan Höche and Ye Li and Stefan Prestel, *Drell-Yan lepton pair production at NNLO QCD with parton showers*, Phys.Rev. **D91** (2015), no. 7, 074015, [`arXiv:1405.3607` [hep-ph]].

[45] C. Bernaciak and D. Wackeroth, *Combining NLO QCD and Electroweak Radiative Corrections to W boson Production at Hadron Colliders in the POWHEG Framework*, Phys.Rev. **D85** (2012), 093003, [`arXiv:1201.4804` [hep-ph]].

[46] P. Richardson, R. R. Sadykov, A. A. Sapronov, M. H. Seymour and P. Z. Skands, *QCD parton showers and NLO EW corrections to Drell-Yan*, Journal of High Energy Physics **1206** (2012), 090, [`arXiv:1011.5444` [hep-ph]].

[47] Stefan Kallweit and Jonas M. Lindert and Philipp Maierhöfer and Stefano Pozzorini and Marek Schönherr, *NLO electroweak automation and precise predictions for W+multijet production at the LHC*, Journal of High Energy Physics **1504** (2015), 012, [`arXiv:1412.5157` [hep-ph]].

[48] A. Denner and S. Pozzorini, *One loop leading logarithms in electroweak radiative corrections. 1. Results*, Eur.Phys.J. **C18** (2001), 461–480, [`arXiv:hep-ph/0010201` [hep-ph]].

[49] A. Denner and S. Pozzorini, *One loop leading logarithms in electroweak radiative corrections. 2. Factorization of collinear singularities*, Eur.Phys.J. **C21** (2001), 63–79, [`arXiv:hep-ph/0104127` [hep-ph]].

[50] E. Accomando, A. Denner and S. Pozzorini, *Electroweak correction effects in gauge boson pair production at the CERN LHC*, Phys.Rev. **D65** (2002), 073003, [`arXiv:hep-ph/0110114` [hep-ph]].

[51] A. Denner, M. Melles and S. Pozzorini, *Two loop electroweak corrections at high-energies*, Nucl.Phys.Proc.Suppl. **116** (2003), 18–22, [`arXiv:hep-ph/0211196` [hep-ph]].

[52] A. Denner, M. Melles and S. Pozzorini, *Two loop electroweak angular dependent logarithms at high-energies*, Nucl.Phys. **B662** (2003), 299–333, [`arXiv:hep-ph/0301241` [hep-ph]].

[53] A. Denner and S. Pozzorini, *An Algorithm for the high-energy expansion of multi-loop diagrams to next-to-leading logarithmic accuracy*, Nucl.Phys. **B717** (2005), 48–85, [`arXiv:hep-ph/0408068` [hep-ph]].

[54] A. Denner, B. Jantzen and S. Pozzorini, *Two-loop electroweak next-to-leading logarithmic corrections to massless fermionic processes*, Nucl.Phys. **B761** (2007), 1–62, [`arXiv:hep-ph/0608326` [hep-ph]].

[55] E. Accomando, A. Denner and S. Pozzorini, *Logarithmic electroweak corrections to $e^+e^- \to \nu_e\bar{\nu}_e W^+W^-$*, Journal of High Energy Physics **0703** (2007), 078, [`arXiv:hep-ph/0611289` [hep-ph]].

[56] A. Denner, B. Jantzen and S. Pozzorini, *Two-loop electroweak Sudakov logarithms for massive fermion scattering*, PoS **RADCOR2007** (2007), 002, [`arXiv:0801.2647` [hep-ph]].

[57] A. Denner, B. Jantzen and S. Pozzorini, *Two-loop electroweak next-to-leading logarithms for processes involving heavy quarks*, Journal of High Energy Physics **0811** (2008), 062, [`arXiv:0809.0800` [hep-ph]].

[58] A. V. Manohar and M. Trott, *Electroweak Sudakov Corrections and the Top Quark Forward-Backward Asymmetry*, Phys.Lett. **B711** (2012), 313–316, [`arXiv:1201.3926` [hep-ph]].

[59] M. Chiesa, G. Montagna, L. Barzò, M. Moretti, O. Nicrosini et al., *Electroweak Sudakov Corrections to New Physics Searches at the LHC*, Phys.Rev.Lett. **111** (2013), no. 12, 121801, [`arXiv:1305.6837` [hep-ph]].

[60] M. Ciafaloni, P. Ciafaloni and D. Comelli, *Bloch-Nordsieck violating electroweak corrections to inclusive TeV scale hard processes*, Phys.Rev.Lett. **84** (2000), 4810–4813, [`arXiv:hep-ph/0001142` [hep-ph]].

[61] F. Bloch and A. Nordsieck, *Note on the Radiation Field of the Electron*, Phys. Rev. **52** (1937), 54–59.

[62] T. Kinoshita, *Mass Singularities of Feynman Amplitudes*, Journal of Mathematical Physics **3** (1962), no. 4

[63] T. D. Lee and M. Nauenberg, *Degenerate Systems and Mass Singularities*, Phys. Rev. **133** (1964), B1549–B1562.

[64] T. Gleisberg and S. Höche, *Comix, a new matrix element generator*, Journal of High Energy Physics **0812** (2008), 039, [`arXiv:0808.3674` [hep-ph]].

[65] T. Gleisberg and F. Krauss, *Automating dipole subtraction for QCD NLO calculations*, Eur. Phys. J. **C53** (2008), 501–523, [`arXiv:0709.2881` [hep-ph]].

[66] F. Cascioli, P. Maierhöfer and S. Pozzorini, *Scattering Amplitudes with Open Loops*, Phys.Rev.Lett. **108** (2012), 111601, [`arXiv:1111.5206` [hep-ph]].

[67] A. Denner, S. Dittmaier and L. Hofer, *COLLIER - A fortran-library for one-loop integrals*, PoS **LL2014** (2014), 071, [`arXiv:1407.0087` [hep-ph]].

[68] M. Guzzi, P. Nadolsky, E. Berger, H.-L. Lai, F. Olness and C.-P. Yuan, *CT10 parton distributions and other developments in the global QCD analysis*, `arXiv:1101.0561` [hep-ph].

[69] S. Chatrchyan et al., CMS, *Search for electroweak production of charginos and neutralinos using leptonic final states in pp collisions at $\sqrt{s} = 7$ TeV*, Journal of High Energy Physics **1211** (2012), 147, [`arXiv:1209.6620` [hep-ex]].

[70] G. Aad et al., ATLAS, *Search for supersymmetry in events with three leptons and missing transverse momentum in $\sqrt{s} = 7$ TeV pp collisions with the ATLAS detector*, Phys.Rev.Lett. **108** (2012), 261804, [`arXiv:1204.5638` [hep-ex]].

[71] G. Aad et al., ATLAS, *Search for direct production of charginos and neutralinos in events with three leptons and missing transverse momentum in $\sqrt{s} = 7$ TeV pp collisions with the ATLAS detector*, Phys.Lett. **B718** (2013), 841–859, [`arXiv:1208.3144` [hep-ex]].

[72] G. Aad et al., ATLAS, *Search for direct slepton and gaugino production in final states with two leptons and missing transverse momentum with the ATLAS detector in pp collisions at $\sqrt{s} = 7$ TeV*, Phys.Lett. **B718** (2013), 879–901, [`arXiv:1208.2884` [hep-ex]].

[73] G. Aad et al., ATLAS, *Search for direct production of charginos and neutralinos in events with three leptons and missing transverse momentum in $\sqrt{s} = 8$TeV pp collisions with the ATLAS detector*, Journal of High Energy Physics **1404** (2014), 169, [`arXiv:1402.7029` [hep-ex]].

[74] V. Khachatryan et al., CMS, *Searches for electroweak production of charginos, neutralinos, and sleptons decaying to leptons and W, Z, and Higgs bosons in pp collisions at 8 TeV*, Eur.Phys.J. **C74** (2014), no. 9, 3036, [`arXiv:1405.7570` [hep-ex]].

[75] R. Frederix, S. Frixione, V. Hirschi, F. Maltoni, O. Mattelaer, P. Torrielli, E. Vryonidou and M. Zaro, *Higgs pair production at the LHC with NLO and parton-shower effects* , Physics Letters **B732** (2014), 142 – 149.

[76] M. E. Pestkin and D. V. Schröder, *An Introduction to Quantum Field Theory*, Westview Press, 1995.

[77] S. Catani and M. H. Seymour, *A General algorithm for calculating jet cross-sections in NLO QCD*, Nucl.Phys. **B485** (1997), 291–419, [`arXiv:hep-ph/9605323` [hep-ph]].

[78] G. Bevilacqua, M. Czakon, M. Kubocz and M. Worek, *Complete Nagy-Soper subtraction for next-to-leading order calculations in QCD*, Journal of High Energy Physics **1310** (2013), 204, [`arXiv:1308.5605` [hep-ph]].

[79] M. Bach, C. H. Chung and T. Robens, *An alternative subtraction scheme for NLO QCD calculations using Nagy-Soper dipoles*, PoS **RADCOR2013** (2013), 014, [`arXiv:1311.5773` [hep-ph]].

[80] R. Frederix, S. Frixione, F. Maltoni and T. Stelzer, *Automation of next-to-leading order computations in QCD: The FKS subtraction*, Journal of High Energy Physics **0910** (2009), 003, [`arXiv:0908.4272` [hep-ph]].

[81] J. M. Campbell, M. A. Cullen and E. N. Glover, *Four jet event shapes in electron - positron annihilation*, Eur.Phys.J. **C9** (1999), 245–265, [`arXiv:hep-ph/9809429` [hep-ph]].

[82] D. A. Kosower, *Antenna factorization in strongly ordered limits*, Phys.Rev. **D71** (2005), 045016, [`arXiv:hep-ph/0311272` [hep-ph]].

[83] G. Ossola, C. G. Papadopoulos and R. Pittau, *Reducing full one-loop amplitudes to scalar integrals at the integrand level*, Nucl.Phys. **B763** (2007), 147–169, [`arXiv:hep-ph/0609007` [hep-ph]].

[84] A. Denner and S. Dittmaier, *Reduction of one-loop tensor 5-point integrals*, Nucl. Phys. **B658** (2003), 175–202, [`hep-ph/0212259`].

[85] A. Denner and S. Dittmaier, *Reduction schemes for one-loop tensor integrals*, Nucl. Phys. **B734** (2006), 62–115, [`arXiv:hep-ph/0509141` [hep-ph]].

[86] A. Denner and S. Dittmaier, *Scalar one-loop 4-point integrals*, Nucl. Phys. **B844** (2011), 199–242, [`arXiv:1005.2076` [hep-ph]].

[87] G. Ossola, C. G. Papadopoulos and R. Pittau, *CutTools: A Program implementing the OPP reduction method to compute one-loop amplitudes*, JHEP **0803** (2008), 042, [`arXiv:0711.3596` [hep-ph]].

[88] A. van Hameren, *OneLOop: For the evaluation of one-loop scalar functions*, Comput.Phys.Commun. **182** (2011), 2427–2438, [`arXiv:1007.4716` [hep-ph]].

[89] J. Alwall, R. Frederix, S. Frixione, V. Hirschi, F. Maltoni et al., *The automated computation of tree-level and next-to-leading order differential cross sections, and their matching to parton shower simulations*, Journal of High Energy Physics **1407** (2014), 079, [`arXiv:1405.0301` [hep-ph]].

[90] T. Sjöstrand, S. Ask, J. R. Christiansen, R. Corke, N. Desai et al., *An Introduction to PYTHIA 8.2*, Comput.Phys.Commun. **191** (2015), 159–177, [`arXiv:1410.3012` [hep-ph]].

[91] M. Bahr, S. Gieseke, M. A. Gigg, D. Grellscheid, K. Hamilton et al., *Herwig++ Physics and Manual*, Eur.Phys.J. **C58** (2008), 639–707, [`arXiv:0803.0883` [hep-ph]].

[92] J. Bellm, S. Gieseke, D. Grellscheid, A. Papaefstathiou, S. Plätzer et al., *Herwig++ 2.7 Release Note*, `arXiv:1310.6877` [hep-ph].

[93] L. Lönnblad, *Ariadne version 4 A program for simulation of QDC cascades implementing the colour dipole model*, Comput. phys. commun. **71** (1992), 15–31.

[94] M. Moretti, T. Ohl and J. Reuter, *O'Mega: An Optimizing matrix element generator*, `arXiv:hep-ph/0102195` [hep-ph].

[95] W. Kilian, T. Ohl and J. Reuter, *WHIZARD: Simulating Multi-Particle Processes at LHC and ILC*, Eur.Phys.J. **C71** (2011), 1742, [`arXiv:0708.4233` [hep-ph]].

[96] F. Caravaglios, M. L. Mangano, M. Moretti and R. Pittau, *A New approach to multijet calculations in hadron collisions*, Nucl.Phys. **B539** (1999), 215–232, [`arXiv:hep-ph/9807570` [hep-ph]].

[97] M. L. Mangano, M. Moretti and R. Pittau, *Multijet matrix elements and shower evolution in hadronic collisions: $W b\bar{b}$ + n jets as a case study*, Nucl.Phys. **B632** (2002), 343–362, [arXiv:hep-ph/0108069 [hep-ph]].

[98] M. L. Mangano, M. Moretti, F. Piccinini, R. Pittau and A. D. Polosa, *ALPGEN, a generator for hard multiparton processes in hadronic collisions*, Journal of High Energy Physics **0307** (2003), 001, [arXiv:hep-ph/0206293 [hep-ph]].

[99] A. Kanaki and C. G. Papadopoulos, *HELAC: A Package to compute electroweak helicity amplitudes*, Comput.Phys.Commun. **132** (2000), 306–315, [arXiv:hep-ph/0002082 [hep-ph]].

[100] C. G. Papadopoulos and M. Worek, *Multi-parton cross sections at hadron colliders*, Eur.Phys.J. **C50** (2007), 843–856, [arXiv:hep-ph/0512150 [hep-ph]].

[101] G. Cullen, N. Greiner, G. Heinrich, G. Luisoni, P. Mastrolia et al., *Automated One-Loop Calculations with GoSam*, Eur.Phys.J. **C72** (2012), no. 3, 1889, [arXiv:1111.2034 [hep-ph]].

[102] G. Cullen, H. van Deurzen, N. Greiner, G. Heinrich, G. Luisoni et al., *GOSAM-2.0: a tool for automated one-loop calculations within the Standard Model and beyond*, Eur.Phys.J. **C74** (2014), no. 8, 3001, [arXiv:1404.7096 [hep-ph]].

[103] S. Badger, B. Biedermann and P. Uwer, *NGluon: A Package to Calculate One-loop Multi-gluon Amplitudes*, Comput.Phys.Commun. **182** (2011), 1674–1692, [arXiv:1011.2900 [hep-ph]].

[104] S. Badger, B. Biedermann, P. Uwer and V. Yundin, *Numerical evaluation of virtual corrections to multi-jet production in massless QCD*, Comput.Phys.Commun. **184** (2013), 1981–1998, [arXiv:1209.0100 [hep-ph]].

[105] C. F. Berger, Z. Bern, L. J. Dixon, F. F. Cordero, D. Forde et al., *One-Loop Calculations with BlackHat*, Nucl.Phys.Proc.Suppl. **183** (2008), 313–319, [arXiv:0807.3705 [hep-ph]].

[106] Z. Bern, L. J. Dixon, F. F. Cordero, S. Höche, H. Ita et al., *The Black-Hat Library for One-Loop Amplitudes*, J.Phys.Conf.Ser. **523** (2014), 012051, [arXiv:1310.2808 [hep-ph]].

[107] S. Alioli, S. Badger, J. Bellm, B. Biedermann, F. Boudjema et al., *Update of the Binoth Les Houches Accord for a standard interface between Monte Carlo tools and one-loop programs*, Comput.Phys.Commun. **185** (2014), 560–571, [arXiv:1308.3462 [hep-ph]].

[108] M. R. Whalley, D. Bourilkov and R. C. Group, *The Les Houches accord PDFs (LHAPDF) and LHAGLUE*, HERA and the LHC: A Workshop on the implications of HERA for LHC physics. Proceedings, Part B, 2005.

[109] S. Frixione and B. R. Webber, *Matching NLO QCD computations and parton shower simulations*, Journal of High Energy Physics **0206** (2002), 029, [arXiv:hep-ph/0204244 [hep-ph]].

[110] P. Nason, *A new method for combining NLO QCD with shower Monte Carlo algorithms*, Journal of High Energy Physics **11** (2004), 040, [hep-ph/0409146].

[111] S. Frixione, P. Nason and C. Oleari, *Matching NLO QCD computations with parton shower simulations: the POWHEG method*, Journal of High Energy Physics **11** (2007), 070, [arXiv:0709.2092 [hep-ph]].

[112] S. Höche, F. Krauss, M. Schönherr and F. Siegert, *A critical appraisal of NLO+PS matching methods*, Journal of High Energy Physics **09** (2012), 049, [arXiv:1111.1220 [hep-ph]].

[113] S. Höche, F. Krauss, M. Schönherr and F. Siegert, *W + n-Jet Predictions at the Large Hadron Collider at Next-To-Leading Order Matched with a Parton Shower*, Phys.Rev.Lett. **110** (2013), 052001, [arXiv:1201.5882 [hep-ph]].

[114] J. Alwall et al., *Comparative study of various algorithms for the merging of parton showers and matrix elements in hadronic collisions*, Eur. Phys. J. **C53** (2008), 473–500, [arXiv:0706.2569 [hep-ph]].

[115] S. Mrenna and P. Richardson, *Matching matrix elements and parton showers with HERWIG and PYTHIA*, Journal of High Energy Physics **0405** (2004), 040, [`arXiv:hep-ph/0312274` [hep-ph]].

[116] S. Höche, F. Krauss, N. Lavesson, L. Lönnblad, M. Mangano et al., *Matching parton showers and matrix elements*, `arXiv:hep-ph/0602031` [hep-ph].

[117] S. Catani, F. Krauss, R. Kuhn and B. R. Webber, *QCD matrix elements + parton showers*, Journal of High Energy Physics **0111** (2001), 063, [`arXiv:hep-ph/0109231` [hep-ph]].

[118] L. Lonnblad, *Correcting the color dipole cascade model with fixed order matrix elements*, JHEP **0205** (2002), 046, [`arXiv:hep-ph/0112284` [hep-ph]].

[119] G. Gustafson, *Dual description of a confined colour field*, Physics Letters **B175** (1986), no. 4, 453 – 456.

[120] G. Gustafson and U. Pettersson, *Dipole formulation of QCD cascades*, Nuclear Physics **B306** (1988), no. 4, 746 – 758.

[121] L. Lönnblad and S. Prestel, *Merging Multi-leg NLO Matrix Elements with Parton Showers*, Journal of High Energy Physics **1303** (2013), 166, [`arXiv:1211.7278` [hep-ph]].

[122] V. Hirschi, R. Frederix, S. Frixione, M. V. Garzelli, F. Maltoni et al., *Automation of one-loop QCD corrections*, Journal of High Energy Physics **1105** (2011), 044, [`arXiv:1103.0621` [hep-ph]].

[123] A. D. Martin, W. J. Stirling, R. S. Thorne and G. Watt, *Parton distributions for the LHC*, Eur.Phys.J. **C63** (2009), 189–285, [`arXiv:0901.0002` [hep-ph]].

[124] A. D. Martin, W. J. Stirling, R. S. Thorne and G. Watt, *Heavy-quark mass dependence in global PDF analyses and 3- and 4-flavour parton distributions*, Eur.Phys.J. **C70** (2010), 51–72, [`arXiv:1007.2624` [hep-ph]].

[125] S. Frixione, *Isolated photons in perturbative QCD*, Phys.Lett. **B429** (1998), 369–374, [`arXiv:hep-ph/9801442` [hep-ph]].

[126] T. Kinoshita, *Mass Singularities of Feynman Amplitudes*, J. Math. Phys. **3** (1962), 650.

[127] J. H. Kühn, A. A. Penin and V. A. Smirnov, *Summing up subleading Sudakov logarithms*, Eur.Phys.J. **C17** (2000), no. 1, 97–105, [`arXiv:hep-ph/9912503` [hep-ph]].

[128] S. Brensing, S. Dittmaier, M. Krämer and A. Mück, *Radiative corrections to W−boson hadroproduction: Higher-order electroweak and supersymmetric effects*, Phys.Rev. **D77** (2008), 073006, [`arXiv:0710.3309` [hep-ph]].

[129] S. Dittmaier and M. Huber, *Radiative corrections to the neutral-current Drell-Yan process in the Standard Model and its minimal supersymmetric extension*, JHEP **1001** (2010), 060, [`arXiv:0911.2329` [hep-ph]].

[130] J. Butterworth, G. Dissertori, S. Dittmaier, D. de Florian, N. Glover et al., *Les Houches 2013: Physics at TeV Colliders: Standard Model Working Group Report*, `arXiv:1405.1067` [hep-ph].

[131] A. Denner, S. Dittmaier, T. Kasprzik and A. Muck, *Electroweak corrections to W + jet hadroproduction including leptonic W-boson decays*, JHEP **08** (2009), 075, [`arXiv:0906.1656` [hep-ph]].

[132] A. D. Martin, R. G. Roberts, W. J. Stirling and R. S. Thorne, *Parton distributions incorporating QED contributions*, Eur. Phys. J. **C39** (2005), 155–161, [`arXiv:hep-ph/0411040` [hep-ph]].

[133] S. Höche, F. Krauss, S. Schumann and F. Siegert, *QCD matrix elements and truncated showers*, Journal of High Energy Physics **05** (2009), 053, [`arXiv:0903.1219` [hep-ph]].

[134] S. Höche, F. Krauss, M. Schönherr and F. Siegert, *QCD matrix elements + parton showers: The NLO case*, Journal of High Energy Physics **1304** (2013), 027, [`arXiv:1207.5030` [hep-ph]].

[135] G. Aad et al., ATLAS Collaboration, *Measurement of the ZZ production cross section and limits on anomalous neutral triple gauge couplings in proton-proton collisions at $\sqrt{s} = 7$ TeV with the ATLAS detector*, Phys.Rev.Lett. **108** (2012), 041804, [arXiv:1110.5016 [hep-ex]].

[136] G. Aad et al., ATLAS Collaboration, *Measurement of the WZ production cross section and limits on anomalous triple gauge couplings in proton-proton collisions at $\sqrt{s} = 7$ TeV with the ATLAS detector*, Phys.Lett. **B709** (2012), 341–357, [arXiv:1111.5570 [hep-ex]].

[137] G. Aad et al., ATLAS Collaboration, *Measurement of $W\gamma$ and $Z\gamma$ production cross sections in pp collisions at $\sqrt{s} = 7$ TeV and limits on anomalous triple gauge couplings with the ATLAS detector*, Phys.Lett. **B717** (2012), 49–69, [arXiv:1205.2531 [hep-ex]].

[138] S. Chatrchyan et al., CMS, *Measurement of the $W\gamma$ and $Z\gamma$ inclusive cross sections in pp collisions at $\sqrt{s} = 7\,TeV$ and limits on anomalous triple gauge boson couplings*, Phys.Rev. **D89** (2014), no. 9, 092005, [arXiv:1308.6832 [hep-ex]].

[139] S. Höche, F. Krauss, S. Pozzorini, M. Schönherr, J. M. Thompson et al., *Triple vector boson production through Higgs-Strahlung with NLO multijet merging*, Phys.Rev. **D89** (2014), no. 9, 093015, [arXiv:1403.7516 [hep-ph]].

[140] T. A. Collaboration, ATLAS Collaboration, *Search for the Associated Higgs Boson Production in the $WH \rightarrow WWW^{(*)} \rightarrow \ell\nu\ell\nu\ell\nu$ Decay Mode Using 4.7 fb^{-1} of Data Collected with the ATLAS Detector at $\sqrt{s} = 7$ TeV*, ATLAS–CONF–2012–078, ATLAS–COM–CONF–2012–094.

[141] T. C. Collaboration, CMS Collaboration, *Search for SM Higgs in WH to WWW to 3ℓ 3ν*, CMS–PAS–HIG–13–009.

[142] G. Aad et al., *Search for charginos nearly mass degenerate with the lightest neutralino based on a disappearing-track signature in pp colli-*

sions at $\sqrt{s}$=8 TeV *with the ATLAS detector*, Phys. Rev. **D88** (2013), 112006.

[143] T. Han and S. Willenbrock, *QCD correction to the* $pp \rightarrow WH$ *and* ZH *total cross-sections*, Phys.Lett. **B273** (1991), 167–172.

[144] O. Brein, A. Djouadi and R. Harlander, *NNLO QCD corrections to the Higgs-strahlung processes at hadron colliders*, Phys.Lett. **B579** (2004), 149–156, [arXiv:hep-ph/0307206 [hep-ph]].

[145] G. Ferrera, M. Grazzini and F. Tramontano, *Associated WH production at hadron colliders: a fully exclusive QCD calculation at NNLO*, Phys.Rev.Lett. **107** (2011), 152003, [arXiv:1107.1164 [hep-ph]].

[146] S. Dawson, T. Han, W. K. Lai, A. K. Leibovich and I. Lewis, *Resummation Effects in Vector-Boson and Higgs Associated Production*, Phys.Rev. **D86** (2012), 074007, [arXiv:1207.4207 [hep-ph]].

[147] A. Lazopoulos, K. Melnikov and F. Petriello, *QCD corrections to tri-boson production*, Phys.Rev. **D76** (2007), 014001, [arXiv:hep-ph/0703273 [hep-ph]].

[148] T. Binoth, G. Ossola, C. G. Papadopoulos and R. Pittau, *NLO QCD corrections to tri-boson production*, Journal of High Energy Physics **0806** (2008), 082, [arXiv:0804.0350 [hep-ph]].

[149] V. Hankele and D. Zeppenfeld, *QCD corrections to hadronic WWZ production with leptonic decays*, Phys.Lett. **B661** (2008), 103–108, [arXiv:0712.3544 [hep-ph]].

[150] F. Campanario, V. Hankele, C. Oleari, S. Prestel and D. Zeppenfeld, *QCD corrections to charged triple vector boson production with leptonic decay*, Phys.Rev. **D78** (2008), 094012, [arXiv:0809.0790 [hep-ph]].

[151] K. Arnold, J. Bellm, G. Bozzi, M. Brieg, F. Campanario et al., *VBFNLO: A Parton Level Monte Carlo for Processes with Electroweak Bosons – Manual for Version 2.5.0*, arXiv:1107.4038 [hep-ph].

[152] F. Krauss, R. Kuhn and G. Soff, *AMEGIC++ 1.0: A Matrix Element Generator In C++*, Journal of High Energy Physics **02** (2002), 044, [`hep-ph/0109036`].

[153] S. Catani, S. Dittmaier, M. H. Seymour and Z. Trócsányi, *The dipole formalism for next-to-leading order QCD calculations with massive partons*, Nucl. Phys. **B627** (2002), 189–265, [`hep-ph/0201036`].

[154] S. Frixione, P. Nason and B. R. Webber, *Matching NLO QCD and parton showers in heavy flavour production*, Journal of High Energy Physics **08** (2003), 007, [`hep-ph/0305252`].

[155] Z. Nagy and D. E. Soper, *Matching parton showers to NLO computations*, Journal of High Energy Physics **10** (2005), 024, [`hep-ph/0503053`].

[156] S. Schumann and F. Krauss, *A parton shower algorithm based on Catani-Seymour dipole factorisation*, Journal of High Energy Physics **03** (2008), 038, [`arXiv:0709.1027` [hep-ph]].

[157] T. Gehrmann, S. Höche, F. Krauss, M. Schönherr and F. Siegert, *NLO QCD matrix elements + parton showers in $e^+e^- \to$ hadrons*, Journal of High Energy Physics **1301** (2013), 144, [`arXiv:1207.5031` [hep-ph]].

[158] M. Cacciari, G. P. Salam and G. Soyez, *The Anti-k_T jet clustering algorithm*, Journal of High Energy Physics **0804** (2008), 063, [`arXiv:0802.1189` [hep-ph]].

[159] M. Cacciari, G. P. Salam and G. Soyez, *FastJet user manual*, Eur.Phys.J. **C72** (2012), 1896, [`arXiv:1111.6097` [hep-ph]].

[160] M. Schönherr and F. Krauss, *Soft photon radiation in particle decays in Sherpa*, Journal of High Energy Physics **12** (2008), 018, [`arXiv:0810.5071` [hep-ph]].

[161] J.-C. Winter, F. Krauss and G. Soff, *A modified cluster-hadronisation model*, Eur. Phys. J. **C36** (2004), 381–395, [`hep-ph/0311085`].

[162] S. Alekhin et al., *HERA and the LHC - A workshop on the implications of HERA for LHC physics: Proceedings Part A*, `hep-ph/0601012`.

[163] Frank Krauss and Petar Petrov and Marek Schönherr and Michael Spannowsky, *Measuring collinear W emissions inside jets*, Phys. Rev. **D89** (2014), 114006.

[164] S. Höche and M. Schönherr, *Uncertainties in next-to-leading order plus parton shower matched simulations of inclusive jet and dijet production*, Phys.Rev. **D86** (2012), 094042, [arXiv:1208.2815 [hep-ph]].

[165] Stefan Höche and Frank Krauss and Marek Schönherr, *Uncertainties in MEPS@NLO calculations of h + jets*, Phys. Rev. **D90** (2014), 014012.

[166] J. Rosiek, *Complete set of Feynman rules for the MSSM: Erratum*, arXiv:hep-ph/9511250 [hep-ph].

[167] T. Aaltonen et al., CDF, *Search for Supersymmetry in $p\bar{p}$ Collisions at $\sqrt{s}$ = 1.96 TeV Using the Trilepton Signature of Chargino-Neutralino Production*, Phys.Rev.Lett. **101** (2008), 251801, [arXiv:0808.2446 [hep-ex]].

[168] V. M. Abazov et al., D0, *Search for associated production of charginos and neutralinos in the trilepton final state using 2.3 fb^{-1} of data*, Phys.Lett. **B680** (2009), 34–43, [arXiv:0901.0646 [hep-ex]].

[169] M. Acciarri et al., L3, *Search for charginos and neutralinos in e^+e^- collisions at $\sqrt{S}$ = 189-GeV*, Phys.Lett. **B472** (2000), 420–433, [arXiv:hep-ex/9910007 [hep-ex]].

[170] J. Abdallah et al., DELPHI, *Searches for supersymmetric particles in e+ e- collisions up to 208-GeV and interpretation of the results within the MSSM*, Eur.Phys.J. **C31** (2003), 421–479, [arXiv:hep-ex/0311019 [hep-ex]].

[171] G. Abbiendi et al., OPAL, *Search for chargino and neutralino production at s**(1/2) = 192-GeV to 209 GeV at LEP*, Eur.Phys.J. **C35** (2004), 1–20, [arXiv:hep-ex/0401026 [hep-ex]].

[172] A. Heister et al., *Absolute mass lower limit for the lightest neutralino of the MSSM from e^+e data at $\sqrt{s}$ up to 209 GeV*, Physics Letters B **583** (2004), no. 34, 247 – 263.

[173] C. Englert, F. Krauss, M. Spannowsky and J. M. Thompson, *Di-Higgs phenomenology in : The forgotten channel* , Physics Letters **B743** (2015), no. 9, 93 – 97.

[174] G. Aad et al., ATLAS, *Measurements of Higgs boson production and couplings in diboson final states with the ATLAS detector at the LHC*, Phys.Lett. **B726** (2013), 88–119, [`arXiv:1307.1427` [hep-ex]].

[175] S. Chatrchyan et al., CMS, *Observation of a new boson with mass near 125 GeV in pp collisions at $\sqrt{s}$ = 7 and 8 TeV*, Journal of High Energy Physics **1306** (2013), 081, [`arXiv:1303.4571` [hep-ex]].

[176] E. Glover and J. van der Bij, *Higgs boson pair production via gluon fusion* , Nuclear Physics **B309** (1988), no. 2, 282 – 294.

[177] D. A. Dicus, C. Kao and S. S. Willenbrock, *Higgs boson pair production from gluon fusion* , Physics Letters **B203** (1988), no. 4, 457 – 461.

[178] T. Plehn, M. Spira and P. Zerwas, *Pair production of neutral Higgs particles in gluon-gluon collisions*, Nuclear Physics **B479** (1996), 46 – 64.

[179] A. Djouadi, W. Kilian, M. Mühlleitner and P. M. Zerwas, *Production of neutral Higgs-boson pairs at LHC*, The European Physical Journal C - Particles and Fields **10** (1999), no. 1, 45–49, (English).

[180] S. Dawson, S. Dittmaier and M. Spira, *Neutral Higgs boson pair production at hadron colliders: QCD corrections*, Phys.Rev. **D58** (1998), 115012, [`arXiv:hep-ph/9805244` [hep-ph]].

[181] R. Gröber and M. Mühlleitner, *Composite Higgs boson pair production at the LHC*, Journal of High Energy Physics **2011** (2011), no. 6, 20, (English).

[182] R. Contino, M. Ghezzi, M. Moretti, G. Panico, F. Piccinini and A. Wulzer, *Anomalous couplings in double Higgs production*, Journal of High Energy Physics **2012** (2012), no. 8, , (English).

[183] J. Baglio, A. Djouadi, R. Gröber, M. M. Mühlleitner, J. Quevillon and M. Spira, *The measurement of the Higgs self-coupling at the LHC:*

theoretical status, Journal of High Energy Physics **2013** (2013), no. 4, , (English).

[184] M. J. Dolan, C. Englert and M. Spannowsky, *Higgs self-coupling measurements at the LHC*, Journal of High Energy Physics **2012** (2012), no. 10, , (English).

[185] A. J. Barr, M. J. Dolan, C. Englert and M. Spannowsky, *Di-Higgs final states augMT2ed - Selecting hh events at the high luminosity LHC* , Physics Letters B **728** (2014), no. 20, 308 – 313.

[186] D. E. F. de Lima, A. Papaefstathiou and M. Spannowsky, *Standard model Higgs boson pair production in the (b b)(b b) final state*, Journal of High Energy Physics **2014** (2014), no. 8, , (English).

[187] A. Papaefstathiou, L. Yang and J. Zurita, *Higgs boson pair production at the LHC in the $b\bar{b}W^+W^-$ channel*, Phys. Rev. **D87** (2013), 011301.

[188] J. M. Butterworth, A. R. Davison, M. Rubin and G. P. Salam, *Jet Substructure as a New Higgs-Search Channel at the Large Hadron Collider*, Phys. Rev. Lett. **100** (2008), 242001.

[189] T. Plehn, G. P. Salam and M. Spannowsky, *Fat Jets for a Light Higgs Boson*, Phys. Rev. Lett. **104** (2010), 111801.

[190] L. G. Almeida, S. J. Lee, G. Perez, G. Sterman, I. Sung and J. Virzi, *Substructure of high-p_T jets at the LHC*, Phys. Rev. **D79** (2009), 074017.

[191] D. E. Soper and M. Spannowsky, *Combining subjet algorithms to enhance ZH detection at the LHC*, Journal of High Energy Physics **2010** (2010), no. 8, , (English).

[192] J. Thaler and K. V. Tilburg, *Identifying boosted objects with N-subjettiness*, Journal of High Energy Physics **2011** (2011), no. 3, , (English).

[193] D. E. Soper and M. Spannowsky, *Finding physics signals with shower deconstruction*, Phys. Rev. **D84** (2011), 074002.

[194] L. G. Almeida, O. Erdoğan, J. Juknevich, S. J. Lee, G. Perez and G. Sterman, *Three-particle templates for a boosted Higgs boson*, Phys. Rev. **D85** (2012), 114046.

[195] S. D. Ellis, A. Hornig, T. S. Roy, D. Krohn and M. D. Schwartz, *Nondeterministic Approach to Tree-Based Jet Substructure*, Phys. Rev. Lett. **108** (2012), 182003.

[196] D. E. Soper and M. Spannowsky, *Finding top quarks with shower deconstruction*, Phys. Rev. **D87** (2013), 054012.

[197] U. Baur, T. Plehn and D. Rainwater, *Determining the Higgs boson self-coupling at hadron colliders*, Phys. Rev. **D67** (2003), 033003.

[198] U. Baur, T. Plehn and D. Rainwater, *Probing the Higgs self-coupling at hadron colliders using rare decays*, Phys. Rev. **D69** (2004), 053004.

[199] T. A. Collaboration, ATLAS, *Physics at a High-Luminosity LHC with ATLAS (Update)*, ATL-PHYS-PUB-2012-004, ATL-COM-PHYS-2012-1455.

[200] D. Shao, C. Li, H. Li and J. Wang, *Threshold resummation effects in Higgs boson pair production at the LHC*, Journal of High Energy Physics **2013** (2013), no. 7, , (English).

[201] D. de Florian and J. Mazzitelli, *Two-loop virtual corrections to Higgs pair production*, Physics Letters **B724** (2013), no. 45, 306 – 309.

[202] J. Grigo, J. Hoff, K. Melnikov and M. Steinhauser, *On the Higgs boson pair production at the LHC*, Nuclear Physics **B875** (2013), no. 1, 1 – 17.

[203] P. Maierhöfer and A. Papaefstathiou, *Higgs boson pair production merged to one jet*, Journal of High Energy Physics **2014** (2014), no. 3, , (English).

[204] M. J. Dolan, C. Englert, N. Greiner and M. Spannowsky, *Production of hhjj at the LHC*, Phys. Rev. Lett. **112** (2014), 101802.

[205] F. Goertz, A. Papaefstathiou, L. Yang and J. Zurita, *Higgs boson self-coupling measurements using ratios of cross sections*, Journal of High Energy Physics **2013** (2013), no. 6, , (English).

[206] J. R. Ellis, M. K. Gaillard and D. V. Nanopoulos, *A Phenomenological Profile of the Higgs Boson*, Nucl.Phys. **B106** (1976), 292, CERN-TH-2093.

[207] M. A. Shifman, A. I. Vainshtein, M. B. Voloshin and V. I. Zakharov, *Low-Energy Theorems for Higgs Boson Couplings to Photons*, Sov.J.Nucl.Phys. **30** (1979), 711–716, ITEP-42-1979, ITEP-42.

[208] B. A. Kniehl and M. Spira, *Low-energy theorems in Higgs physics*, Zeitschrift für Physik C Particles and Fields **69** (1995), no. 1, 77–87, (English).

[209] Steven Abel and Alberto Mariotti, *Novel Higgs Potentials from Gauge Mediation of Exact Scale Breaking*, Phys.Rev. **D89** (2014), no. 12, 125018, [`arXiv:1312.5335` [hep-ph]].

[210] The ATLAS Collaboration, *Measurement of the b-tag Efficiency in a Sample of Jets Containing Muons with 5 fb1 of Data from the ATLAS Detector*, Tech. Report ATLAS-CONF-2012-043, CERN, Geneva, Mar 2012.

[211] A. L. Read, *Presentation of search results: the CL s technique*, Journal of Physics G: Nuclear and Particle Physics **28** (2002), no. 10, 2693.

[212] T. Junk, *Confidence level computation for combining searches with small statistics*, Nuclear Instruments and Methods in Physics Research Section A: Accelerators, Spectrometers, Detectors and Associated Equipment **434** (1999), no. 23, 435 – 443.

[213] T. Junk, *Sensitivity, Exclusion and Discovery with Small Signals, Large Backgrounds, and Large Systematic Uncertainties*, Tech. Report CDF Note 8128 [cdf/doc/statistics/public/8128]., Fermilab, October 2007.

[214] T. Junk, *Building a more general χ^2*, Tech. Report CDF Note 7904 [cdf/doc/statistics/public/7904]., University of Illinois at Urbana-Champaign, March 2006.

[215] V. Khachatryan et al., CMS Collaboration, *Search for resonant pair production of Higgs bosons decaying to two bottom quark-antiquark pairs in proton-proton collisions at 8 TeV*, arXiv:1503.04114 [hep-ex].

[216] G. Aad et al., ATLAS, *Search for the Standard Model Higgs boson produced in association with top quarks and decaying into $b\bar{b}$ in pp collisions at $\sqrt{s} = 8$ TeV with the ATLAS detector*, arXiv:1503.05066 [hep-ex].

[217] A. J. Barr, M. J. Dolan, C. Englert, D. E. F. de Lima and M. Spannowsky, *Higgs Self-Coupling Measurements at a 100 TeV Hadron Collider*, Journal of High Energy Physics **1502** (2015), 016, [arXiv:1412.7154 [hep-ph]].

[218] R. Boughezal, C. Focke, Y. Li and X. Liu, *Jet vetoes for Higgs production at future hadron colliders*, Phys.Rev. **D90** (2014), no. 5, 053001, [arXiv:1405.4562 [hep-ph]].

[219] C.-R. Chen and I. Low, *Double take on new physics in double Higgs boson production*, Phys.Rev. **D90** (2014), no. 1, 013018, [arXiv:1405.7040 [hep-ph]].

[220] A. Azatov, R. Contino, G. Panico and M. Son, *Effective field theory analysis of double Higgs production via gluon fusion*, arXiv:1502.00539 [hep-ph].

[221] P. Lebiedowicz and A. Szczurek, *Exclusive production of heavy charged Higgs boson pairs in the $pp \to ppH^+H^-$ reaction at the LHC and FCC*, arXiv:1502.03323 [hep-ph].

[222] T. Cohen, T. Golling, M. Hance, A. Henrichs, K. Howe et al., *SUSY Simplified Models at 14, 33, and 100 TeV Proton Colliders*, Journal of High Energy Physics **1404** (2014), 117, [arXiv:1311.6480 [hep-ph]].

[223] S. Jung and J. D. Wells, *Gaugino physics of split supersymmetry spectra at the LHC and future proton colliders*, Phys.Rev. **D89** (2014), no. 7, 075004, [arXiv:1312.1802 [hep-ph]].

[224] B. Fuks, J. Proudom, J. Rojo and I. Schienbein, *Characterizing New Physics with Polarized Beams at High-Energy Hadron Colliders*, Journal of High Enery Physics **1405** (2014), 045, [arXiv:1403.2383 [hep-ph]].

[225] M. Lou and L.-T. Wang, *Neutralino dark matter at 14 TeV and 100 TeV*, Journal of High Energy Physics **1408** (2014), 161, [arXiv:1404.0682 [hep-ph]].

[226] A. Fowlie and M. Raidal, *Prospects for constrained supersymmetry at $\sqrt{s} = 33\,TeV$ and $\sqrt{s} = 100\,TeV$ proton-proton super-colliders*, Eur.Phys.J. **C74** (2014), 2948, [arXiv:1402.5419 [hep-ph]].

[227] W. Altmannshofer, P. J. Fox, R. Harnik, G. D. Kribs and N. Raj, *Dark Matter Signals in Dilepton Production at Hadron Colliders*, arXiv:1411.6743 [hep-ph].

[228] T. Cohen, R. T. D'Agnolo, M. Hance, H. K. Lou and J. G. Wacker, *Boosting Stop Searches with a 100 TeV Proton Collider*, Journal of High Energy Physics **1411** (2014), 021, [arXiv:1406.4512 [hep-ph]].

[229] D. S. M. Alves, J. Galloway, J. T. Ruderman and J. R. Walsh, *Running Electroweak Couplings as a Probe of New Physics*, Journal of High Energy Physics **1502** (2015), 007, [arXiv:1410.6810 [hep-ph]].

[230] B. S. Acharya, K. Boek, C. Pongkitivanichkul and K. Sakurai, *Prospects for observing charginos and neutralinos at a 100 TeV proton-proton collider*, Journal of High Energy Physics **1502** (2015), 181, [arXiv:1410.1532 [hep-ph]].

[231] Y. Wen, H. Qu, D. Yang, Q. shu Yan, Q. Li et al., *Probing triple-W production and anomalous WWWW coupling at the CERN LHC and future $\mathcal{O}(100)$ TeV proton-proton collider*, Journal of High Energy Physics **1503** (2015), 025, [arXiv:1407.4922 [hep-ph]].

[232] J. Perez-Peraza, J. Velasco, A. Gallegos-Cruz, M. Alvarez-Madrigal, A. Faus-Golfe et al., *Parametrization of proton proton total cross-section from 10 GeV to 100 TeV*, arXiv:hep-ph/0011167 [hep-ph].

[233] J. A. Aguilar-Saavedra, B. Fuks and M. L. Mangano, *Pinning down top dipole moments with ultra-boosted tops*, `arXiv:1412.6654` [hep-ph].

[234] G. Aad et al., ATLAS, *Measurement of the $WW + WZ$ cross section and limits on anomalous triple gauge couplings using final states with one lepton, missing transverse momentum, and two jets with the ATLAS detector at $\sqrt{s} = 7$ TeV*, Journal of High Energy Physics **1501** (2015), 049, [`arXiv:1410.7238` [hep-ex]].

[235] V. Khachatryan et al., CMS Collaboration, *Measurements of the ZZ production cross sections in the 2 l 2 nu channel in proton-proton collisions at $\sqrt{s} = 7$ and 8 TeV and combined constraints on triple gauge couplings*, `arXiv:1503.05467` [hep-ex].

[236] G. Aad et al., ATLAS Collaboration, *Evidence of $W\gamma\gamma$ production in pp collisions at $\sqrt{s} = 8$ TeV and limits on anomalous quartic gauge couplings with the ATLAS detector*, `arXiv:1503.03243` [hep-ex].

[237] V. Khachatryan et al., CMS, *Measurement of the Z production cross section in pp collisions at 8 TeV and search for anomalous triple gauge boson couplings*, Journal of High Energy Physics **1504** (2015), 164, [`arXiv:1502.05664` [hep-ex]].

[238] V. Gribov and L. Lipatov, *Deep inelastic e p scattering in perturbation theory*, Sov.J.Nucl.Phys. **15** (1972), 438–450, IPTI-381-71.

[239] Y. L. Dokshitzer, *Calculation of the Structure Functions for Deep Inelastic Scattering and e+ e- Annihilation by Perturbation Theory in Quantum Chromodynamics.*, Sov.Phys.JETP **46** (1977), 641–653.

[240] G. Altarelli and G. Parisi, *Asymptotic Freedom in Parton Language*, Nucl.Phys. **B126** (1977), 298, LPTENS-77-6.

[241] L. Lipatov, *Reggeization of the Vector Meson and the Vacuum Singularity in Nonabelian Gauge Theories*, Sov.J.Nucl.Phys. **23** (1976), 338–345.

[242] E. A. Kuraev, L. N. Lipatov and V. S. Fadin, *Multi - Reggeon Processes in the Yang-Mills Theory*, Sov.Phys.JETP **44** (1976), 443–450.

[243] E. Kuraev, L. Lipatov and V. S. Fadin, *The Pomeranchuk Singularity in Nonabelian Gauge Theories*, Sov.Phys.JETP **45** (1977), 199–204.

[244] I. Balitsky and L. Lipatov, *The Pomeranchuk Singularity in Quantum Chromodynamics*, Sov.J.Nucl.Phys. **28** (1978), 822–829.

[245] L. Lipatov, *The Bare Pomeron in Quantum Chromodynamics*, Sov.Phys.JETP **63** (1986), 904–912, LENINGRAD-85-1137.

[246] E. Gerwick, T. Plehn and S. Schumann, *Understanding Jet Scaling and Jet Vetos in Higgs Searches*, Phys. Rev. Lett. **108** (2012), 032003.

[247] E. Gerwick, T. Plehn, S. Schumann and P. Schichtel, *Scaling Patterns for QCD Jets*, JHEP **10** (2012), 162, [`arXiv:1208.3676` [hep-ph]].

[248] A. Buckley, J. Butterworth, L. Lönnblad, D. Grellscheid, H. Hoeth et al., *Rivet user manual*, Comput.Phys.Commun. **184** (2013), 2803–2819, [`arXiv:1003.0694` [hep-ph]].

[249] D. Binosi and L. Theußl, *JaxoDraw: A graphical user interface for drawing Feynman diagrams*, Computer Physics Communications **161** (2004), no. 12, 76 – 86.

[250] J. D. Hunter, *Matplotlib: A 2D graphics environment*, Computing In Science & Engineering **9** (2007), no. 3, 90–95.